In the context of the ground testing to streamline the deployment process of wind turbines, this thesis presents a comprehensive analysis on the application of a grid emulator to conduct grid compliance tests of wind turbines (WT). The focus of the thesis lies on the flicker measurements caused by the output power fluctuations of WTs, mainly due to the wind turbulence and the tower shadowing effect, as well as the low-voltage ride-through (LVRT) tests. Firstly, the design requirements are derived based on the behavior of the device under test (DUT) and the regulatory frameworks. Afterwards, the application of a multi-megawatt grid emulator employing interleaved multi-megawatt converters is analyzed. Next to the filter design to meet criteria on the voltage quality, the emulation of a high grid impedance at the point of common coupling (PCC) is presented in this thesis. This appears to be the worst scenario when it comes to the flicker emission and the LVRT capability of WTs. The results show that the grid emulator concept is capable of meeting the derived design criteria in terms of the voltage quality and dynamic. The stability limit of the coupled system between the grid emulator and DUT can be well predicted by only considering the passive elements of the DUT. Hence, with the presented grid emulator, LVRT tests and flicker measurements can be conducted on a wind turbine test bench with a good accuracy.

ISBN 978-3-948234-09-6

Thinking the Future
Zukunft denken

Analysis of the Application of a Grid Emulator to Conduct Grid Compliance Tests for Multi-Megawatt Wind Turbines
Nurhan Rizqy Averous

E.ON Energy Research Center
RWTH AACHEN UNIVERSITY

Analysis of the Application of a Grid Emulator to Conduct Grid Compliance Tests for Multi-Megawatt Wind Turbines

A Contribution towards Ground Testing of Wind Turbines

Nurhan Rizqy Averous
Institute for Power Generation and Storage Systems

Analysis of the Application of a Grid Emulator to Conduct Grid Compliance Tests for Multi-Megawatt Wind Turbines

A Contribution towards Ground Testing of Wind Turbines

Von der Fakultät für Elektrotechnik und Informationstechnik der Rheinisch-Westfälischen Technischen Hochschule Aachen zur Erlangung des akademischen Grades eines Doktors der Ingenieurwissenschaften genehmigte Dissertation

vorgelegt von
Nurhan Rizqy Averous, M.Sc.
aus Kudus, Indonesien

Berichter:
Univ.-Prof. Dr. ir. Dr. h. c. Rik W. De Doncker
Univ.-Prof. Dr.-Ing. Georg Jacobs

Tag der mündlichen Prüfung: 15. October 2020

Diese Dissertation ist auf den Internetseiten
der Universitätsbibliothek online verfügbar.

Bibliographische Information der Deutschen Nationalbibliothek
Die Deutsche Nationalbibliothek verzeichnet diese Publikation in der Deutschen Nationalbibliografie; detaillierte bibliografische Daten sind im Internet über http://dnb-nb.de abrufbar.

D 82 (Diss. RWTH Aachen University, 2021)

Herausgeber:
Univ.-Prof. Dr. ir. Dr. h. c. Rik W. De Doncker
Direktor E.ON Energy Research Center

Institute for Power Generation and Storage Systems (PGS)
E.ON Energy Research Center
Mathieustraße 10
52074 Aachen

E.ON Energy Research Center I 95. Ausgabe der Serie
PGS I Power Generation and Storage Systems

Copyright Nurhan Rizqy Averous
Alle Rechte, auch das des auszugsweisen Nachdrucks, der auszugsweisen oder vollständigen Wiedergabe, der Speicherung in Datenverarbeitungsanlagen und der Übersetzung, vorbehalten.

Printed in Germany

ISBN: 978-3-948234-09-6
1. Auflage 2021

Verlag:
E.ON Energy Research Center, RWTH Aachen University
Mathieustraße 10
52074 Aachen
Internet: www.eonerc.rwth-aachen.de
E-Mail: post_erc@eonerc.rwth-aachen.de

Preface

This dissertation work was conducted during my work as a research associate at the Institute for Power Generation and Storage Systems (PGS), E.ON Energy Research Center (ERC), RWTH Aachen University. This work was part of the public-funded research projects that were conducted at the Center for Wind Power Drives (CWD), RWTH Aachen University, which is a research house for wind energy.

First of all, I would like to thank Allah SWT for the wonderful far-from-home journey in Germany as well as the health and strength that I needed to accomplish one of my missions in this country. I would like to express my gratitude to Prof. De Doncker as the Director of the Institute PGS and my "Doktorvater" for the opportunity to join the Institute ISEA and PGS, to work on my dissertation project, for the freedom and the guidance during the entire project. Besides, I would like to thank him for the trust he gave when he appointed me as a group leader and chief engineer at PGS to work on various topics to achieve a successful energy transition. I also wish to thank Prof. Jacobs, the Spokesman of the Board of Directors at CWD, for being the co-advisor of my dissertation and also for the cooperation, advices, eventful projects at the CWD which gave me a valuable experience to my journey. Nevertheless, I would like to express my appreciation to the industry partners in particular the colleagues at Siemens AG in Ruhstorf an der Rott for the support and contribution in the projects at CWD which made this thesis possible.

I would like to thank all my dear colleagues at PGS, ISEA and CWD for the colorful institute life, the cooperation and continuous support. Especially to Dr. Marco Stieneker, Benedict Mortimer, Philipp Joebges and Steffen Beushausen, I would also like to express my appreciation for the interesting discussions, cooperation, jokes and their helps in overcoming my cultural and language challenges in Germany. Besides many thanks are also directed to the entire administration, IT and workshop teams at the E.ON ERC, ISEA and CWD. Without their support, it would have been very difficult to realize the project.

Special thanks to my family, my wife Aya, my son Luthfi and my latest edition Rashdan for the support, smiles and motivation to overcome the challenges

throughout my dissertation time. Last but not least, I would like to express my highest gratitude to my parents for the motivation, the financial support and the precious opportunity to study in Germany.

Aachen, September 2021
Nurhan Rizqy Averous

Abstract

With the increasing share of wind energy in today's energy mix, wind energy plays an important role in keeping the stable operation of the electricity grid. Next to the design, verification tests of wind turbines are highly important to ensure a reliable operation. Compared to the field tests, wind turbine testing on a nacelle test bench offer substantial benefits. Thanks to the emulator systems, the operation conditions are controllable and reproducible. Hence, time and cost intensive field tests can be performed in a more efficient manner resulting in time and cost reduction. Besides, the flexibility offered by a power-electronics-based grid emulator enables a wide variety of test scenarios.

This thesis presents an analysis on the application of a multi-megawatt grid emulator concept to perform the two most challenging grid compliance tests of wind turbines, flicker measurements and low-voltage ride-through (LVRT) tests. Firstly, this thesis elaborates the behavior of a wind turbine to derive the design criteria for a grid emulator as well as to draw a reference behavior. The reference behavior is essential to evaluate the performance of a grid emulator. Afterwards, the design requirements for a grid emulator from the perspective of the regulatory are identified. In the last part of this thesis, a concept evaluation of a multi-megawatt grid emulator employing multiple medium-voltage converters is presented. This includes a proper filter design and an interaction analysis with the device under test. The results show that the grid emulator concept is capable of meeting the design requirements to conduct flicker measurements and LVRT tests.

The analysis results in this thesis are verified with a 2.75 MW reference nacelle at the Center for Wind Power Drives (CWD), RWTH Aachen University in Aachen, Germany.

Contents

1 Introduction **1**
- 1.1 Motivation . . . 1
- 1.2 State-of-the-Art . . . 3
- 1.3 Objective and Approach . . . 5
- 1.4 Grid Model and Sign Convention . . . 7

2 Fundamental Wind Energy Conversion **9**
- 2.1 Wind Energy Conversion . . . 9
- 2.2 Drivetrain Architectures . . . 10
- 2.3 Power-Electronic Converter Architecture . . . 11
- 2.4 Wind-Turbine Control Architecture . . . 12
- 2.5 A 2.75 MW Reference Wind Turbine . . . 16

3 Output Power Fluctuations **23**
- 3.1 Flicker . . . 24
- 3.2 Origins of Power Fluctuations . . . 27
  - 3.2.1 Wind Turbulences . . . 27
  - 3.2.2 Tower Shadowing Effect . . . 27
  - 3.2.3 Drivetrain Resonance . . . 34
- 3.3 Flicker Caused by Power Fluctuations . . . 35
- 3.4 Average Output Power Drift due to Turbulence . . . 40
- 3.5 Summary . . . 42

4 Dynamic Behavior at the Grid Connection Point **43**
- 4.1 Current Controller Modeling . . . 44
- 4.2 Grid-Fault Scenarios and Models . . . 53
- 4.3 Behavior of the Current Controller during Grid Faults . . . 56
  - 4.3.1 Current Controller Performance . . . 56
  - 4.3.2 Loss of Synchronization . . . 61
- 4.4 Dynamic Behavior of Reference Nacelle during Grid Faults . . . 65
  - 4.4.1 Simulation Model and Validation . . . 65
  - 4.4.2 Control Response under Various Grid Impedances . . . 66
  - 4.4.3 Dynamic Behavior during Grid Faults . . . 68
- 4.5 Summary . . . 72

5 Analysis on Regulatory Frameworks **73**
5.1 Static Grid Support . . . 73
5.2 Dynamic Grid Support . . . 75
5.2.1 Low-Voltage Ride-Through (LVRT) . . . 75
5.2.2 High-Voltage Ride Through (HVRT) . . . 79
5.3 Flicker . . . 81
5.4 Harmonic Distortion . . . 87

6 Multi-Megawatt Grid Emulator **89**
6.1 Topology . . . 89
6.1.1 Review on the State-of-the-Art . . . 89
6.1.2 Interleaved Converters . . . 91
6.2 Filter Design . . . 96
6.2.1 System Modeling . . . 97
6.2.2 Parameters Selection and Verification . . . 99
6.3 Grid Impedance Emulation . . . 103
6.3.1 Implementation . . . 103
6.3.2 Stability Assessment at PCC . . . 104
6.3.3 Performance Evaluation . . . 108
6.4 Coupled Operation with a Device Under Test . . . 110
6.4.1 Operation with a Power Fluctuation . . . 110
6.4.2 Low-Voltage Ride-Through Test . . . 112
6.5 Summary . . . 113

7 Conclusions and Future Work **115**
7.1 Summary and Conclusion . . . 115
7.2 Future Work . . . 116

A Appendix **119**
A.1 Park and Clarke Transformation . . . 120
A.2 Electromagnetic Transient Simulation Model of the Wind Turbines 122
A.3 Symmetrical-Component Quantities according to IEC 61400-21 . . 123

B Acronyms **125**

List of Figures **129**

List of Tables **135**

Bibliography **137**

1 Introduction

1.1 Motivation

As part of the roadmap towards a sustainable energy supply, the electricity generation out of wind energy has been increased in the last decade. In Europe alone, around 150 GW of wind turbines have been installed until 2016 which already surpassed the total installed capacity of coal power plants in this region [1]. This number is expected to increase further in the future in an attempt to suppress the greenhouse emissions as well as the fossil fuel consumption. Directorate General Energy and Transportation of the European Commission is targeting at least 27 % share of renewable energy including wind energy in 2030. With such a significant share of wind energy within the energy supply structure, wind energy will play a significant role in the future operation of power systems. Hence, they must be highly reliable to guarantee the security and stability of the power supply.

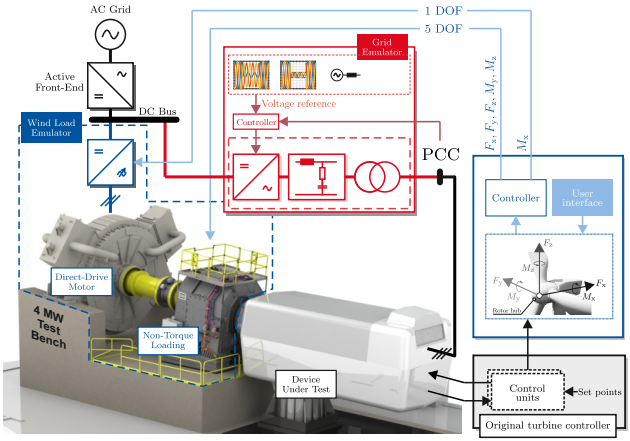

Figure 1.1: Schematic of a 4 MW nacelle test bench at CWD RWTH Aachen University

Next to the technological development of wind turbines, design validation and certification tests including for the grid compliance verification of the entire nacelle assembly are critical aspects for the successful deployment and operation of wind turbines. These are typically accomplished in a selected test field on a wind turbine in a full setup including the rotor assembly and the tower . The wind turbine being tested or also called device under test (DUT) is connected to a public grid. However, due to the indeterministic and non-repeatable test conditions, this approach is tremendously time consuming as well as greatly cost intensive which lead to a high development cost. Furthermore, the possible test scenarios are also limited to the given conditions in the test field making this approach inflexible.

Alternatively, testing of a wind turbine nacelle may be carried out on a nacelle test bench without the rotor blades and the tower assembly as firstly introduced by Jansen [2], [3]. This approach benefits from the so-called emulator systems that mimic the behavior of the rotor blades at the rotor flange (wind load emulator) as well as the electrical grid at the point of common coupling (PCC) (grid emulator) in a controllable manner. As the dependency on the uncertain weather and grid conditions is greatly reduced by means of the emulator systems, a substantial cost reduction and time saving can be achieved. Therefore, this concept quickly gained interest and applied worldwide in several wind turbine development centers [4]–[7] including at the Center for Wind Power Drives (CWD), RWTH Aachen University [8]–[12].

Figure 1.1 illustrates the schematic of a 4 MW nacelle test bench at the CWD. In this setup, the wind load emulator is indicated in blue. It comprises a low-speed direct-drive permanent-magnet motor and a non-torque loading unit. The direct-drivea permanent-magnet motor is responsible for the application of the rotating torque on the main shaft of the DUT M_{x}. Meanwhile, the task of the non-torque loading unit is to apply the remaining 5 off axis loads F_{x}, F_{y}, F_{z}, M_{y} and M_{z}. These hardware are commanded by a real-time simulation of the rotor blades considering not only the wind field but also the response of the DUT by its controller e.g. the pitch position of the rotor blades. The detailed description on the emulation of the wind load can be found in [10], [13], [14].

At the PCC, a power-electronic-based grid emulator indicated in red is employed to apply a controllable three-phase grid voltage replicating the behavior of an electric grid. The power segment of the grid emulator comprises a power-electronic converter system, a filter unit to minimize the voltage harmonics due to the converter switchings and a transformer depending on the desired voltage level at the PCC. A controller unit determines the switching states for the power-electronic converter system to produce a voltage signal at the PCC according to the refer-

ence voltage depending on the test scenario. This gives a higher degree of freedom in applying three-phase voltages at PCC which enables a wide spectrum of possible test scenarios compared to the conventional approach. The voltage reference in Fig. 1.1 may be generated internally by the controller itself or received from a real-time electrical grid simulator that realistically mimics a grid behavior for the DUT at PCC. Thereby, a wide varieties of electrical grids can theoretically be virtually replicated at PCC enabling a closer look to the performance of wind turbine (WT)s at certain grid situations. The second approach is also widely known as Power Hardware-in-the-Loop (PHiL).

1.2 State-of-the-Art

Voltage dips and swells

For design validation and grid compliance verification purposes, several methods have been utilized to apply voltage variations at the PCC of WT. In these methods, WT are connected to a public grid at PCC. The simplest method is by means of a transformer with an on-load tap changer as shown in Fig. 1.2a [15]. The voltage variation is accomplished by modifying the winding ratio between the primary and secondary winding using mechanical switches. In further development of this concept, the mechanical switches are substituted with power-electronic switches to improve the transient performance of this concept [16]–[18].

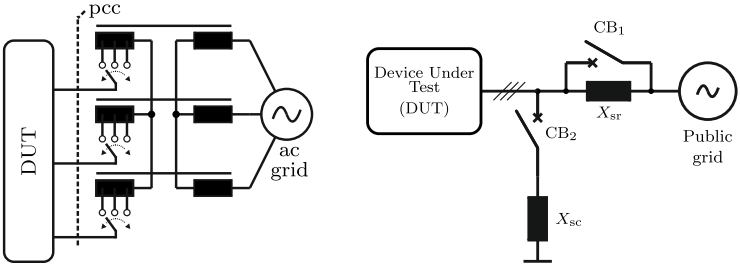

(a) Transformer-based method [15]

(b) Shunt-impedance-based method [19]–[22]

Figure 1.2: Methods to apply voltage dips for wind turbines testing

Another method utilizes an inductive divider principle or often called shunt-impedance-based voltage dip generator. The schematic of this concept is shown

in Fig. 1.2b [19]–[22]. Initially, the switch CB_1 is closed while the switch CB_2 is open. To initiate a voltage dip, CB_1 is firstly opened and an inductive X_{sr} is energized to limit the influence of the DUT on the ac grid when performing the test. At the same time, a high value of inductive grid impedance is introduced at PCC by X_{sr} since the value of X_{sr} is typically set relatively high. The voltage dip [(i)] is then generated by closing the switch CB_2 and the residual voltage of the dip is defined by the value of X_{sr} and X_{sc}. Afterwards, the voltage dip is cleared by opening CB_2 and CB_1 such that the system returns to the initial state. Both shunt-impedance-based method has been standardized in certification guidelines not only in Germany [23] but also worldwide [24].

In contrast to the power-electronic based grid emulator, the shunt-impedance-based method is less flexible. Firstly, the grid impedance during fault is fixed by the inductances depending on the available short-circuit power of the grid at the test location and the residual voltage of the applied voltage dip. Secondly, the rate-of-ramp of the voltage transient cannot be freely selected since it operates based on switchings of discrete sets of inductors. This means that voltage dips with a lower rate-of-ramp of voltage [25], which can be caused for instance by a energizing process of large power transformers, cannot be reproduced.

Frequency variations

So far, no hardware equipment has been introduced in the test guidelines to apply frequency variations PCC. To assess the reaction of the DUT with regards to variations in the grid frequency, the frequency variation tests are performed by slightly adjusting the programmed nominal frequency in the DUT while it is operating at an electrical grid. Thus, the DUT detects a frequency deviation although the real grid frequency is unchanged. By doing so, the reaction of the controller against frequency variations in terms of maintaining the synchronous operation with the electrical grid and fed-in power can be assessed.

However, the currently applied method is prone to errors because the influence of the frequency variation on the hardware level is completely disregarded. As an example, the impedance variations of the DUT's passive elements at the fundamental frequency as a result of frequency deviation are not reflected in the test results. Particularly in DUTs with a relatively low switching frequencies, the filter elements are relatively large to comply with the power quality requirements. Hence, the voltage drops across the filter elements may vary significantly with the

[(i)] also called voltage sag in several countries

changing grid frequencies which may cause the DUT exceeding its operation constraints such as overvoltages or overmodulation. Thereby, a discrepancy between the test results and the real behavior would occur.

1.3 Objective and Approach

Thanks to the emulator systems at the mechanical and electrical interfaces, nacelle test benches offers the possibility of time- and cost-intensive grid compliance verification tests to be performed on the ground under a fully controllable operation conditions. On the way of introducing this method as an alternative to the currently applied method, a question has been raised whether the behavior of wind turbines in the field can be reproduced on the test bench. Moreover, the key aspects to be considered in the design and evaluation of a grid emulator are not yet clear because the current regulatory framework does not fully cover this option.

This thesis presents a comprehensive analysis on the application of a grid emulator system to conduct grid compliance verification tests for multi-megawatt wind turbines. The topic coverage of this thesis is graphically shown in Fig. 1.3. Firstly, this thesis elaborates the behavior of a multi-megawatt wind turbine under various operation conditions. By doing so, a reference can be drawn when comparing the test results obtained by means of a grid emulator. Furthermore, elaborating the behavior of wind turbines also enables a derivation of the design requirements suitable for grid emulators. Secondly, the regulatory framework for grid compliance tests of wind turbines is analyzed. This particular part will identify which design criteria in the current standards and guidelines require further interpretation in order to be applied to a grid emulator. Lastly, a concept of a multi-megawatt grid emulator will be presented and evaluated in fulfilling the requirements and reproducing the behavior of a wind turbine. This thesis will not address all grid compliance tests of wind turbines but focuses only on the tests, flicker measurements and low-voltage ride-through (LVRT) tests.

This thesis is structured as follows:

Chapter 2 will present the fundamental, the system architecture and the control structure of a wind turbine. Furthermore, a research wind turbine nacelle developed at the Center for Wind Power Drives (CWD), RWTH Aachen University for research purposed will also be presented. This turbine will be used to verify the analysis in chapter 3 and 4.

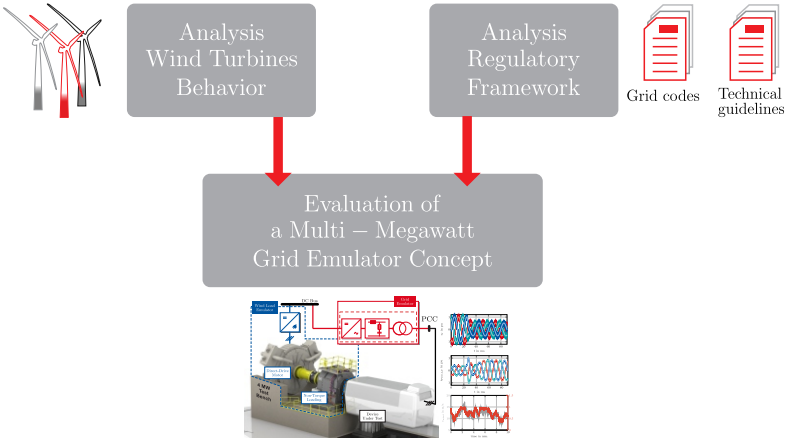

Figure 1.3: Topics coverage of the thesis

Chapter 3 deals with the output power fluctuation of wind turbines which is the main cause of flicker. Here, the origins of output power fluctuation of a wind turbine will be identified based on theory and measurements on the research nacelle. Furthermore, the main contributing origins of the output power fluctuation to flicker phenomenon will be identified. This is a crucial input to derive the dynamic criterion for a grid emulator to perform flicker measurements.

Chapter 4 elaborates the dynamic behavior of a wind turbine when it encounters a voltage dip. Firstly, the potential fault scenarios in an electrical grid is studied. Afterwards, the reaction of the wind turbines to the fault scenarios will be analyzed. The outcome of the chapter will serve as a reference when evaluating the performance of a grid emulator discussed in chapter 6.

Chapter 5 presents the analysis on the regulatory frameworks for grid compliance and certification tests of wind turbines. Besides, an evaluation of the current test method according to the regulatory framework will also be introduced. Furthermore, a derivation of requirements that can be used as a reference for the design of a grid emulator will be introduced.

In **Chapter 6**, a concept for multi-megawatt grid emulator employing multiple medium-voltage converters will be deeply elaborated. Afterwards, the stability analysis of a coupled system between the grid emulator and a device under test will be performed. The stability analysis is followed by the concept assessment

and evaluation with regards to the design criteria determined in chapter 5.

Chapter 7 closes the thesis with a summary as well as conclusion remarks. Besides, some future works will be introduced following the works presented within this thesis.

1.4 Grid Model and Sign Convention

For the discussions within this thesis, The electrical grid is modeled as a three-phase sinusoidal voltage source and a grid impedance that comprises an inductive L_{grid} and a resistive part R_{grid} as shown in Fig. 1.4a. Hence, the impedance of the grid can be written as follows

$$\underline{Z}_{\text{grid}} = R_{\text{grid}} + \mathrm{j}X_{\text{grid}} \tag{1.1}$$

where $X_{\text{grid}} = 2\pi \cdot \omega_{\text{grid},1} \cdot L_{\text{grid}}$. The angular frequency $\omega_{\text{grid},1}$ denotes the fundamental angular frequency of the grid voltage v_{grid}. The magnitude of the grid impedance Z_{grid} is determined by the available short-circuit power at the PCC S_{grid}. In terms of per-unit values (pu), the magnitude of the grid impedance follows the relation in (1.2).

$$Z_{\text{grid}} = \frac{1}{S_{\text{grid}}} \tag{1.2}$$

In the standards or grid codes, the grid impedance angle $\psi_{\text{grid}} = \arctan {}^{X_{\text{grid}}}/_{R_{\text{grid}}}$ is also used to express the composition between the resistive and inductive part. A lower ψ_{grid} indicates a more resistive grid impedance while a higher ψ_{grid} indicates a more inductive grid impedance.

Since the load or consumer sign convention is often used in grid codes [(ii)], the same convention is also applied in this thesis. This leads to the current and voltage direction as shown in Fig. 1.4a. If a wind turbine operates in generation mode i.e. it feeds power to the grid, the real part of the PCC current and active

[(ii)] In several standards such as in the IEEE 1547 [26] and IEC 61850-7-420 [27], distributed power generations are no longer considered as loads. Therefore, the generator convention is applied. In this case, the over- and underexcited operation are located in the quadrant 1 and 4 respectively if the active power flows into the power grid.

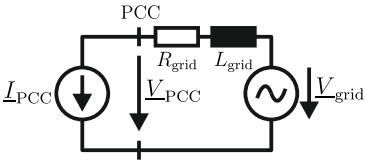

(a) Single-phase equivalent circuit diagram at PCC

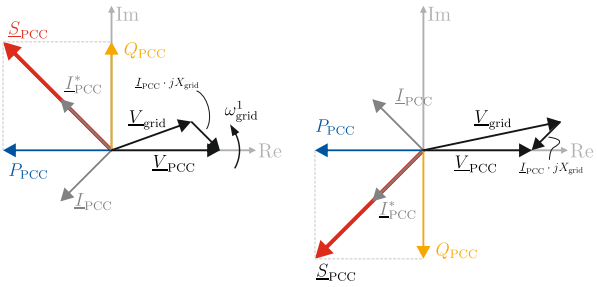

(b) Phasor diagram for diffferent cases of reactive power flow

Figure 1.4: Sign convention at PCC

power at the P_{PCC} become negative. The resulting phasors of the PCC voltage $\underline{V}_{\text{PCC}}$, current $\underline{I}_{\text{PCC}}$ and apparent power $\underline{S}_{\text{PCC}}$ with the applied sign convention are shown in Fig. 1.4b. When a wind turbine delivers reactive power Q_{PCC} to the grid (overexcited), the imaginary part of the PCC current is positive. Because, the apparent power $\underline{S}_{\text{PCC}}$ equals $\underline{V}_{\text{PCC}} \cdot \underline{I}^*_{\text{PCC}}$, the overexcited operation leads to a negative reactive power Q_{PCC}. Vice versa, the underexcited operation will lead to a positive sign for the Q_{PCC}.

2 Fundamental Wind Energy Conversion

2.1 Wind Energy Conversion

The conversion from kinetic energy in moving air into rotational energy in a wind turbine drivetrain is accomplished by the rotor blades. For a set of rotor blades with a radius R_{rotor}, the amount of the converted kinetic power into the rotational energy can be formulated as follows [28]

$$P_{\mathrm{aero}} = \frac{\pi}{2} \cdot \rho_{\mathrm{air}} \cdot R_{\mathrm{rotor}}^2 \cdot v_{\mathrm{wind}}^3 \cdot C_{\mathrm{p}}\left(\beta,\lambda\right) \tag{2.1}$$

where ρ_{air} is the density of air in $^{\mathrm{kg}}/_{\mathrm{m}^3}$ and v_{wind} is the wind speed in $^{\mathrm{m}}/_{\mathrm{s}}$. C_{p} is known as the power coefficient which describes the aerodynamic efficiency of the rotor blades. For a certain design of the rotor blades, C_{p} is a function of the pitch angle β and the unitless tip-speed ratio λ of the rotor blades:

$$\lambda = \frac{\Omega_{\mathrm{rotor}} \cdot R_{\mathrm{rotor}}}{v_{\mathrm{wind}}} \tag{2.2}$$

Ω_{rotor} in (2.2) denotes the angular rotation frequency of the rotor in $^{\mathrm{rad}}/_{\mathrm{s}}$. An example characteristic of a power coefficient C_{p} is plotted in Fig. 2.1. For this plot, the aerodynamic characteristic of the wind turbine in [29], [30] is taken into account. By adjusting the pitch angle β, a wind turbine controller is able manipulate the power coefficient to adjust the input power P_{aero}. Thereby, the tip-speed ratio λ can be selected depending on the wind speed such that the optimum power coefficient is achieved.

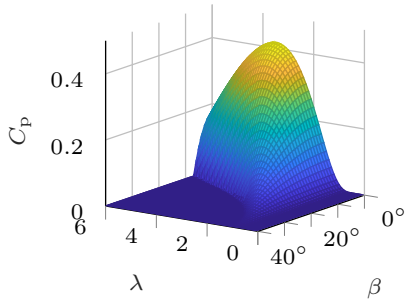

Figure 2.1: Power coefficient C_p for different tip-speed ratios λ and rotor blades pitch angle β in [29], [30]

2.2 Drivetrain Architectures

The task of a wind turbine drivetrain is to convert the rotational energy into grid-conform electrical energy. Depending on the size of the employed power-electronic converters, wind turbine drivetrain architectures can be classified into the partial-scale and the full-scale converter concept as shown in Fig. 2.2. In the partial-scale converter concept or also called doubly-fed generator concept, an asynchronous generator with a wound rotor is employed where its stator is coupled to the electrical grid via a step-up transformer to adjust the grid connection voltage [31], [32]. Thereby, the stator produces an air gap rotating magnetic field with the same frequency as the grid frequency. To enable a variable speed operation, a back-to-back voltage-source converter (VSC) is linked to the rotor circuit as shown in Fig. 2.2a to control the excitation. As only a fraction of the stator power flowing trough the rotor circuit, the converter needs to be rated to a fraction of the nominal power of wind turbine (typically 30 %). Wind turbines employing the partial converter concept are characterized by the installed 3-stage gearbox to couple the high-rotating generator shaft with the low-rotating rotor blades [32].

Different to the partial-scale converter concept, the full-scale converter concept employs a back-to-back power-electronics converter installed between the generator and electrical grid as depicted in Fig. 2.2b. Thereby, a higher flexibility in terms of the rotating speed of the generator is achieved thanks to the fully decoupled generator from the electrical grid via the converter. As the generator, other types such as asynchronous generator with squirrel-cage rotor, permanent-magnet synchronous generator, or electrically-excited synchronous generator are applicable here.

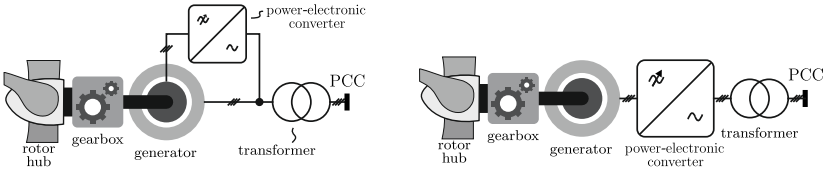

(a) Partial-scale converter concept (b) Full-scale converter concept

Figure 2.2: Drivetrain architectures variable-speed wind turbines in a multi-megawatt class [31], [33], [34]

Even though the partial-converter concept offers a benefit over the full-scale converter concept in terms of the cost of the converter, the report in [35] shows a trend shift towards the full-scale converter concept particularly in Europe and for a turbine's nominal power of higher than 2 MW. One reason for this trend shift is the introduction of low-voltage ride-through (LVRT) requirement in the grid codes which can induce severe stresses on the drivetrain components. Therefore, this thesis only considers full-scale converter wind turbines.

2.3 Power-Electronic Converter Architecture

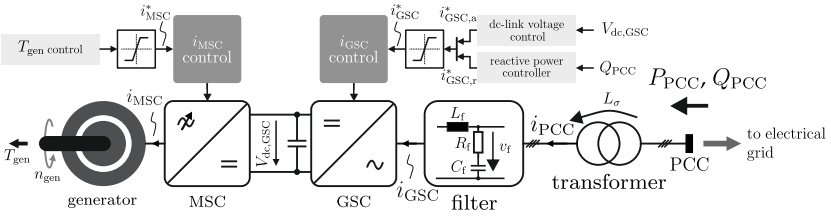

Figure 2.3: Power-electronic converter and control architecture of a wind turbine with a full-scale converter [33], [36], [37]

Figure 2.3 illustrates the topology and control architecture of a power-electronic converter for multi-megawatt wind turbines applying a full-scale converter concept. The converter consists of a machine-side converter (MSC) and a grid-side converter (GSC) connected via a direct current (DC) link. Beside rectifying the current of the generator which operates with a variable frequency, the machine-side converter is responsible for providing the generator torque T_{gen} requested by the wind turbine controller. Depending on the generator type, the torque control

algorithms elaborated in [38] can be implemented to perform this task.

The rectified dc current is inverted back to an ac current with a fixed frequency by the grid-side converter prior to the transmission to an electrical grid. To suppress the harmonic content in the current fed into the grid, a passively-damped LC filter is installed, which together with the stray inductance of a step-up transformer $L_{\sigma,\mathrm{WT}}$ forms an LCL filter. This filter setup is often selected to minimize the installation of bulky components and to reduce the converter footprint.

To accomplish its task, a grid-side converter applies a cascaded control structure as shown in Fig. 2.3. It consists of an inner current controller that regulates converter's terminal current i_{GSC} and two outer controllers, a dc-link voltage V_{dc} controller and a PCC reactive power Q_{PCC} controller [36], [37]. If the current controller is implemented on a synchronous reference frame thanks to the park transformation [39], it is possible to decouple the control on the active and reactive current $i_{\mathrm{GSC,a}}$ and $i_{\mathrm{GSC,r}}$.

2.4 Wind-Turbine Control Architecture

The objective of the wind-turbine controller is to operate the wind turbine at its optimum operating point taking the operation limits into account. Since the wind-turbine control strategy will have a substantial influence on the output power of a wind turbine next to the transmission dynamic of the drivetrain, the typical architecture of a wind-turbine controller is elaborated in this section. Figure 2.4 shows the typical control architecture of a variable speed wind turbine in a multi-megawatt class.

A wind-turbine control architecture consists of two functions, the rotor speed and the generator torque regulator. The rotor speed regulator adjusts the input power and torque T_{aero} via the pitch angle β to regulate the rotor rotational speed n_{rotor} to its nominal value $n_{\mathrm{rotor,N}}$. A proportional-integral (PI) controller can be employed to perform this task. When the speed error e_{n} is negative ($n_{\mathrm{rotor}} \leq n_{\mathrm{rotor,N}}$), the PI controller will lower the pitch angle to increase the input power P_{aero} (see Fig. 2.1). The movement of the pitch angle is usually limited to $0^\circ \leq \beta \leq 90^\circ$. Further, the rate of change of the pitch angle is limited to $\pm 3\,^\circ/\mathrm{s} \leq {}^{\mathrm{d}\beta}/_{\mathrm{d}t} \leq \pm 10\,^\circ/\mathrm{s}$ which limits the dynamic of the rotor speed regulator.

The operation point of a wind turbine at a certain wind speed is given by the gen-

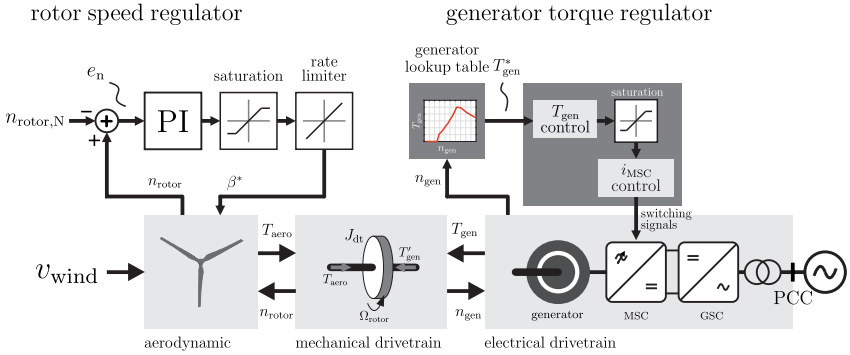

Figure 2.4: Typical control architecture of a variable-speed wind turbine [40]

erator torque regulator function. It is stored in a lookup table which outputs the reference generator torque T^*_{gen} depending on the measured generator rotational speed n_{gen}. The torque controller implemented within the machine-side converter will realize the generator torque reference on the generator shaft. To understand how the operating point of a wind turbine which are stored in the lookup table are determined, an exemplary derivation is explained in the following. For this example, the aerodynamic characteristic in Fig. 2.1 is taken into account.

The grey curves plotted in Fig. 2.5a are the aerodynamic power curves P_{aero} as a function of the rotor speed n_{rotor} for various wind speeds v_{wind} when the pitch angle β is set to 0°. If the wind turbine is operated at the points indicated by the blue circles, the power coefficient C_p is maximized thus a maximum converted aerodynamic power $P_{aero,max}$. However, due to the drivetrain efficiency η_{dt}, the target operation power point of the generator P^*_{gen} must be offset from the maximum power point along the grey curves. Hence, the target operation power of the generator P^*_{gen} for every wind speed can be defined as expressed in (2.3).

$$P^*_{gen}(n_{rotor}) = \begin{cases} 0, & \text{for } P^*_{gen} \leq P_{cut-in} \\ \eta_{dt} \cdot P_{aero,max}(n_{rotor}), & \text{for } P_{cut-in} \leq P^*_{gen} \leq P_N \\ P_N, & \text{for } P^*_{gen} \geq P_N \end{cases} \tag{2.3}$$

When considering a drivetrain efficiency $\eta_{dt} = 90\,\%$, the resulting operating point of the generator are shown by the red squares in Fig. 2.5a. It must be noted that for high wind speeds, the generator power is limited to its nominal power P_N.

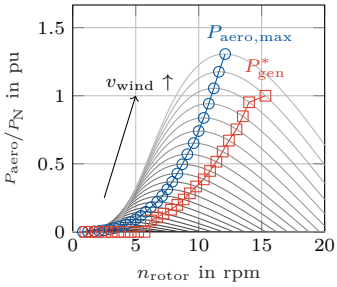

(a) Power curve at $\beta = 0°$

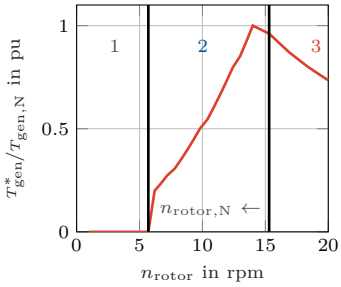

(b) Generator operation baseline

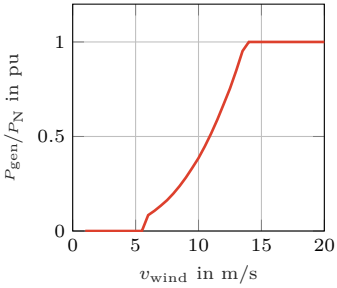

(c) Baseline power curve

Figure 2.5: Derivation of a generator lookup table considering the aerodynamic characteristic in Fig. 2.1

Vice versa, the generator power is set to zero if the wind speed is lower then the so-called cut-in wind speed. Below the cut-in wind speed, the wind power is too low to compensate its internal power consumption.

Finally, the reference generator torque as a function of the rotor rotational speed n_{rotor} in rpm is calculated by

$$T^*_{\text{gen}}(n_{\text{rotor}}) = \frac{P^*_{\text{gen}}(n_{\text{rotor}})}{n_{\text{rotor}}} \cdot \frac{60}{2\pi} \tag{2.4}$$

For wind turbines equipped with a gearbox, the rotational speed on the generator side n_{gen} can be obtained by multiplying n_{rotor} with the transmission ratio of the

gearbox.

The resulting baseline of the reference generator torque as a function of the rotational rotor speed for this example is given in Fig. 2.5b. Here, the typical three regions of operation [40] can be seen. Region 1 represents the situation where the wind speed is lower than the cut-in wind speed. Region 2 is the optimum power production mode where the wind turbine operates at the maximum power point considering the power coefficient C_p, rotor speed n_rotor and the drivetrain efficiency η_dt. Region 3 is the constant power operation where the generator power is limited to its nominal power of the turbine.

Figure 2.6 shows a simulated operation of a wind turbine equipped with the above described control architecture under a varying wind speed. For this simulation, the mechanical drivetrain is approached by a one rotating mass having a moment inertia $J_\mathrm{dt} = 4 \cdot 10^6 \mathrm{kg\,m^2}$. Thus, the dynamic equation of the mechanical drivetrain can be expressed as follows

$$T_\mathrm{aero} - T_\mathrm{gen} = J_\mathrm{dt} \cdot \frac{\mathrm{d}\Omega_\mathrm{rotor}}{\mathrm{d}t} \tag{2.5}$$

Ω_rotor denotes the angular rotational speed of the rotor in $^\mathrm{rad}/_\mathrm{s}$ and T_aero represents the shaft torque as a result of the input power P_aero.

As expected, when the wind speed is still low at the beginning of the simulation, the wind-turbine controller sets the rotor pitch angle to the lowest possible value $\beta = 0^\circ$ to accelerate the rotor speed. On the other side, the generator torque T_gen is provided according the baseline curve in Fig. 2.5b. As a result, the wind turbine stays at the steady-state point defined by the generator baseline curve. The wind-turbine controller is not able to increase the rotor rotational speed as there is no more input power available.

As the wind speed increases, the wind turbine behaves similarly with $\beta = 0^\circ$ until the nominal values of the generator torque and power as well as the rotor speed are reached at $t = 166\,\mathrm{s}$. Beyond this instance, the wind turbine enters the constant power region which is indicated by a constant generator power although the wind speed further rises. The wind turbine controller keeps the generator power constant by increasing the pitch angle β because the input power to the drivetrain is inversely proportional to the power coefficient C_p (refer to Fig. 2.1). Thus, the rotor rotational speed n_rotor is maintained at its nominal setpoint.

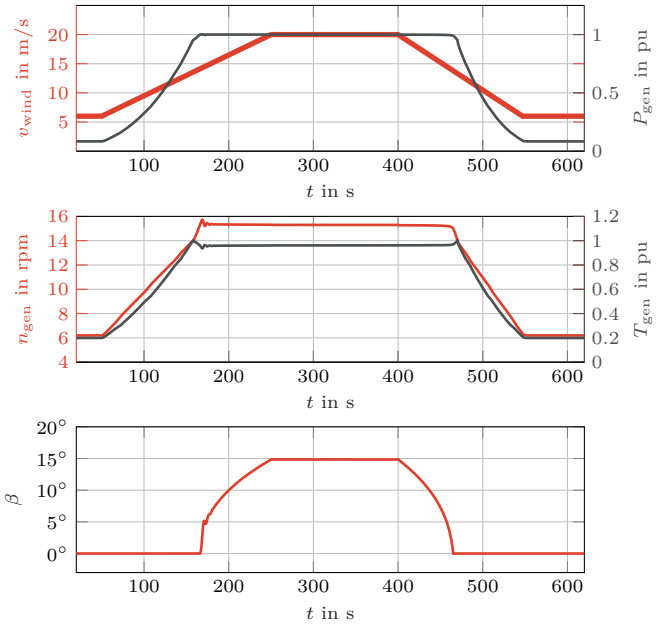

Figure 2.6: Operation simulation of a wind turbine at a varying wind speed

2.5 A 2.75 MW Reference Wind Turbine

In this thesis, the validation of the analysis is conducted using a 2.75 MW reference wind turbine nacelle at the Center for Wind Power Drives (CWD), RWTH Aachen University in Aachen, Germany. This reference wind turbine is also called FVA nacelle. Its generic character allows an open data mining inside the nacelle to assess the behavior of WT components as well as their interactions in wide varieties of operational situations. The behavior of the missing rotor and blades is simulated and emulated at the rotor flange in real time as described in detail in [13], [14], [41]–[44]. Thereby, the FVA nacelle operates with its controller as it would operate in the field. The final setup of the FVA nacelle is shown in Fig. 2.8b.

The FVA nacelle was developed based on a commercial wind turbine Vestas NEG Micon NM80 [45] with a nominal power of 2.75 MW. Unlike the original configuration, FVA nacelle adopts the geared drivetrain concept employing a high-speed

asynchronous generator coupled to a full-scale power electronic back-to-back converter system (fsc) as depicted in Fig. 2.8. The power electronic converter system comprises three sychronously-switched low-voltage converters connected in parallel on both alternating current (AC) and DC side [46]. Each converter unit is equipped with an LC filter on the grid side which together with the stray inductance of a step-up transformer forms an LCL filter configuration. The step-up transformer is necessary since the voltage at the PCC is 20 kV while the power electronic converters are rated to an AC voltage of 690 V. In the DC-link, a DC chopper is installed to prevent dc-link overvoltages, for instance during the occurance of grid voltage dips.

The wind turbine controller of the FVA nacelle communicates with the MSC via a Profibus DP communication link [47]. It allows a maximum communication transfer rate of 100 Hz. Hence, the torque control implemented in the MSC receives the setpoints in 10 ms interval after a new operation point is set by the wind turbine controller. The key specification of the nacelle is given in Table 2.1.

To enable detailed investigation on nacelle's behavior deep until the component level, about 300 mechanical and electrical sensors are installed inside the FVA nacelle. To ensure a sophisticated signal quality in terms of the electromagnetic interference noise and signal synchronicity, a data acquisition (DAQ) architecture shown in Fig. 2.8c is applied. The output signals of the sensors are collected and locally digitalized by means of sensor terminals. This avoid a long analog connections which may deteriorate the signal quality. The digitalized signals are sent via a Precision Time Protocol (PTP) network [48] to the user interface terminal for visualization purpose as well as to a data storage system to secure the acquired data. By means of PTP network protocol, a signal synchronization up to 2 µs is possible allowing a signal sampling frequency up to 20 kHz with a negligibly error. Thereby, typical electrical measurement tasks for characterization of wind turbines are possible.

In Fig. 2.9, the measured operation behavior of the FVA nacelle is shown. Similar to the aforementioned control scheme of a wind turbine, the controller of the FVA nacelle regulates the rotor speed to its nominal value $n_{\mathrm{rotor}} = 17.5\,\mathrm{rpm}$ by setting the pitch angle β. On the other hand, the generator follows a certain characteristic line shown in Fig. 2.7. At a low wind speed as in Fig. 2.9a, the pitch angle already reaches its minimum $\beta = 0^\circ$ even though the nominal rotor speed is not yet reached. Thus, the reaction of the FVA nacelle is defined by the generator characteristic line and the aerodynamic characteristic as mentioned before. Since the wind velocity is fluctuating, the resulting rotor speed n_{rotor} and output power at the grid connection point P_{PCC} are fluctuating as well.

Table 2.1: Nominal values of the FVA nacelle

Parameter	Symbol	Value
Power	$P_{\mathrm{WT,N}}$, $S_{\mathrm{WT,N}}$	2.75 MW, 3.05 MVA
Low-speed-shaft speed	$n_{\mathrm{rotor,N}}$	17.5 rpm
High-speed-shaft speed	$n_{\mathrm{gen,N}}$	1100 rpm
Rotor swept area	A_{rotor}	5027 m^2
Turbulence intensity	I_{wind}	16 %
Operating wind speed	v_{wind}	4.5 ... 25 $\mathrm{m/s}$
PCC voltage	$V_{\mathrm{PCC,N}}$	20 kV
Generator		
Type		ASG with wound rotor
Voltage	$V_{\mathrm{gen,N}}$	720 V
Current	$I_{\mathrm{gen,N}}$	2564 A
Frequency	$f_{\mathrm{gen,N}}$	54.5 Hz
Torque	$T_{\mathrm{gen,N}}$	24.7 kNm
Power-electronic converter		
Topology		two-level VSC
DC-link voltage	$V_{\mathrm{dc,GSC}}$	1050 V
DC-link capacitor	$C_{\mathrm{dc,GSC}}$	92.4 mF
Switching frequency	f_{sw}	3.2 kHz
Modulation		flat-top modulation
Equivalent grid filter parameter	L_{f}, C_{f}, R_{f}	33.3 µH, 2.1 mF, 7.8 mΩ
Cooling IGBT modules		water cooling
Transformer		
Power	$S_{\mathrm{TR,N}}$	3.5 MVA
Short-circuit impedance	$S_{\mathrm{sc,TR}}$	7.5 %
Field bus communication		
Protocol		Profibus DP
Transmission rate		100 Hz

At a high average wind speed like depicted by Fig. 2.9b, the rotor rotational speed n_{rotor} reaches its nominal and so does the generator torque T_{gen}. In contrast to the above mentioned strategy, beyond its nominal rotor speed, the FVA nacelle limits the generator torque T_{gen} to its nominal value $T_{\mathrm{gen,N}}$ instead of reducing it to maintain the output power constant. Consequently, a short-term higher generator power than the nominal value is allowed. Such a strategy must be carefully coordinated with the maximum deliverable generator torque in field-weakening operation. As the wind can provide power higher then the nominal power of the turbine, the controller of the FVA nacelle increases the pitch angle β to regulate the rotor rotational speed to its nominal value. This is indicated by the pitch angle curve in Fig. 2.9b which is higher than the pitch angle at the lower average wind speed V_{wind} in Fig. 2.9a.

Figure 2.9 also reveals that the dc-link voltage controller of the power electronic converter of the FVA nacelle has a much higher bandwidth compared to the

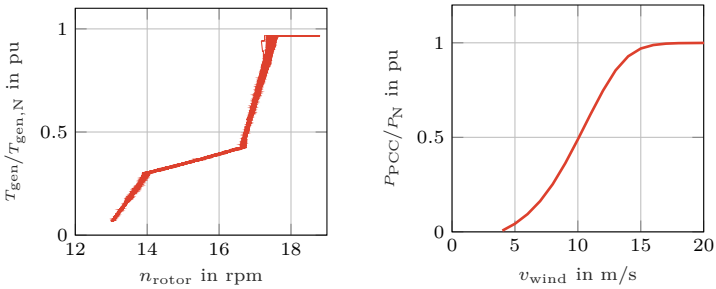

(a) Measured generator operation points

(b) Baseline power curve from datasheet

Figure 2.7: Operation baseline of the FVA nacelle

dynamics of the power transmission from the generator to the grid. This is indicated by the dc-link voltage curve V_{dc} in Fig. 2.9. It remains constant even though the power P_{PCC} is fluctuating with a peak-to-peak value of more than 0.5 pu. This is an important information for system level modeling as well as the analysis of output power fluctuation of a wind turbine discussed in Chapter 3.

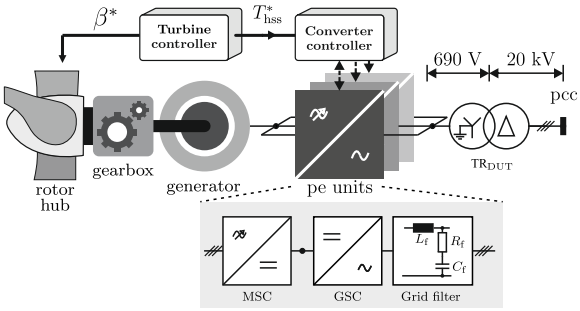

(a) Schematic

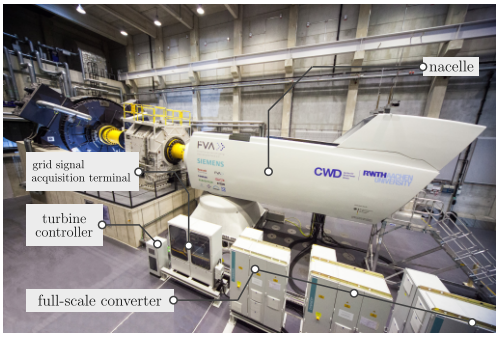

(b) Final assembly on CWD test bench

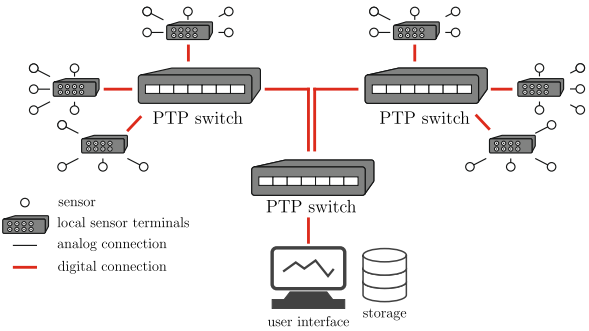

(c) Distributed data acquisition (DAQ) system architecture

Figure 2.8: FVA nacelle setup

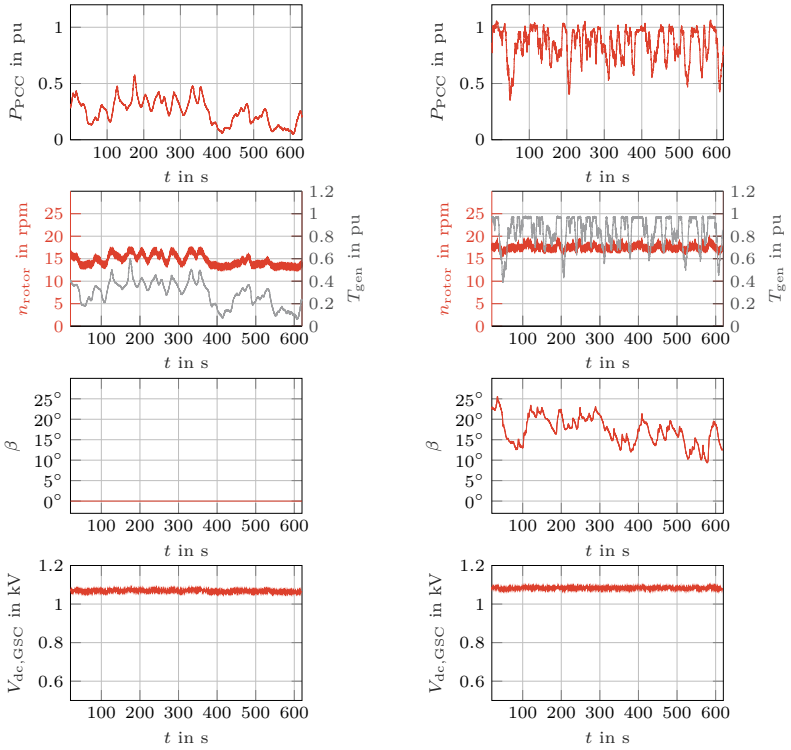

(a) Average wind speed $V_{\mathrm{wind}} = 8\,\mathrm{m/s}$

(b) Average wind speed $V_{\mathrm{wind}} = 20\,\mathrm{m/s}$

Figure 2.9: Measured operation behavior of the FVA nacelle under a low and high wind speed

3 Output Power Fluctuations

One drawback of wind turbines compared with other power generations is their fluctuating output power [28]. This can be seen in the output power of the FVA nacelle depicted in Fig. 2.9. Short-term power fluctuations have gained a special attention because they can induce severe flicker in the electrial grid with a potential negative effect for humans. Therefore, flicker severity level must be limited and verified for every different wind turbine prior to the grid integration.

However, measurements of flicker is one of the most time-consuming task in a certification program. The measurements have to be conducted for the entire range of wind conditions. With the wind conditions in the field being uncontrollable, flicker measurements become very challenging, costly as well as resource intensive. If flicker measurements are performed on a wind turbine test bench, enormous time and cost savings are achievable thanks to the operation conditions being controllable and reproducible. Furthermore, more accurate results are possible which will be elaborated further in this thesis.

This chapter aims to analyze the output power fluctuation of wind turbines in particular the origins, their characteristic and finally their contribution to flicker. These steps are necessary in order to correctly derive the dynamic requirement for the grid emulator if flicker measurements are supposed to be performed on a test bench. Similarly, the origins of power fluctuation that must be correctly emulated by the wind load emulator can also identified. This chapter is structured as follows. Firstly, the definition, measurement, and characteristic of flicker is discussed. Afterwards, the potential origins for the output power fluctuation of wind turbines are introduced and the contribution to the flicker is identified considering a wind turbine model in Fig. 2.4. The analysis is verified via measurements on the reference nacelle introduced in 2.5.

3.1 Flicker

Definition

According to the International Electrotechnical Commission (IEC), flicker is defined as an impression of unsteadiness of visual sensation induced by a light stimulus whose luminance or spectral distribution fluctuates with time [49]. The formal definition for flicker adopted by the Institute of Electrical and Electronics Engineers (IEEE) is a change in the luminous flux of a lamp or illuminant due to fluctuations in the voltage of the power supply [50]. Flicker can lead to negative biological effects on humans ranging from convenience problems to headaches or eyestrains.

In case of wind turbines, voltage fluctuations are caused by the fluctuating nature of their output power resulting in a fluctuating fed-in current to the electrical grid. Referring to the sign convention in Fig. 1.4, the voltage at the grid connection point or PCC is described by:

$$\underline{V}_{\mathrm{PCC}} = \underline{V}_{\mathrm{grid}} - \underline{I}_{\mathrm{PCC}} \cdot \underline{Z}_{\mathrm{grid}} \tag{3.1}$$

For a given grid impedance $\underline{Z}_{\mathrm{grid}}$, once the fed-in current by a wind turbine $\underline{I}_{\mathrm{PCC}}$ fluctuates, the voltage drop across the grid impedance (the second term in (3.1)) varies accordingly. This leads to a variation in the PCC voltage $\underline{V}_{\mathrm{PCC}}$ which results in a flicker phenomenon in the consumer ends. Figure 3.1 plots the magnitude variation in the PCC voltage to its value under no-load condition ΔV_{PCC} as a function of wind turbine active power P_{PCC}. The plots are given for various grid short-circuit power S_{grid} and grid impedance angles θ_{grid}.

It is seen from Fig. 3.1 that the higher the grid impedance Z_{grid} is i.e. the lower short circuit power S_{grid}, the more sensitive is the PCC voltage V_{PCC} to the variation in the delivered active power P_{PCC} by a wind turbine. Furthermore, this figure shows that the grid impedance angle θ_{grid} substantially affects ΔV_{PCC}. A less resistive grids indicated by the higher grid impedance angle θ_{grid} will result in less voltage power dependent voltage variations. Therefore, when calculating flicker severity levels, a resistive grid ($\theta_{\mathrm{grid}} = 30°$) with a low grid short-circuit power($S_{\mathrm{grid}} = 3\,\mathrm{pu}$) is considered in this chapter. An electrical grid with a low short-circuit power is also associated to a weak grid.

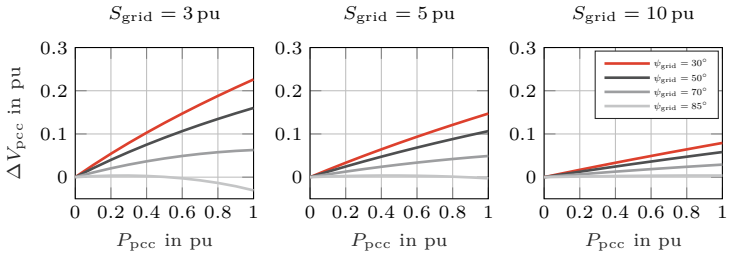

Figure 3.1: PCC voltage deviation to its nominal value (ΔV_{PCC}) as a function of the fed-in power and the grid impedance. $Q_{\text{PCC}} = 0\,\text{pu}$

Measurement

The flicker intensity is described by the so-called short-term and long-term flicker severity level P_{lt} and P_{st} respectively. They differ mainly in the duration of the assessment interval. The short-term severity level P_{st} considers a measurement interval of 10 minutes whereas 120 minutes of a measurement interval are taken to examine the long-term severity level P_{lt}. The long-term severity level is mainly intended to capture flicker phenomena which due to their low occurance frequency take effect after a longer time compared to the time frame of P_{st}. For this thesis, the short-term P_{st} is the most relevant one to consider. Hence, the long-term severity level will not be discussed further in this thesis.

The measurement procedure to determine P_{st} is standardized in the IEC standard 61000-4-15 [51], [52]. To obtain the flicker severity level P_{st} out of a fluctuating voltage signal, the IEC flickermeter process chain presented in Fig. 3.2a is used. It consists of three main processes: input signal pre-conditioning (Block 1), model of human perception on time-varying luminance of lamps (Block 2, 3 and 4) and determination of severity level of voltage flicker based on statistic (Block 5). The second section of the IEC flickermeter is constructed based on the modeling of human's impression on unsteadiness of visual sensation induced by fluctuating luminance of light stimulus which is proposed and validated in [53].

Due to the processes within the IEC flickermeter, it gives a different response for different voltage waveforms. Detailed discussions on this topic can be found in [54]. Nonetheless, the response to the test voltage waveform in Fig. 3.2b is plotted in Fig. 3.2c. As the test voltage, a low-frequency sinusoidal signal with an amplitude $\hat{V}_{\text{lf}}$ representing the time-varying magnitude fluctuation of the PCC voltage is modulated to a 50 Hz sinusoidal voltage. The coloring from red to light

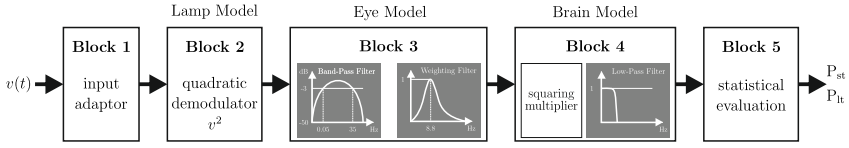

(a) Flickermeter process chain

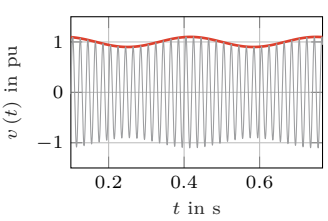

(b) Test voltage

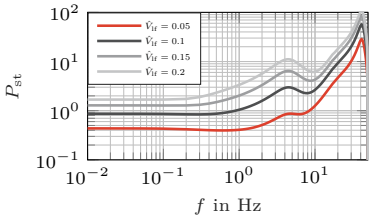

(c) Response plot

Figure 3.2: IEC flickermeter

grey in Fig. 3.2c indicates an increasing amplitude of the low-frequency sinusoidal signal. In Fig. 3.2c, the response of IEC flickermeter in terms of P_{st} for different amplitudes and frequencies of the low-frequency signal.

It can be seen in this figure that the frequency of the modulated signal has a strong influence on the flicker severity level P_{st} next to its amplitude. The influence of frequency becomes more significant at frequencies higher than 1 Hz. This means that the dynamic requirement on the grid impedance emulation by a grid emulator becomes stricter. Therefore, in order to derive a proper dynamic requirement on the grid impedance emulation by a grid emulator for flicker measurements, the frequency characteristic of the power fluctuations caused by wind turbines as well as the resulting voltage fluctuations must be analyzed in this chapter.

It must be noted that voltage harmonics may have an influence on the output of the IEC flickermeter as reported in [55]. However, for flicker measurements the IEC standard 61400-21 [24] allows a sampling rate of 2 kHz for the current and voltage measurements. When considering the entire data acquisition chain including the anti-aliasing filter, it results in a measurement bandwidth of only about 200 Hz. Since harmonics also occur beyond this frequency, the influence of harmonics is minimum. Therefore, it is neglected in this thesis.

3.2 Origins of Power Fluctuations

3.2.1 Wind Turbulences

As the movement of air in the fields is irregular, the wind speed v_{wind} shows a fluctuating behavior. This irregular air movement can be attributed to several factors e.g. the profile of the surrounding terrains, the air temperature, the wakes produced by neighbouring wind turbines and many other factors. This phenomenon is also called turbulence. Consequently, the converted power by the rotor blades P_{aero} fluctuates correspondingly (refer to (2.1)). According to [30], [56], [57], the wind turbulence follows a stochastic behavior and can be approached by the gaussian probability distribution function [58]. The intensity of wind turbulence I_{wind} is described by

$$I_{\mathrm{wind}} = \frac{\sigma_{\mathrm{wind}}}{V_{\mathrm{wind}}} \cdot 100\,\% \tag{3.2}$$

σ_{wind} in (3.2) denotes the standard deviation of wind speed while V_{wind} expresses the average wind speed. Figure 3.3 exemplarily shows the time series curves of a turbulent wind speed $v_{\mathrm{wind,t}}$ with three different turbulence intensities I_{wind}. The probability curve of these curves fitted to the normal distribution function are plotted in Fig. 3.3. In this example, the average wind speed is $12\,\mathrm{m/s}$.

In Fig. 3.3, it is shown that a higher turbulence intensity results in a wider variance of the wind speed. This indicates that the instantaneous wind speed containing turbulence component $v_{\mathrm{wind,t}}$ has a wider span between its highest and lowest value. As shown in the time series plot, the instantaneous wind speed $v_{\mathrm{wind,t}}$ may reach a span of $12\,\mathrm{m/s}$. In terms of wind turbine input power P_{aero}, this means a power span as high as $0.6\,\mathrm{pu}$ when considering the power curve in Fig. 2.9. Furthermore, the time series curves indicate that a higher I_{wind} also causes $v_{\mathrm{wind,t}}$ to fluctuate more frequently. Thus, it is expected that the flicker severity level $\mathrm{P_{st}}$ will increase with a greater turbulence intensity.

3.2.2 Tower Shadowing Effect

Next to wind turbulences, input power fluctuations of a wind turbine P_{aero} can be caused by the so-called tower shadowing effect. When a rotor blade of a wind turbine is passing the tower during rotation, the air flow passing the rotor blade

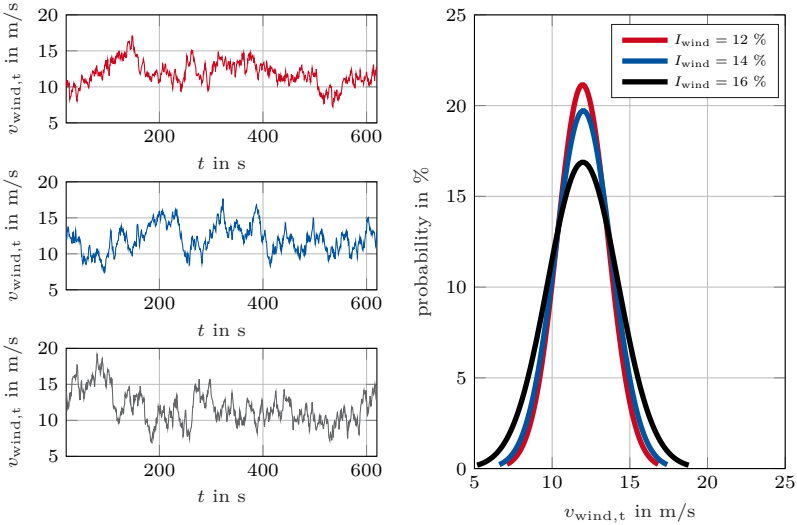

Figure 3.3: Probability of instantaneous wind speed v_{wind} due to turbulence at $V_{\mathrm{wind}} = 16\,\mathrm{m/s}$

is disturbed. Thereby, the torque on the rotor shaft produced by this particular rotor blade deteriorates. Consequently, the effective input power of the wind turbine experiences a periodical dip with a frequency triple the rotational frequency of the shaft for three-blades wind turbines. The tower shadowing frequency can be written as follows

$$f_{\mathrm{ts}} = \frac{3 \cdot n_{\mathrm{rotor}}}{60}. \tag{3.3}$$

Due to this reason, this phenomenon is also known as the 3P torque oscillation [59]–[61].

Sorenson et al. [56] and Dolan et al. [60], [62] introduced the concept of "equivalent wind speed" that can be used for wind turbine simulations. The instantaneous equivalent wind speed $v_{\mathrm{wind,eq}}$ accounting turbulence phenomenon $v_{\mathrm{wind,t}}$ and the tower shadowing effect $v_{\mathrm{wind,ts}}$ can be described by:

$$v_{\mathrm{wind,eq}} = v_{\mathrm{wind,t}} + v_{\mathrm{wind,ts}} \text{ in m/s} \tag{3.4}$$

The second part of (3.4) expresses the tower shadowing effect which can be written as [60], [62]:

$$v_{\mathrm{wind,ts}} = \frac{mV_{\mathrm{wind}}}{3R_{\mathrm{rotor}}^2} \sum_{b=1}^{3} \left[\frac{R_{\mathrm{t}}^2}{\sin^2\theta_{\mathrm{b}}} \ln\left(\frac{R_{\mathrm{rotor}}^2 \sin^2\theta_{\mathrm{b}}}{x_{\mathrm{bt}}^2} + 1 \right) - \frac{2R_{\mathrm{t}}^2 R_{\mathrm{rotor}}^2}{R_{\mathrm{rotor}}^2 \sin^2\theta_{\mathrm{b}} + x_{\mathrm{bt}}^2} \right] \tag{3.5}$$

where $m \approx 1$. R_{t} denotes the tower radius in meter. Angle θ_{b} is the angle between the rotor blade b and the vertical axis in radian. The angle θ_{b} indicates the instantaneous position of the rotor blade b. x_{bt} is the distance from the blade origin and to the tower midline in the longitudinal direction in meter. For clarity, the variables in (3.5) are visualized in Fig. 3.4a. It is worth to mention that (3.5) is only valid for $90° \leq \theta_{\mathrm{b}} \leq 270°$. A waveform example of $v_{\mathrm{wind,ts}}$ normalized to the average wind speed V_{wind} is given in Fig. 3.4b. For this example, $R_{\mathrm{rotor}} = 40\,\mathrm{m}$, $R_{\mathrm{t}} = 2.5\,\mathrm{m}$ and $x_{\mathrm{bt}} = 5.4\,\mathrm{m}$ are taken into account which are reasonable values for a 3 MW wind turbine.

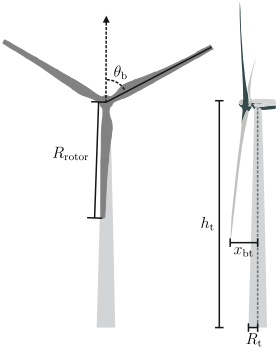

(a) Geometry of a wind turbine to calculate $v_{\mathrm{wind,ts}}$

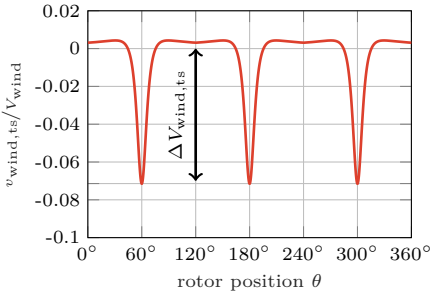

(b) Turbulence component in the equivalent wind speed $v_{\mathrm{wind,ts}}$

Figure 3.4: Influence of tower shadowing on the instantaneous equivalent wind speed $v_{\mathrm{wind,eq}}$

As depicted in Fig. 3.4b, the tower shadowing induces three dips in the equivalent wind speed within one rotor rotation. Besides, the magnitude of the dips can reach 7 % of the mean wind speed when considering the aforementioned turbine geometry. As compared to wind turbulence, the magnitude of wind speed fluctuation is much lower. Several publications such as in [59] show that the tower shadowing effect presents a less dominant effect on the output power fluctuation although flicker severity level was not used as an evaluation parameter. However, the results presented in [63] indicate that the tower shadowing effect has a substantial contribution on flicker. Due to these contradicting conclusions in the publication, the contribution of the tower shadowing to the induced flicker is elaborated in this section.

First, the resulting aerodynamic torque pulsation due to tower shadowing effect needs to be derived. Second, the resulting generator rotational speed pulsation taking the drivetrain dynamic into account is deduced in order to obtain the transmitted power pulsation onto the generator side. For this purpose, a turbulence intensity of 0 % is assumed thus $v_{\mathrm{wind,t}} = V_{\mathrm{wind}}$ and $v_{\mathrm{wind,eq}} = v_{\mathrm{wind,ts}}$.

By substituting v_{wind} in (2.1) with (3.4), the aerodynamic torque considering tower shadowing effect can be rewritten as given in (3.6).

$$T_{\mathrm{aero}} = \frac{\pi}{2} \cdot \rho_{\mathrm{air}} \cdot R_{\mathrm{rotor}}^2 \cdot \left(V_{\mathrm{wind}} + v_{\mathrm{wind,ts}}\right)^3 \cdot \frac{C_{\mathrm{p}}\left(\beta,\lambda\right)}{\Omega_{\mathrm{rotor}}} \text{ in Nm} \tag{3.6}$$

Assuming that the power coefficient C_{p} is unaffected by the tower shadowing effect and the resulting oscillation of the rotor angular speed is small enough compared to its average value, the waveform of T_{aero} will have a similar waveform as the waveform of $v_{\mathrm{wind,ts}}$ in Fig. 3.4b but differ in the amplitude. To derive the output power fluctuation on the generator side analytically, the waveform of T_{aero} is approached as depicted by the black curve in Fig. 3.5.

T_{ts} denotes the period of the torque fluctuation in seconds which equals one third of the rotor rotating period. $d \cdot T_{\mathrm{ts}}$ represents the width of the torque dip. $T_{\mathrm{aero,0}}$ is the aerodynamic torque at $v_{\mathrm{wind,ts}} = 0\,\mathrm{m/s}$. If the generator torque T_{gen} is constant which equals the average aerodynamic torque $\bar{T}_{\mathrm{aero}}$ in steady state condition, the rotor speed equation becomes

$$\Omega_{\mathrm{rotor}} = \frac{1}{J_{\mathrm{dt}}} \int \left(T_{\mathrm{aero}} - T_{\mathrm{gen}}\right) \mathrm{d}t. \tag{3.7}$$

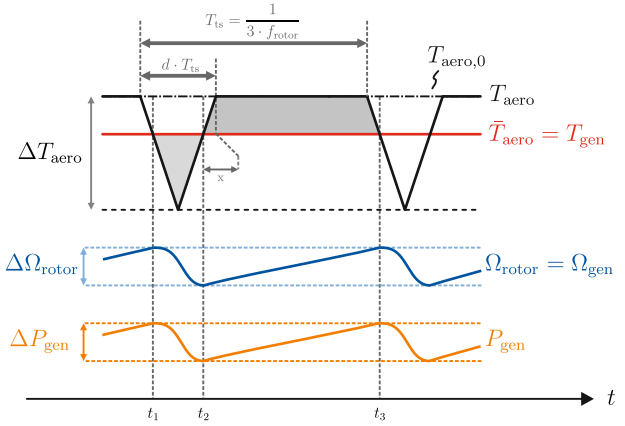

Figure 3.5: Waveform approximation of torques and speed due to the tower shadowing effect

At steady state condition, the grey-shaded areas are equal. Hence, the peak-to-peak value of the rotor speed oscillation $\Delta\Omega_{rotor}$ can be obtained by evaluating (3.7) either between t_1 and t_2 or between t_2 and t_3. In (3.8), the time range between t_2 and t_3 is considered.

$$\begin{aligned}\Delta\Omega_{rotor} &= \frac{1}{J_{dt}} \int_{t_2}^{t_3} (T_{aero} - T_{gen})\,\mathrm{d}t \\ &= \frac{1}{J_{dt}} \left[(T_{aero,0} - T_{gen}) \cdot (1-d) \cdot T_{ts} + (T_{aero,0} - T_{gen}) \cdot x\right]\end{aligned} \tag{3.8}$$

where

$$x = \frac{T_{aero,0} - T_{gen}}{\Delta T_{aero}} \cdot \frac{1}{2} \cdot d \cdot T_{ts} \tag{3.9}$$

Thus,

$$\Delta\Omega_{rotor} = \frac{1}{J_{dt}} (T_{aero,0} - T_{gen}) \left[(1-d) + \frac{T_{aero,0} - T_{gen}}{\Delta T_{aero}} \cdot \frac{1}{2} \cdot d\right] T_{ts} \tag{3.10}$$

The generator torque T_{gen} can be obtained by averaging the aerodynamic torque waveform over one period T_{ts}

$$\begin{aligned} T_{\mathrm{gen}} = \bar{T}_{\mathrm{aero}} &= \frac{1}{T_{\mathrm{ts}}} \left(T_{\mathrm{aero},0} \cdot T_{\mathrm{ts}} - \frac{1}{2} \cdot d \cdot \Delta T_{\mathrm{aero}} \cdot T_{\mathrm{ts}} \right) \\ &= T_{\mathrm{aero},0} - \frac{1}{2} \cdot d \cdot \Delta T_{\mathrm{aero}} \end{aligned} \tag{3.11}$$

Finally, the peak-to-peak value of the power on the generator side ΔP_{gen} is obtained by (3.12) which is graphically shown in Fig. 3.6. ΔP_{gen} in this figure is calculated for various ΔT_{aero} and drivetrain moment of inertia J_{dt}. For this figure, $d = \dfrac{0.7\,\mathrm{rad}}{2 \cdot \pi / 3\,\mathrm{rad}} = 0.33$ as shown in the example in Fig. 3.4b is considered.

$$\Delta P_{\mathrm{gen}} = T_{\mathrm{gen}} \cdot \Delta \Omega_{\mathrm{rotor}} \tag{3.12}$$

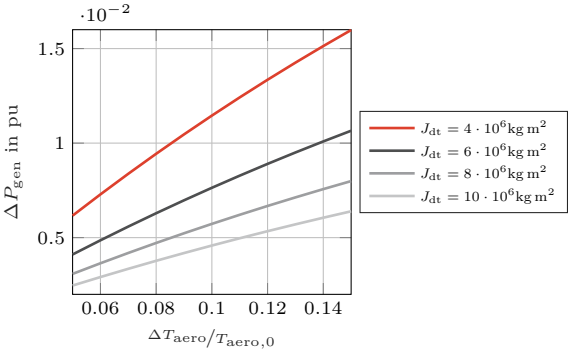

Figure 3.6: Power pulsation magnitude on the generator side of a wind turbine due to tower shadowing effect

Figure 3.6 reveals that the power oscillation on the generator side caused by the tower shadowing is far smaller than the power fluctuation magnitude caused by turbulent wind. For the example turbine geometry used to obtain the waveform in Fig. 3.4b, the power oscillation of less than 0.01 pu (indicated by the red curve). Furthermore, the power oscillation is less severe with a higher moment of inertia of the rotor which is also described analytically in (3.8). Wind turbines dedicated for weak wind speed operations are typically equipped with longer rotor blades that add mass to the rotor assembly thus a higher moment of inertia. Therefore,

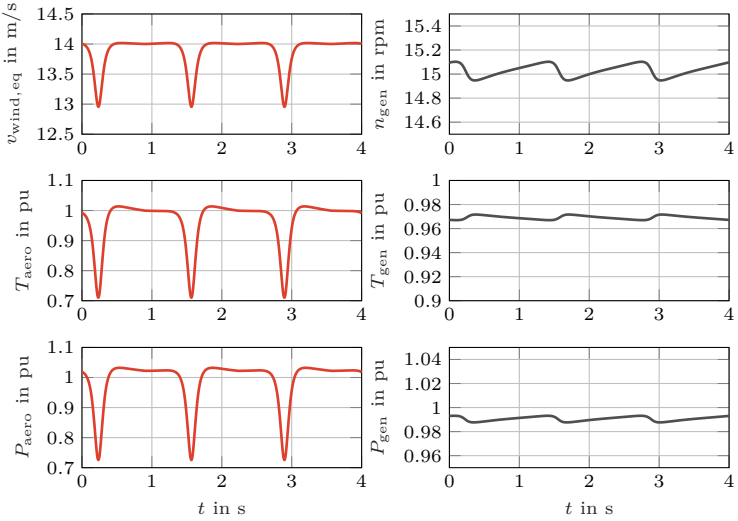

Figure 3.7: Wind turbine simulation considering tower shadowing effect at an average wind speed of $V_{\mathrm{wind}} = 14\,\mathrm{m/s}$ and 0 % turbulence intensity

it is expected that the power oscillations due to tower shadowing effects in these wind turbines are less severe.

Nevertheless, in case of low turbulence intensities, the contribution in the power oscillation from the tower shadowing effect can be significant in particular for wind turbines with a low rotor moment of inertia. Additionally, the power oscillation frequency is located in the range where it could induce a severe flicker (refer to Fig. 3.2c). Hence, it is worth investigating the flicker induced by tower shadowing effect to be able to correctly derive the requirements on the grid emulator.

To confirm the analytical calculations presented above, a simulation of the wind turbine in Fig. 2.4 considering the geometry in Fig. 3.4b is carried out. The simulation results are shown in Fig. 3.7. As expected, the tower shadowing effect causes dips in the input power of the wind turbine. However, the fluctuation in the generator power P_{gen} is significantly lower than in the aerodynamic power. This confirms the analytical calculation given in Fig. 3.6. Besides, the pulsation in the generator speed is very low such that the generator torque T_{gen} controlled by the machine-side converter is almost constant making the above assumption is valid.

3.2.3 Drivetrain Resonance

Unlike the previously mentioned causes for power fluctuations that are related to the input power to the wind turbine drivetrain, drivetrain oscillations originate at the drivetrain eigenfrequencies. The wind turbine drivetrain is a complex system and may contain many eigenfrequencies depending on the drivetrain architecture. Unlike the simplified modeling of a wind turbine drivetrain in Fig. 2.4, the model of a wind turbine drivetrain is typically extended to a two or more rotating mass model. An example of a three-rotating-mass model is shown in Fig. 3.8. Here three masses having an inertia J in $\mathrm{kg\,m^2}$ are linked to each other via a spring-damper system with spring constants k in $^{\mathrm{N\,m}}/_{\mathrm{rad}}$ and damping constants c in $^{\mathrm{N\,m\,s}}/_{\mathrm{rad}}$. Since such a system is capable of resonating which may lead to drivetrain oscillations during the operation.

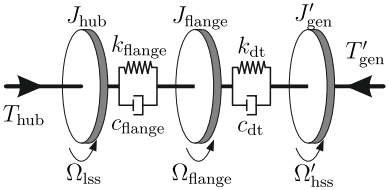

(a) Three-mass model

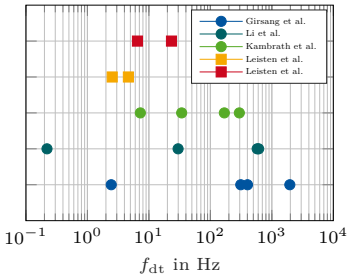

(b) Drivetrain eigenfrequencies of various turbines [43], [44], [64]–[66]

Figure 3.8: Wind turbine drivetrain representation as a three-rotating-mass model

Figure 3.8 shows the eigenfrequencies of different WT found in several publications. This figure reveals that a wind turbine drivetrain can have multiple eigenfrequencies from subsychronous which are particularly relevant for voltage flicker. These resonances may be excited during the operation causing oscillations and thus power fluctuations. Although the wind turbine drivetrain itself may have a certain damping, a wind turbine controller is typically designed to avoid excessive drivetrain oscillations [66] as they may increase the wear of mechanical components. Nevertheless, it is worth evaluating whether power fluctuations caused by drivetrain oscillations are observable in the output power of the 2.75 MW reference nacelle.

It must be noted that Leisten et al. in [43], [44] presents two different sets of eigenfrequencies for the same wind turbine which is the aforementioned 2.75 MW reference wind turbine nacelle. The first set indicated by the orange squares is the expected set of the original eigenfrequencies with the rotor assembly. Whereas, the second set indicated by red squares is a set of eigenfrequencies where the FVA nacelle operates on the system test bench at CWD. This discrepancy occurs due to the missing rotor assembly in the setup on the wind turbine system test bench. Instead, an electric motor and a load application unit are attached to the rotor hub to emulate the behavior of the missing rotor.

3.3 Flicker Caused by Power Fluctuations

Turbulence

In order to observe the behavior of the output power at the PCC, a simulation of the wind turbine model shown in Fig. 2.4 is carried out using the simulation software MATLAB/Simulink [67] in combination with PLECS [68]. For this purpose, the electrical drivetrain is modeled applying the root-mean-square (RMS) approach presented in [69]. According to this publication, the RMS approach is already sufficient to reproduce the dynamic of the power transmission from the generator to the electrical grid. Furthermore, the RMS approach is beneficial in terms of simulation time compared to the detailed electromagnetic transient (EMT) modeling approach. Therefore, the RMS approach is preferred here. The flicker severity level P_{st} is calculated using the IEC flickermeter process shown in Fig. 3.2.

As shown in Fig. 3.9, the simulation results show a correlation between the turbulence intensity I_{wind} and the flicker severity level P_{st}. The difference in the flicker severity level between the high and low turbulence at the same average wind speed can be as high as 1 which can be considered as severe. Per definition, a flicker severity level of 1 means that 50 % of the population notice flicker and find it irritating. Particularly under medium average wind speed V_{wind}, the flicker severity level reaches its maximum. This is because the wind turbine operates within the region 2 according to Fig. 2.5b where it tracks its maximum aerodynamic efficiency. Thus, the wind turbine output power follows the fluctuating wind speed leading to a high output power fluctuation. On the other hand, the flicker severity level reduces at high average wind speeds. In this situation, the wind turbine limits its output power to its nominal power whenever the wind speed exceeds the nominal wind speed.

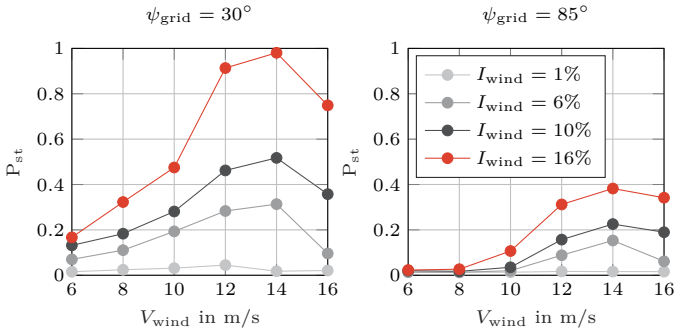

Figure 3.9: Flicker severity level of the simulated wind turbine in Fig. 2.4 under turbulent wind conditions. $S_{\text{grid}} = 3\,\text{pu}$.

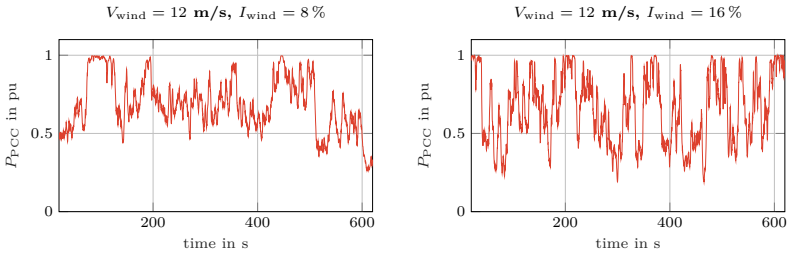

Figure 3.10: Simulated output power fluctuation of a wind turbine

When the wind turbine is operating at a more inductive grid i.e. θ_{grid} close to 90°, the flicker intensity is substantially reduced since the voltage variation is at minimum according to Fig. 3.2. Therefore, it is highly important to assess the flicker emission of wind turbines for their operation at resistive grids rather than inductive grids. Moreover, wind turbines typically have a medium voltage grid connection and the medium voltage (MV) distribution grids behave mostly resistive ($X_{\text{grid}}/R_{\text{grid}} \leq 8$) [70].

As a comparison, the output power of the 2.75 MW reference wind turbine nacelle were measured at various wind speeds and turbulence intensities. Similarly, the induced flicker is post-processed by means of simulations. Two exemplary results at $V_{\text{wind}} = 12\,\text{m/s}$ are given in Fig. 3.11 showing the output power fluctuation of the nacelle under a turbulent wind. A similar behavior on the reference nacelle is observed in the presented measurement results where the output power P_{PCC}

follows the course of the wind speed v_{wind} as long as $P_{\text{PCC}} \leq 1\,\text{pu}$. Otherwise, the reference nacelle maintains its output power at the nominal value i.e. $P_{\text{PCC}} = 1\,\text{pu}$.

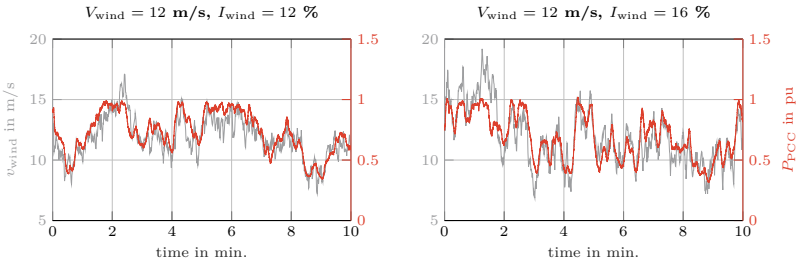

Figure 3.11: Measured output power fluctuation of the 2.75 MW reference wind turbine nacelle

Due to the low grid impedance of the electrical grid of the test bench at Center for Wind Power Drives ($S_{\text{grid}} \approx 21\,\text{pu}$), the resulting voltage fluctuation is too low to capture. Therefore, simulations were additionally carried out to obtain the flicker severity level at other grid conditions particularly at $S_{\text{grid}} = 3\,\text{pu}$ and $\theta_{\text{grid}} = 30°$, the same condition as in Fig. 3.9. For these simulations, the measured generator torque and rotational speed were taken as the input parameters and the same electrical drivetrain model was used.

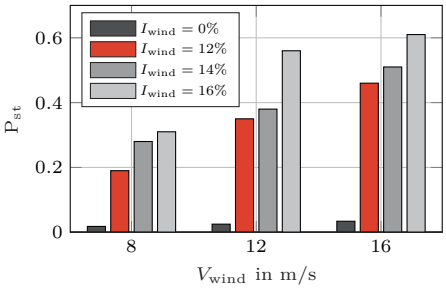

Figure 3.12: Flicker severity level of a 2.75 MW reference wind turbine nacelle

Figure 3.12 depicts the flicker severity level P_{st} of the reference nacelle at various average wind speeds V_{wind} and turbulence intensities I_{wind}. This figure shows that wind turbulence is the main contributing factor to flicker. The P_{st} without turbulence component in the wind speed (dark grey bars) is nearly zero under

all measured average wind speeds. Whereby, the P_{st} increases if the turbulence component is added to the wind speed indicated by a higher turbulence intensity. Although a similar rising trend of P_{st} versus wind speed is observed in the measurements as compared to the P_{st} trend in Fig. 3.9, the declining trend of P_{st} is still not observable until the tested average wind speed. This is because the reference nacelle reaches its nominal power at a higher wind speed as compared to the turbine model in Fig. 3.9.

Tower Shadowing Effect

Although the tower shadowing effect causes a power fluctuation on the generator side with a very low magnitude, it is still important to assess the resulting flicker severity level P_{st}. For this purpose, simulations with the same setup as in Fig. 3.7 were carried out with two conditions, with and without the tower shadowing. The results are presented in Fig. 3.13. In these simulations, the wind turbine is coupled to a grid having a short-circuit power $S_{grid} = 3\,\text{pu}$ and a grid impedance angle $\theta_{grid} = 30°$.

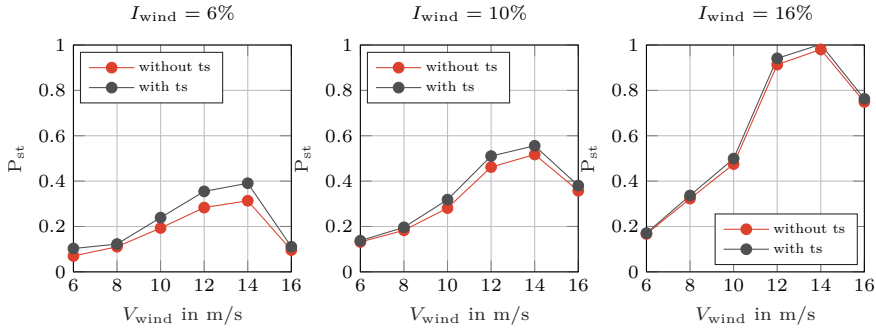

Figure 3.13: Flicker severity level P_{st} without (red) and with (grey) tower shadowing effect at various wind speeds and turbulence intensity.

From the flicker severity level in Fig. 3.13, it is revealed that the contribution from tower shadowing effect to flicker is substanstially lower as compared to contribution from the wind turbulence. Namely at high turbulence intensities, there is almost no difference in flicker severity level between the simulated conditions with and without tower shadowing effect. Nevertheless, at lower turbulence intensity, the contribution from wind turbulence to flicker reduces while the power fluctuation from tower shadowing effect remains. The difference in the simulated

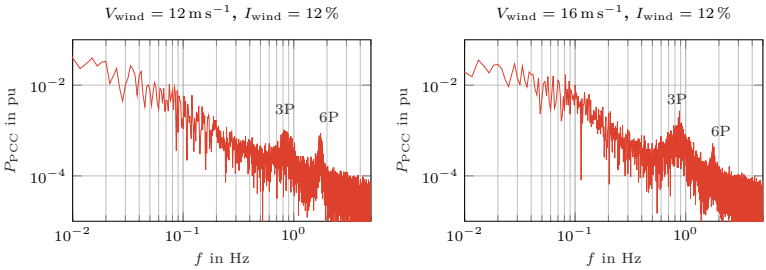

Figure 3.14: Output power of the reference nacelle in frequency domain

flicker severity level can reach around 20 % or larger than flickermeter tolerated error of 5 %. Therefore, it can be concluded that tower shadowing effect must be taken into consideration when measuring flicker on the test bench. This means that both the wind load and grid emulator systems must be able to correctly emulate the influence of the tower shadowing effect.

To observe the oscillation components in the measured output power, a fast fourier transformation (FFT) is applied to perform an analysis in frequency domain. The results for two different wind speeds are plotted in Fig. 3.14. Here, the indication of the tower shadowing effect can be observed by the frequency component in these plots marked by "3P". However, its magnitude is very small which is aligned with previous analysis. The frequency of this component also matches with the triple rotor rotation frequency in (3.2). Furthermore, another component at twice of the tower shadowing effect's frequency is observable as well. This frequency component marked by "6P"is the harmonic component of the power oscillation caused by tower shadowing effect.

From this measurement, it is not possible to quantify the contribution of tower shadowing effect to flicker severity level P_{st} because it is inherent in the real-time simulation of the rotor blades. Operation at zero turbulence intensity helps quantifying the flicker severity level caused by tower shadowing effect. As Fig. 3.12 shows, P_{st} is much lower compared to the flicker severity level at other turbulence intensities. This shows the low contribution from tower shadowing effect to the induced flicker. Relative to the P_{st} at $I_{\text{wind}} = 12\,\%$, the P_{st} at non-turbulent wind reaches 10 % or double the tolerance limit for an IEC flickermeter according to [49]. It can be concluded that tower shadowing effect is an essential part in the induced flicker by a wind turbine despite its relatively low magnitude. Therefore, when measuring flicker on a wind turbine test bench particularly with a grid emulator, tower shadowing effect shall be emulated properly and its effect on the

PCC voltage must be realized accurately.

Drivetrain Resonance

As mentioned earlier, if drivetrain eigenfrequencies are excited during the operation, flicker may be induced since the eigenfrequencies may be located at subsynchronous frequency range where flickermeter is sensitive. Nevertheless, only the power fluctuations caused by the tower shadowing effect are observable in the frequency spectrum plot of the output power in Fig. 3.14. No other oscillations can be observed in this frequency spectrum plot. The wind-turbine controller is typically constructed in such a way to minimize the excitation of the drivetrain eigenfrequencies. Thereby, power fluctuations caused by drivetrain resonance are typically unseen in the output power, thus not relevant for flicker.

3.4 Average Output Power Drift due to Turbulence

In terms of average output power, flicker can have a negative effect as well. Figure 3.15 shows the output power of the above simulated wind turbine model averaged over 10 min which is expressed by $\bar{P}_{\mathrm{pcc}}$. In the figure, the baseline power curve (light blue curve) based on the design in Fig. 2.5 is also plotted for comparison purpose. As this figure shows, the average output power of the simulated wind turbine deviates as a wind turbulence occurs. This happens particularly when the wind turbine operates in the constant power mode i.e. at high wind speeds (region 3 in Fig. 2.5). This phenomenon happens because the applied control strategy limits the output power to 1 pu when the instantaneous wind speed is higher then the nominal wind speed. On the other hand, the wind turbine does not have enough energy storage that can cover the power deficit when the instantaneous wind speed falls below its average value. Thereby, the average output power gets reduced especially at the transition between the operation region 2 and 3.

Looking at the measured average output power, a similar effect is observable in the reference nacelle. Figure 3.16 shows the average output power over 10 minutes of the reference nacelle. The grey curve represents the baseline power curve while the average output power are represented by the red dots. It can be seen that the average power deviates from its baseline at the beginning of the constant power mode region (region 3). Similar reason is behind this phenomenon where the output power is limited to 1 pu whenever the instantaneous wind speeds allow a

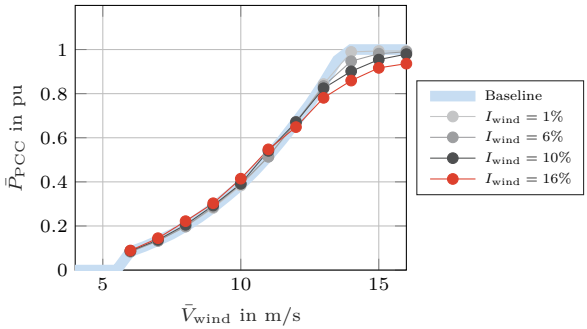

Figure 3.15: Average output power of a wind turbine $\bar{P}_{\mathrm{pcc}}$ under various turbulence intensities

higher aerodynamic power. In contrast, the output power of the nacelle follows the available aerodynamic input power when the instaneous wind speed drops to lower values since no element within the nacelle is capable to cover the power deficit. Next to flicker, this behavior of output power may present a challenge for electrical grid operators in particular when the penetration of wind turbines has reached a significant number.

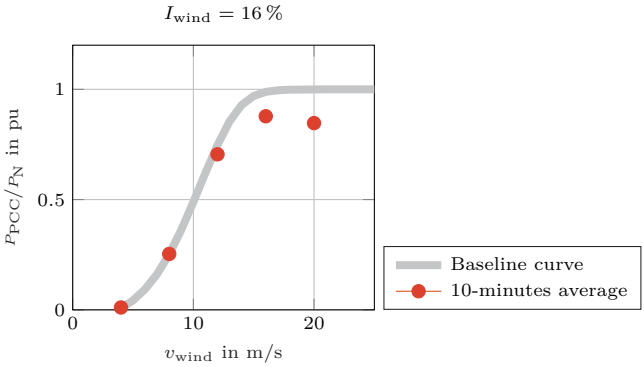

Figure 3.16: Power curve of the reference nacelle (grey) and the measured 10-minutes average power $\bar{P}_{\mathrm{pcc}}$ (red) for various V_{wind} and $I_{\mathrm{wind}} = 16\,\%$

3.5 Summary

From the analysis presented in this chapter, it can be concluded that to derive the requirements on grid emulators for flicker measurements, the dynamic of the power fluctuation due to turbulence and tower shadowing effect must be taken into account. As far as flicker severity level is concerned, wind turbulence and tower shadowing effect are the main contributing factors although the contribution from the tower shadowing effect is considerable only in case of low wind speeds and high turbulence intensities. According to the measurement in the reference nacelle, drivetrain resonances do not contribute to flicker under normal operation conditions.

4 Dynamic Behavior at the Grid Connection Point

To contribute to the grid stability, modern wind turbines must stay synchronized with the electrical grid even in the event of certain grid faults. This is further called low-voltage ride-through (LVRT) capability. Additionally, a dynamic grid support by a reactive current injection is demanded to support the grid voltage during fault events to prevent a voltage collapse.

In wind turbines employing the full-scale converter concept, the capability of wind turbines in fulfilling the LVRT requirement depends particularly on the performance of the current controller of the grid-side converter. This is not the case in wind turbines employing doubly-fed generators since the stator of the generator is directly coupled with the electrical grid. Thus, the power-electronic converter plays a significant role in the dynamic response to grid faults [32], [71]–[73]. The performance of the current controller in terms of the control stability and its response to the fast changing reference current is affected by the unknown and changing grid impedance. Depending on the fault location and grid structure, grid faults may lead to different grid impedances. Hence, different control performance is expected with varying fault scenarios.

With regards to the LVRT tests for the grid compliance verification, the questions that must be addressed are:

- What are the possible scenarios for grid faults which must be reflected in an LVRT test?
- How the grid-side converter current controller of a wind turbine responds to these scenarios?
- Is the LVRT capability and dynamic voltage support of wind turbines affected by the occurring fault scenarios?

This chapter addresses these questions by analyzing a baseline current controller given in the literatures and publications. The results will be compared with the 2.75 MW reference nacelle to verify analysis results.

When introducing and evaluating a grid emulator as an alternative test method, conducting this analysis is essential because it provides benchmarks to validate the test results. Although a test method in Fig. 1.2b has been widely used to verify the LVRT capability of wind turbines, taking only the test results from the conventional method as a benchmark [74] is not sufficient since the conventional test method may only depict a certain fault cases depending on the available inductances in the test setup.

This chapter is structured as follows. At first, the analytical modeling of a grid-side current controller is derived and the influence of the grid impedance on the control performance parameters is described. Afterwards, the grid impedance models during faults based on the literatures are presented. Finally, the performance of the current controller for different fault cases are analyzed. For the analysis in this chapter, the parameters of the grid-side converter given in Table 4.1 are used.

Table 4.1: Parameter of the baseline grid-side converter

Parameter	**Symbol**	**Value**
Nominal power	$S_{\mathrm{WT,N}}$	5 MVA
Nominal voltage	$V_{\mathrm{WT,N}}$	690 V
Fundamental frequency	$f_{\mathrm{grid,1}}$	50 Hz
DC-link voltage	V_{dc}	1.07 kV
Filter inductor	L_{f}	24.97 µH
Filter capacitor	C_{f}	2.8 mF
Damping resistance	R_{f}	5.8 mΩ
Transformer leakage inductance	L_{σ}	22.73 µH
Switching frequency	f_{sw}	3.2 kHz
Sampling frequency	f_{samp}	6.4 kHz

4.1 Current Controller Modeling

The control task for the grid-side converter's current is typically performed on an arbitrary reference frame that synchronously rotates with the grid voltage [33], [36], [37]. In a synchronous reference frame, the active and reactive current control can be performed independently. Moreover, controlling alternating-current (ac) quantities in a synchronous reference frame enables the application of proportional-integral (PI) regulators. The overview of the grid-side current controller architecture in a synchronous reference frame is shown in Fig. 4.1.

To form a closed-loop current control, the three-phase grid-side converter cur-

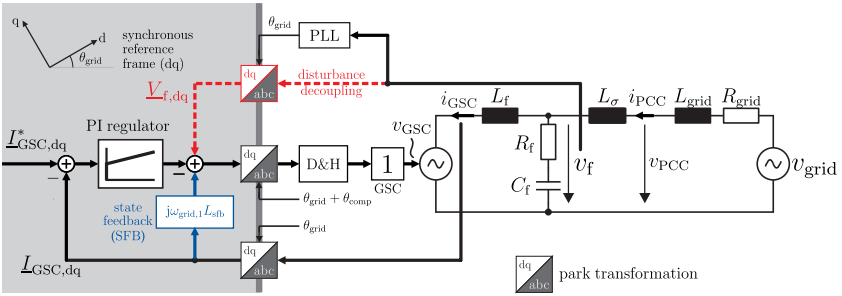

Figure 4.1: Typical control architecture for the grid-side converter current i_{GSC}

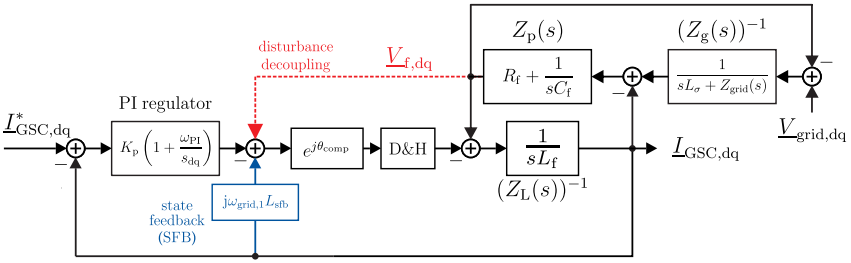

Figure 4.2: Current control model in the s-domain

rent i_{GSC} needs to be measured as a control feedback and transformed onto an arbitrary rotating reference frame using the park transformation [39]. For the park transformation, a phase-locked loop (PLL) [75], [76] is needed to capture the angle of the grid voltage θ_{grid}. Thus, the reference frame will be synchronized with the grid voltage.

It is also a common practice that the voltage v_{f} is used instead of the PCC voltage v_{PCC} to construct the reference frame due to practical reasons. The error between the measured grid-side current to its reference $\underline{I}^{*}_{\mathrm{GSC,dq}}$ is then regulated by a PI regulator. A state feedback (SFB) colored in blue is added to the PI regulator's output to decouple the cross-coupling effect between the d-axis and q-axis components of the plant as briefly described in [33], [36], [37], [77]–[79]. Principally, the SFB gain is the reactance of the inductance L_{SFB} at the angular frequency of the reference frame ω_{dq} which equals the grid voltage $\omega_{\mathrm{grid},1}$. If the disturbance decoupling is not used, $L_{\mathrm{SFB}} = L_{\mathrm{f}} + L_{\sigma}$. Hence,

$$Z_{\mathrm{SFB}} = \mathrm{j} \cdot \omega_{\mathrm{grid},1} \cdot \underbrace{(L_{\mathrm{f}} + L_{\sigma})}_{L_{\mathrm{SFB}}}. \tag{4.1}$$

Finally, the output of the control process is reversed transformed to the three-phase system before it is amplified by the grid-side converter. In this thesis, an ideal power-electronic converter is assumed. Thus, it is represented by a unity gain.

Since today's converter controllers are realized digitally, a delay and hold block (D&H) must be added to account the internal control delay as well as the zero-order hold as a result of the digital control implementation. To compensate the phase shift caused by this block, θ_{comp} is added to grid voltage angle θ_{grid} when transforming the control output back to the three phase system.

To analyze the control performance under varying grid impedances, the control architecture in Fig. 4.1 is modeled in the s-domain. The resulting control loop is illustrated in Fig. 4.2. It must be noted that the Laplace operator s of the PI regulator differs to that of the plant. Therefore, a subscript dq is given to the one of the PI regulator to distinguish. This is necessary because the PI regulator is performed in the synchronous reference frame rotating with an angular frequency ω_{dq}. If a signal with an angular frequency ω_{s} appears in the plant and the reference frame is synchronized with the grid voltage i.e. $\omega_{\mathrm{dq}} = \omega_{\mathrm{grid},1}$, this signal is seen by the controller as a signal with a frequency of $\omega_{\mathrm{s,dq}} = \omega_{\mathrm{s}} - \omega_{\mathrm{dq}}$. Thus the relationship between the two Laplace operators can be expressed by [77], [78]:

$$s_{\mathrm{dq}} = s - \mathrm{j} \cdot \omega_{\mathrm{dq}} \tag{4.2}$$

In the following, the performance of such a control architecture considering the system parameters in Table 4.1 is assessed under various grid impedances $\underline{Z}_{\mathrm{grid}} = R_{\mathrm{grid}} + \mathrm{j} \cdot X_{\mathrm{grid}}$. For this purpose, the open-loop transfer function of the current controller needs to be derived with the help of a modified plant transfer function that summarizes all blocks in Fig. 4.2 except the PI regulator. For this thesis, the modified plant transfer function is expressed as a function of the Laplace operator in the synchronous reference frame s_{dq}. The resulting modified plant transfer function is given by the following equation:

$$G_{\mathrm{pl}}(s_{\mathrm{dq}}) = \frac{G_{\mathrm{D\&H}}(s_{\mathrm{dq}}) \cdot e^{\mathrm{j}\theta_{\mathrm{comp}}} \cdot Y_{\mathrm{GSC}}(s_{\mathrm{dq}})}{1 - G_{\mathrm{D\&H}}(s_{\mathrm{dq}}) \cdot e^{\mathrm{j}\theta_{\mathrm{comp}}} \cdot Y_{\mathrm{GSC}}(s_{\mathrm{dq}}) \cdot Z_{\mathrm{SFB}}} \tag{4.3}$$

where

$$Y_{\mathrm{GSC}}(s_{\mathrm{dq}}) = \left[Z_{\mathrm{L}}(s_{\mathrm{dq}}) + \frac{Z_{\mathrm{g}}(s_{\mathrm{dq}}) \cdot Z_{\mathrm{p}}(s_{\mathrm{dq}})}{Z_{\mathrm{g}}(s_{\mathrm{dq}}) + Z_{\mathrm{p}}(s_{\mathrm{dq}})} \right]^{-1} \tag{4.4}$$

and

$$G_{\mathrm{D\&H}}(s) = e^{-\mathrm{j}(s \cdot T_{\mathrm{DH}})} \cdot \frac{1 - e^{-\mathrm{j}(s \cdot T_{\mathrm{DH}})}}{s \cdot T_{\mathrm{DH}}} \tag{4.5}$$

It has to be noted that the disturbance decoupling path marked in red in Fig. 4.1 and Fig. 4.2 is not yet considered in this stage. Taking the plant transfer function in (4.3) and the PI regulator into account, the open-loop transfer function of the current controller becomes:

$$G_{\mathrm{ol}}(s_{\mathrm{dq}}) = K_{\mathrm{p}} \left(1 + \frac{\omega_{\mathrm{PI}}}{s_{\mathrm{dq}}} \right) \cdot G_{\mathrm{pl}}(s_{\mathrm{dq}}) \tag{4.6}$$

K_{p} and ω_{PI} in the above equation are the gain and the corner frequency of the PI regulator in Ω and $^{\mathrm{rad}}/_{\mathrm{s}}$, respectively.

Figure 4.3 shows the magnitude and phase plots of the plant and open-loop transfer function at a low grid short-circuit power $S_{\mathrm{grid}} = 3\,\mathrm{pu}$. Additionally, the plant without the state feedback (SFB) obtained by setting $L_{\mathrm{SFB}} = 0\,\mathrm{H}$ in (4.3) is also given in this figure for a comparison purpose.

Firstly, the transfer function without the disturbance decoupling is discussed. It can be observed from Fig. 4.3 that the shape of the open-loop transfer function is not symmetric between the positive and negative frequency sides [(i)]. As a result, the positive phase margin PM+ and negative phase margin PM- become unbalanced. Similarly, the positive bandwidth frequency $f_{\mathrm{bw+}}$ and negative bandwidth frequency $f_{\mathrm{bw-}}$ are unbalanced as well . The reason for the asymmetry of the open-loop transfer function can be explained by looking at the plant transfer function. Due to the inductances, the plant is supposed to have a pole at $f = 0\,\mathrm{Hz}$. Without the state feedback, this pole is however shifted to $f = -f_{\mathrm{grid,1}}$

[(i)] A vector in a synchronous reference frame is considered to have a negative frequency if it rotates with the opposite direction with the rotation of the reference frame

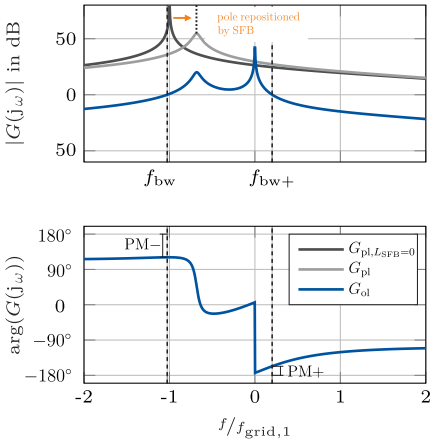

Figure 4.3: Plant and open-loop transfer function of the grid-side converter current controller $G_{\mathrm{ol}}(s_{\mathrm{dq}})$. $S_{\mathrm{grid}} = 3\,\mathrm{pu}$ and $\theta_{\mathrm{grid}} = 90°$

in the synchronous reference frame (refer to (4.2)). Hence, the open-loop transfer function becomes asymmetric between the positive and negative sides.

With the help of the state feedback (SFB), the shift of the plant's pole is supposed to be compensated. However, a perfect compensation requires an information on the unknown grid inductance L_{grid} i.e. $L_{\mathrm{SFB}} = L_{\mathrm{f}} + L_{\sigma} + L_{\mathrm{grid}}$. Thus, the SFB is only capable of repositioning the plant's pole towards 0 Hz in Fig. 4.3 in case of a low grid short circuit power. In other words, the control behavior is sensitive to variations in the grid impedance.

Ultimately, the current controller performance is dictated by the lowest phase margin and the bandwidth frequency. In this example, it is determined by the PM+ and $f_{\mathrm{bw+}}$. This means that the designer of such a current controller can still get an accurate information on the performance of the current controller if the negative side is not included in the figure as long as the resonance of the LCL filter is sufficiently dampened either passively or actively.

The simplest method to minimize the control sensitivity against the grid impedance is by decoupling the influence of the grid voltage via a measurement as shown by the red path in Fig. 4.1. This way is called voltage disturbance decoupling (VDD). When considering the VDD, the modified plant transfer function becomes:

$$G_{\mathrm{pl,VDD}}(s_{\mathrm{dq}}) = \frac{G_{\mathrm{pl}}(s_{\mathrm{dq}}) \cdot (Z_{\mathrm{g}}(s_{\mathrm{dq}}) + Z_{\mathrm{p}}(s_{\mathrm{dq}}))}{Z_{\mathrm{g}}(s_{\mathrm{dq}}) + Z_{\mathrm{p}}(s_{\mathrm{dq}}) + G_{\mathrm{pl}}(s_{\mathrm{dq}}) \cdot Z_{\mathrm{g}}(s_{\mathrm{dq}}) \cdot Z_{\mathrm{p}}(s_{\mathrm{dq}})} \tag{4.7}$$

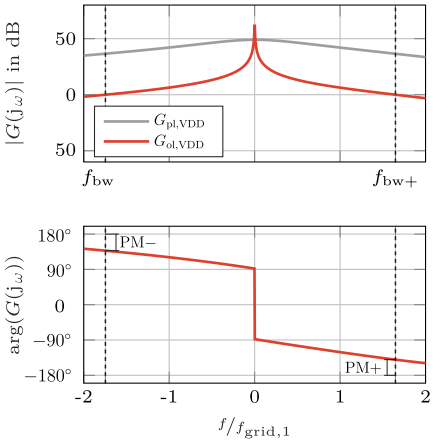

Figure 4.4: Plant and open-loop transfer function of the grid-side converter current controller $G_{\mathrm{ol}}(s_{\mathrm{dq}})$ with voltage disturbance decoupling. $S_{\mathrm{grid}} = 3\,\mathrm{pu}$ and $\theta_{\mathrm{grid}} = 90°$

In Fig. 4.4, the modified plant transfer function applying the voltage disturbance decoupling $G_{\mathrm{pl,VDD}}(s_{\mathrm{dq}})$ and the resulting open-loop transfer function are plotted. The open-loop transfer function is obtained by substituting $G_{\mathrm{pl}}(s_{\mathrm{dq}})$ in (4.6) with $G_{\mathrm{pl,vdd}}(s_{\mathrm{dq}})$ in (4.7). In this plot, the improvement as a result of voltage disturbance decoupling is observable. The pole of the modified plant is now located at 0 Hz allowing the open-loop transfer function to be more symmetrical. Thereby, the phase margin and the bandwidth frequency are also similar between both sides. When looking at the negative side, although the phase margin PM- is reduced, the bandwidth frequency $f_{\mathrm{bw-}}$ is significantly improved. On the positive side, both phase margin PM+ and bandwidth frequency $f_{\mathrm{bw+}}$ are improved significantly in particular the PM+ allowing the system to be more stable. Therefore, the ultimate control performance is improved. In contrast to the previous control setup, here the state feedback only accounts the filter inductance that is more predictable, i.e. $L_{\mathrm{SFB}} = L_{\mathrm{f}}$.

Analytical Model Validation via Circuit Simulations

In order to validate the analytical model of the current controller, simulations were conducted with a circuit simulator PLECS [68]. The description of the simulation model of the grid-side converter including its current controller can be found in Appendix A.2. In this simulation, the dc-link voltage is set to be constant. In the first validation, a rotating vector in a synchronous reference frame with a varying frequency is set as the current reference $\underline{I}^{*}_{\mathrm{GSC,dq}}$. The magnitude of the actual grid-side converter current $|\underline{I}_{\mathrm{GSC,dq}}|$ is measured and plotted in Fig. 4.5 which is indicated by the diamond shapes. For comparison, the closed-loop transfer functions of the current controller without and with disturbance decoupling $G_{\mathrm{cl}}(s_{\mathrm{dq}})$ and $G_{\mathrm{cl,VDD}}(s_{\mathrm{dq}})$ respectively are also plotted in this figure.

$$\begin{aligned} G_{\mathrm{cl}}(s_{\mathrm{dq}}) &= \frac{G_{\mathrm{ol}}(s_{\mathrm{dq}})}{1 + G_{\mathrm{ol}}(s_{\mathrm{dq}})} \\ G_{\mathrm{cl,VDD}}(s_{\mathrm{dq}}) &= \frac{G_{\mathrm{ol,VDD}}(s_{\mathrm{dq}})}{1 + G_{\mathrm{ol,VDD}}(s_{\mathrm{dq}})} \end{aligned} \tag{4.8}$$

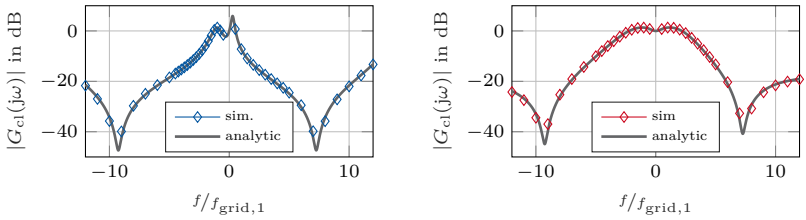

(a) Without disturbance decoupling

(b) With disturbance decoupling

Figure 4.5: Analytical model validation via circuit simulations in frequency domain

It can be seen in Fig. 4.5 that the aforementioned analytical model of the current controller matches perfectly with the results from circuit simulations. This is valid not only for the case without the disturbance decoupling but also with the disturbance decoupling. Hence, the above described analytical model can be used to conduct further analysis.

Sensitivity Analysis

As mentioned earlier, the control performance without disturbance decoupling is sensitive to variations in the grid impedance Z_{grid} or short-circuit power S_{grid}. To verify this statement, the phase margin PM and bandwidth frequency f_{bw} are plotted in Fig. 4.6a for various grid short-circuit power. As expected, the phase margin and control bandwidth are strongly affected by the varying S_{grid} thanks to shift of the plant's pole which is not fully compensated by the state feedback. When plotting the performance parameters of the control setup with the voltage disturbance decoupling in Fig. 4.6b, the performance improvement is visible. The phase margin and the control bandwidth become more balanced throughout the simulated grid short-circuit power. Moreover, with a higher phase margin and control bandwidth, a more stable and quicker response can be achieved as displayed by the step response simulation in Fig. 4.7.

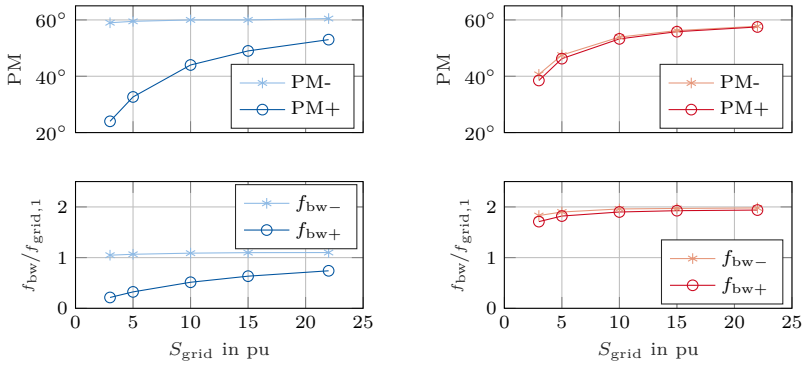

(a) Without disturbance decoupling

(b) With disturbance decoupling

Figure 4.6: Comparison of control performance parameters under various grid short-circuit power S_{grid}

From this discussion, it becomes clear that voltage disturbance decoupling is a very simple method to strive a significant improvement in the control performance. Therefore, it is expected that wind turbine converters are equipped with a voltage disturbance decoupling to gain a good control performance required in particular during very demanding situations such as grid faults. This control setup will be taken as a benchmark setup for further discussions in this thesis. As Fig. 4.6b shows, the controller still shows a sensitivity against the varying grid impedance despite applying the voltage disturbance decoupling. This is at-

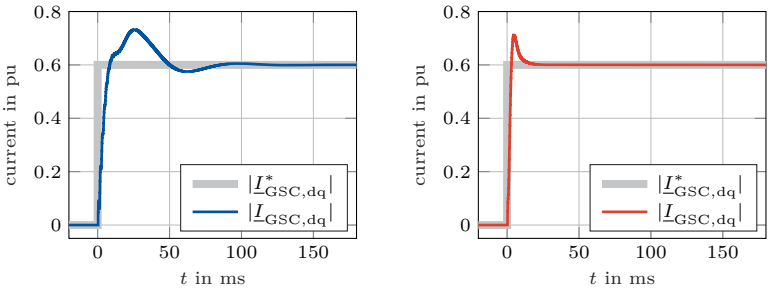

(a) Without disturbance decoupling

(b) With disturbance decoupling

Figure 4.7: Step response simulation of the current controller at $S_{\mathrm{grid}} = 3\,\mathrm{pu}$

tributed to the control delay represented by the D&H block in Fig. 4.2 that adds a phase delay to the disturbance decoupling path. Therefore, it is also expected that converters applying lower switching frequencies will show a higher sensitivity to grid impedance variations.

Lastly, it is worth looking at the changes in the controller performance due to grid impedance variations at different PI regulator parameters. Quite often that the PI regulator is tuned for a particular grid situation. Once the grid impedance changes as a result of grid restructuring or grid faults, the controller may not perform as expected anymore. Therefore, the phase margin PM and the bandwidth frequency f_{bw} under different PI regulator parameters are plotted in Fig. 4.8. In Fig. 4.8a, the PI regulator's gain K_{p} is varied with a factor of 1.5 (blue diamonds) and 2 (black squares) of the reference gain $K_{\mathrm{p,ref}}$ used in the previous discussions. In Fig. 4.8b the PI regulator's corner frequency w_{PI} is increased (black squares) and lowered (blue diamonds) with a factor of 2 of the reference corner frequency $w_{\mathrm{PI,ref}}$ used in the previous discussions. The coloring from dark to light represents the variations in the grid short-circuit power from 3 pu to 22 pu.

From Fig. 4.8a, increasing the PI regulator's gain apparently will enhance the control bandwidth thus a shorter settling time. However, the control performance in terms of phase margin and bandwidth frequency deteriorates more severely following the reduction in the grid short circuit power S_{grid}. Consequently, if the current controller is tested and tuned at an electrical grid having a very low grid short-circuit power, the control tends to be less stable and have a slower response when it is operating at an electrical grid with a higher short-circuit power. Noted that the modification in ω_{PI} basically reduces the stability without

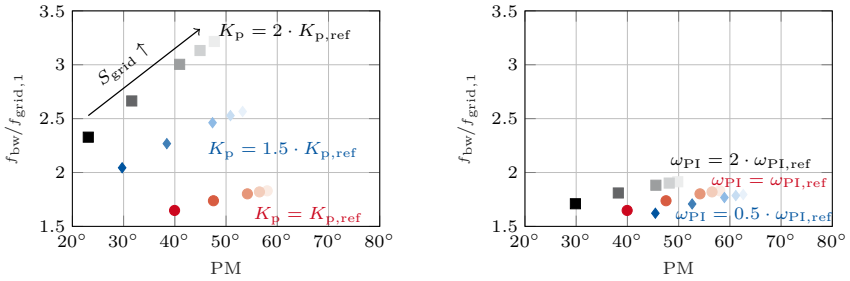

(a) Gain K_p (b) Corner frequency ω_{PI}

Figure 4.8: Sensitivity analysis of PI regulator parameters on the control performance for different S_{grid}

gaining benefits in terms of bandwidth. Therefore, it is expected that the tuning for grid-side current controller is mostly done by K_p.

4.2 Grid-Fault Scenarios and Models

This thesis emphasizes two particular short-circuit fault scenarios that lead to a substantial difference in terms of the small-signal grid impedance at the PCC of a wind turbine. These scenarios are illustrated in Fig. 4.9.

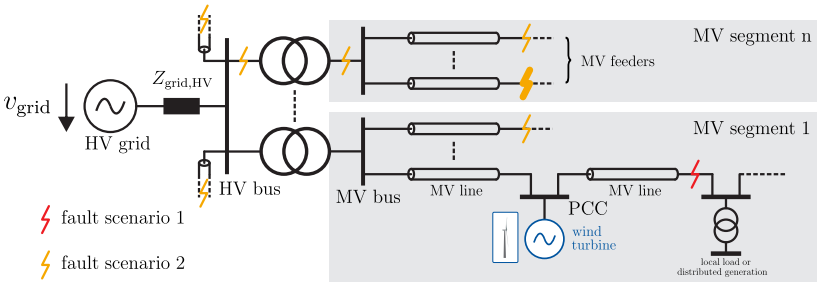

Figure 4.9: Short-circuit fault scenarios

In this illustration, multiple medium-voltage (MV) grid segments are fed by a high-voltage (HV) grid via step-down transformer substations. Each MV segment

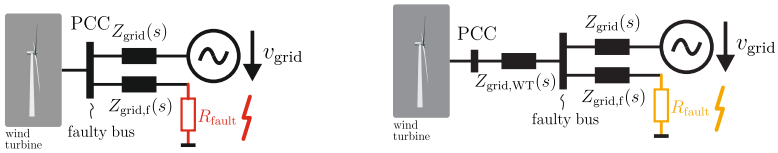

(a) Scenario 1 (b) Scenario 2

Figure 4.10: Grid fault scenarios and the simplified grid impedance model depending on the fault location

consists of one or multiple MV feeders to which loads or distributed generations like wind turbines are connected. For a study of a single wind turbine, it is assumed that a wind turbine is connected to one of the MV feeders as illustrated in Fig. 4.9 since multi-megawatt wind turbines typically have a medium-voltage grid connection. Noted that an MV segment may also be interpreted as a wind farm or a wind farm cluster supplying a high-voltage grid via a step-up transformer.

Two notable short-circuit fault scenarios that present a substantial difference in terms of the small-signal grid impedance at the wind turbine's PCC are marked in red and orange in Fig. 4.9. In the scenario 1 marked in red, a fault occurs in the same MV feeder, to which the wind turbine is located. For instance, a short-circuit occurs at an MV line in the downstream section of the mv feeder as indicated by red mark in Fig. 4.9. This scenario is commonly taken to conduct studies of a single wind turbine.

From the perspective of the wind turbine, the grid impedance for the fault scenario 1 can be simplified as depicted in Fig. 4.10a. The impedance Z_{grid} is the equivalent grid impedance at the wind turbine's PCC while the impedance $Z_{\text{grid,f}}$ represents the impedance of the faulty line from PCC to the fault location. When the wind turbine is inactive (no-load condition), the voltage experienced by the wind turbine at the wind turbine's PCC is expressed by:

$$\underline{V}_{\text{PCC,f}} = \underline{V}_{\text{grid}} \cdot \frac{(Z_{\text{grid,f}} + R_{\text{fault}})}{Z_{\text{grid,f}} + R_{\text{fault}} + Z_{\text{grid}}} \tag{4.9}$$

The magnitude of $\underline{V}_{\text{PCC,f}}$ is further called residual voltage in this thesis. R_{fault} in (4.9) denotes the resistance of the fault at the fault location. Considering a bolted fault i.e. $R_{\text{fault}} = 0\,\Omega$, the magnitude of the PCC voltage gets lower with

a lower $Z_{\mathrm{grid,f}}$. In other words, the fault location is closer to the PCC bus of the wind turbine. In this scenario, the equivalent small-signal impedance of the grid can be expressed by the following equation:

$$Z_{\mathrm{PCC,f}}(s) = \frac{(Z_{\mathrm{grid,f}}(s) + R_{\mathrm{fault}}) \cdot Z_{\mathrm{grid}}(s)}{Z_{\mathrm{grid,f}}(s) + R_{\mathrm{fault}} + Z_{\mathrm{grid}}(s)} \tag{4.10}$$

The scenario 2 marked in orange represents a short-circuit fault occurring in the neighboring feeder, in other another MV grid segment or in the high voltage (HV) network. The simplified grid model for this fault scenario is depicted in Fig. 4.10b. In contrast to the scenario 1, an impedance $Z_{\mathrm{grid,WT}}$ exists between the wind turbine's PCC and the bus, to which the faulty feeder or grid segment is connected depending on the fault location. This bus is named faulty bus. In case of wind farms, the impedance $Z_{\mathrm{grid,WT}}$ can be acquired by applying an equivalencing method proposed by Muljadi, et al. in [80]. Hence, the small-signal impedance of the grid can be written as follows:

$$Z_{\mathrm{PCC,f}}(s) = Z_{\mathrm{grid,WT}}(s) + \frac{(Z_{\mathrm{grid,f}}(s) + R_{\mathrm{fault}}) \cdot Z_{\mathrm{grid}}(s)}{Z_{\mathrm{grid,f}}(s) + R_{\mathrm{fault}} + Z_{\mathrm{grid}}(s)} \tag{4.11}$$

Similar to the fault scenario 1, the impedance $Z_{\mathrm{grid,f}}$ in fault scenario 2 represents the impedance from the short-circuit fault location to the common bus between the faulty line or grid segment and the wind turbine. For the case indicated by the bold orange mark in Fig. 4.9, the impedance $Z_{\mathrm{grid,f}}$ covers the impedance from the fault location in the faulty feeder to the HV bus. Meanwhile, the impedance $Z_{\mathrm{grid,WT}}$ covers the equivalent impedance from the wind turbine's PCC to the HV bus. Under no-load condition, the voltage experienced by the wind turbine at its PCC also follows (4.9). Due to the existence of the impedance $Z_{\mathrm{grid,WT}}$ in the event of a short-circuit fault, wind turbine may behave differently in fault scenario 2 as compared to the fault scenario 1. This issue will be elaborated in detail in the following section.

Table 4.2: Simulation parameters for the fault scenario 1

Parameter	Variable	Value
Grid impedance (source-faulty bus)	Z_{grid}	3 pu
Grid impedance angle	ψ_{grid}	84°
Grid impedance (source-faulty pcc)	$Z_{\text{grid,WT}}$	0 pu
Residual voltage	$\lvert\underline{V}_{\text{PCC,f}}\rvert$	0.05 pu
Fault resistance	R_{fault}	0 pu

4.3 Behavior of the Current Controller during Grid Faults

4.3.1 Current Controller Performance

To observe the behavior of the current controller when a wind turbine encounters a grid fault, circuit simulations are carried out using the above mentioned grid-side converter model. As an example for an analysis scenario, a symmetrical fault is considered that results in a residual voltage at PCC of 0.05 pu in no-load condition. Prior to the fault occurrence, the grid-side converter is in a standby mode. It means that the grid-side converter does not deliver active and reactive power but it remains synchronized with the electrical grid. When a grid fault occurs, the grid-side converter delivers a reactive current of 1 pu to the electrical grid to provide dynamic grid support. This is realized via its q-axis current $I_{\text{GSC,q}}$. This simulation scenario is selected in order to exclude the active current from the analysis since it will lead to other phenomenon describe in the next section.

Firstly, the scenario 1 in Fig. 4.10a is analyzed. The simulation parameters for this scenario are summarized in Table 4.2. For the grid short-circuit power, the lowest value in the FGW technical guidelines for LVRT tests [23] is considered in the simulation. The impedance $Z_{\text{grid,f}}$ is therefore selected based on the simulated residual voltage. The outcome of the simulations are plotted in Fig. 4.11.

It can be seen that the grid-side converter does not immediately set its q-axis current $I_{\text{GSC,q}}$ at the fault occurrence $t = 0\,\text{ms}$. Before the grid fault mode is initiated, it firstly observes if the voltage drop is caused by a grid fault or by other matters e.g. an abrupt change of a reference current. During this period, the $I_{\text{GSC,q}}$ rises because the PCC voltage suddenly gets reduced due to the fault. The current controller acts by adapting the converter voltage to return the $I_{\text{GSC,q}}$ to the reference. After the controller switches to the grid fault operation mode, the $I_{\text{GSC,q}}$ is raised immediately to provide a grid support.

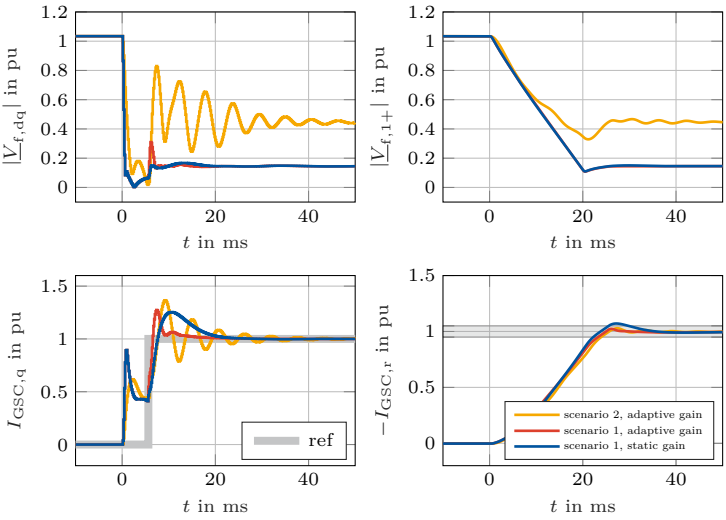

Figure 4.11: Behavior of current controller under different scenarios of a bolted grid fault ($R_{\text{fault}} = 0$). $f_{\text{samp}} = 2 \cdot f_{\text{sw}}$

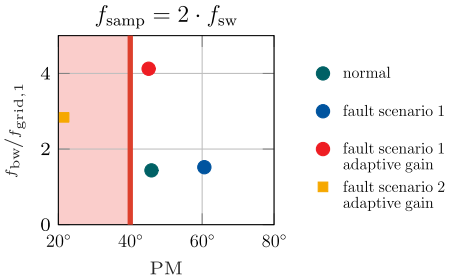

Figure 4.12: Phase margin (PM) and bandwidth f_{bw} resulted from bolted grid faults for $f_{\text{samp}} = 2 \cdot f_{\text{sw}}$

In other simulations in Fig. 4.11 (red and orange curves), the PI regulator gain is also adapted by a factor of 3.3 during the fault operation mode. As shown by the red curves, when the adaptive gain method is applied, the current controller still remains stable and the $I_{\text{GSC,q}}$ reaches its reference faster if the wind turbine encounters the fault scenario 1. However, this method increases the risk of a control instability when the wind turbine encounters the fault scenario 2 as shown

by the orange curves. This phenomenon is explained in the following.

To support the following discussion, the phase margin and the bandwidth of the current controller when encountering a grid fault is plotted in Fig. 4.12. This plot is obtained using the current controller model described in Section 4.1 and by substituting the impedance $Z_{\mathrm{grid}}(s)$ in Fig. 4.2 with (4.11). The parameters of the PI regulator are tuned for normal operation indicated by the green dot. When the wind turbine encounters the grid fault scenario 1, the controller phase margin increases (blue dot) as a result of the small-signal grid impedance gets lower. The lower is the residual voltage, the lower is the line impedance to the fault point (refer to (4.10)). Thus, the equivalent small-signal impedance of the grid becomes lower accordingly. A similar effect can also be observed in the normal operation when the grid short-circuit capacity is increased (refer to Fig. 4.8).

Due to the higher phase margin, theoretically the PI regulator gain can be increased to elevate the control bandwidth without destabilizing the current controller. If such an adaptive method is implemented, the control performance point shifts to the location indicated by the red circle in Fig. 4.12. In this example, the gain of the PI controller is increased by a factor of 3.3 such that the phase margin returns to that in normal operation. As a result, the bandwidth rises with a factor of around two. Therefore, the $I_{\mathrm{GSC,q}}$ settles faster to its reference when the gain of the PI regulator is adapted while the system remains stable This is a significant improvement particularly when considering the short time frame of grid faults and the demand on the dynamic grid voltage support via a reactive current supply.

The adaptive gain method becomes more attractive especially for converters with a low switching and sampling frequency. Therefore, a second setup of a grid-side converter is introduced here in order to observe how much improvement such a method can offer in terms of control response during a grid fault. This setup performs the sampling for its control process at the same rate as the switching frequency ($f_{\mathrm{samp}} = f_{\mathrm{sw}}$). The same filter setup as in Table 4.1 is considered except the sampling frequency and the damping resistance. Different with Table 4.1, the damping resistance R_{f} must be doubled because the active damping effect provided by the voltage disturbance decoupling deteriorates with a lower sampling frequency. Furthermore, the PI regulator's corner frequency ω_{PI} is also halved of the one of the previous setup. The outcomes of the simulation with this setup is displayed in Fig. 4.13. In Fig. 4.14, the phase margin and the bandwidth of the current controller at different situations are plotted.

Similar to the previous control setup, the phase margin with a slower sampling rate increases when a similar grid fault as in Table 4.2 occurs. When the adaptive

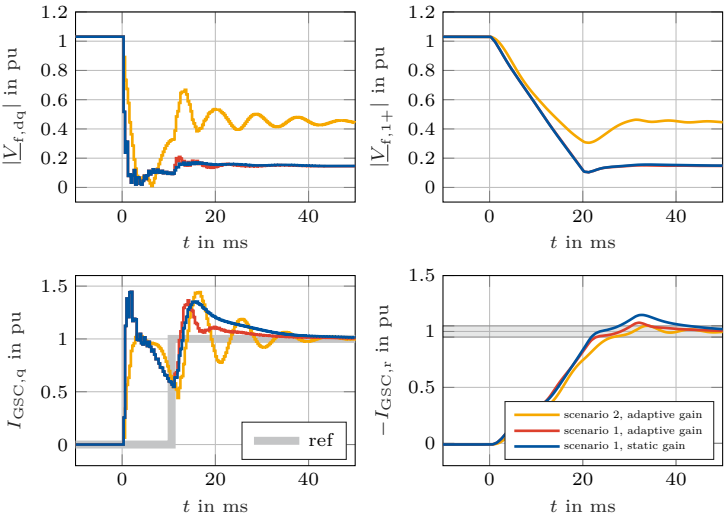

Figure 4.13: Behavior of current controller under different scenarios of a bolted grid fault ($R_{\text{fault}} = 0$). $f_{\text{samp}} = f_{\text{sw}}$

gain is implemented with a gain amplification factor of 2, a bandwidth improvement is achievable even though not as good as the previous setup due to the limitation caused by the internal control delay (refer to Fig. 4.14). This improvement is also observable in time domain as shown in Fig. 4.13. When implementing the adaptive gain (red curves), the q-axis current settles much quicker to its reference as compared to the static PI regulator gain (blue curve).

According to grid codes and technical guidelines, the positive sequence reactive current $I_{\text{GSC,r}}$ shall be evaluated to benchmark a wind turbine with regards to the LVRT capability. Therefore, the $I_{\text{GSC,r}}$ is also given alongside the q-axis current in Fig. 4.11 and Fig. 4.13. In addition, the plot of the positive sequence voltage $\underline{V}_{\text{f,1+}}$ is also plotted in these figures for the sake of completeness. Both $I_{\text{GSC,r}}$ and $\underline{V}_{\text{f,1+}}$ are obtained using the equations in Appendix A.3 [24]. The settling time of the $I_{\text{GSC,r}}$ is counted from the occurrence instance of a grid fault until $I_{\text{GSC,r}}$ enters the tolerance band (grey area) for the last time. For easy readings, the settling time of each grid-side converter setup is listed in Table 4.3 considering a tolerance band of $I^*_{\text{GSC,r}} \pm 0.05\,\text{pu}$ where $I^*_{\text{GSC,r}}$ denotes the target positive sequence reactive current. From this table, it can be seen that adapting the PI gain enables a shorter settling time. In both cases, an improvement of

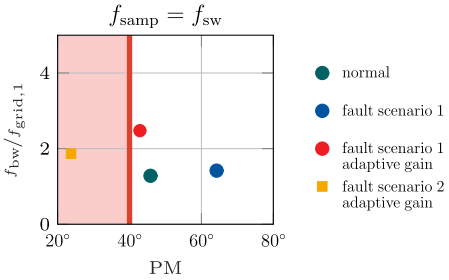

Figure 4.14: Phase margin (PW) and bandwidth f_{bw} resulted from bolted grid faults for $f_{\mathrm{samp}} = \cdot f_{\mathrm{sw}}$

about 20 % is reached with the help of adaptive PI gain. Thanks to the simple implementation, it is also possible that wind turbines are equipped with such a feature to fulfill grid codes.

Table 4.3: Settling time of the positive sequence reactive current under the fault scenario 1

	$f_{\mathrm{samp}} = 2 \cdot f_{\mathrm{sw}}$	$f_{\mathrm{samp}} = f_{\mathrm{sw}}$
Static PI gain	29.8 ms	42.7 ms
Adaptive PI gain	23.2 ms	34.2 ms
Difference	6.6 ms	8.5 ms

As mentioned earlier, the fault scenario 1 is widely used to evaluate single turbines. However, the fault scenario 2 is inevitable. In scenario 2, the adaptive gain method is no longer effective as revealed by the orange q-axis current waveforms in Fig. 4.11 and Fig. 4.13. The q-axis current shows a large oscillation under the fault scenario 2 indicating a low phase margin. When plotting the phase margin as well as the bandwidth under this operation condition into Fig. 4.12 and Fig. 4.14, one can observe that the open-loop phase margin under fault scenario 2 is shifted towards the red zone. The red zone is defined as an undesired area since the risk of instability becomes high. For the simulated example, an extreme case is considered where the $Z_{\mathrm{grid,WT}}$ accounts for 90 % of the total grid impedance at the wind turbine's PCC under normal operation. When looking at the waveforms of the positive sequence reactive current $I_{\mathrm{GSC,r}}$, the risk of control instability is not observable. This is because of the applied integration over the fundamental period in its calculation process. Therefore, it is highly important to investigate the instantaneous current rather than the positive sequence current to benchmark the LVRT capability of a wind turbine. More importantly, it is highly

recommended to consider the fault scenario 2 in addition to the fault scenario 1 that has been considered so far.

4.3.2 Loss of Synchronization

Another aspect that determines the system stability in an event of grid faults is the active or d-axis current component $I_{\mathrm{GSC,d}}$ delivered by a wind turbine. Particularly in fault scenarios that results in a very low residual voltage, the $I_{\mathrm{GSC,d}}$ of a wind turbine must be limited [81]. Otherwise, the PLL is not able to synchronize with the grid voltage [82] which leads to a system instability. Within this subsection, this phenomenon will be explained and the maximum d-axis current $I_{\mathrm{GSC,d,max}}$ will be derived for different grid impedances during a fault. For the discussion within this section, the wind turbine is considered to be operating at its nominal power ($I_{\mathrm{GSC,d}} = 1\,\mathrm{pu}$) and the grid operator does not demand any reactive current support during grid faults. Thereby, the influence of the reactive current is excluded.

Taking the fault scenario 2 into consideration and applying the superposition theorem, the voltage $\underline{V}_{\mathrm{f}}$ (refer to Fig. 4.1) at the fundamental frequency can be written as follows

$$\underline{V}_{\mathrm{f}} = \underline{V}_{\mathrm{PCC,f}} - \underline{I}_{\mathrm{GSC}} \cdot Z_{\mathrm{t}} \tag{4.12}$$

where Z_{t} is called transmission impedance and described as follows

$$Z_{\mathrm{t}} = \mathrm{j}X_{\sigma} + Z_{\mathrm{grid,WT}} + \frac{Z_{\mathrm{grid,f}} \cdot Z_{\mathrm{grid}}}{Z_{\mathrm{grid,f}} + Z_{\mathrm{grid}}} \tag{4.13}$$

Noted that the voltage $V_{\mathrm{PCC,f}}$ in (4.12) is the voltage at PCC when a grid fault occurs and the wind turbine is inactive which is described by (4.9). Furthermore, the current into the parallel filter components C_{f} and R_{f} is assumed to be negligibly small in the event of a grid fault with a low residual voltage, thus $I_{\mathrm{GSC}} \approx I_{\mathrm{PCC}}$.

At first, the impedance Z_{t} is assumed to consist of only the imaginary part. Thus $Z_{\mathrm{t}} = \mathrm{j}X_{\mathrm{t}}$. This means that the grid impedance Z_{grid}, the impedance of the faulty grid section $Z_{\mathrm{grid,f}}$ as well as the impedance at wind turbine's PCC $Z_{\mathrm{grid,WT}}$ are

inductive. If the PCC aligns the d-axis of its synchronous reference frame with the voltage $\underline{V}_\mathrm{f}$ such that $\mathrm{Im}(\underline{V}_\mathrm{f}) = 0$, the real and imaginary component of the voltage $\underline{V}_\mathrm{PCC,f}$ become

$$\begin{aligned} \mathrm{Re}(\underline{V}_\mathrm{PCC,f}) &= \underline{V}_\mathrm{f} - I_\mathrm{GSC,q} \cdot X_\mathrm{t} \\ \mathrm{Im}(\underline{V}_\mathrm{PCC,f}) &= I_\mathrm{GSC,d} \cdot X_\mathrm{t} \end{aligned} \tag{4.14}$$

Therefore, the maximum of possible deliverable active current for a certain grid fault case is achieved when $\mathrm{Im}(\underline{V}_\mathrm{PCC,f}) = |\underline{V}_\mathrm{PCC,f}|$ [81], [82]. Thus, $I_\mathrm{GSC,d,max}$ can be written as follows

$$I_\mathrm{GSC,d,max} = \frac{|\underline{V}_\mathrm{PCC,f}|}{X_\mathrm{t}} \tag{4.15}$$

Beyond this limit, there is simply no feasible solution for the (4.12) for a given fault condition and transmission impedance. Therefore, a grid-side converter needs to ensure that its active current remains below this limit during a grid fault. Otherwise, the PLL is not able to synchronize to the grid voltage and the Loss of Synchronization (LOS) happens.

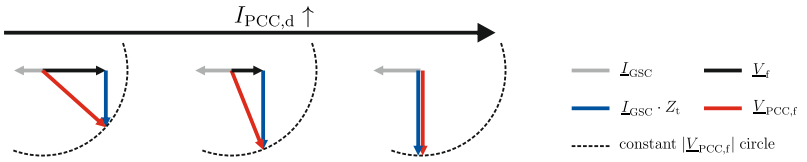

Figure 4.15: Phasor diagram during a grid fault under various I_GSC from low (left) to high (right)

The LOS can also be understood via the phasor diagram displayed in Fig. 4.15. The condition for this phasor diagram is that the phasor $\underline{I}_\mathrm{GSC}$ is in counterphase with the phasor $\underline{V}_\mathrm{f}$ because the pll aligns the d-axis of the reference frame with the V_f and the reactive or q-axis current $I_\mathrm{GSC,q}$ is considered to be 0. Since the magnitude of the voltage $\underline{V}_\mathrm{PCC,f}$ is independent on the converter current, with increasing active current delivery (from left to right), the phasor $\underline{V}_\mathrm{PCC,f}$ is shifted clockwise along the dotted line until it becomes perpendicular with the phasor $\underline{I}_\mathrm{GSC}$. This condition describes (4.15). If the active current is further increased,

there will be no feasible solution for a given magnitude of $\underline{V}_{\mathrm{PCC,f}}$. Therefore, the PLL is not able to synchronize with the grid voltage anymore and an instability occurs.

Figure 4.16 depicts the limit curves for the active or d-axis current component as a function of the fault residual voltage. This plot is obtained using the (4.15) and by varying the impedance $Z_{\mathrm{grid,WT}}$ to simulate different cases of the transmission impedance. The sum of $Z_{\mathrm{grid,WT}}$ and Z_{grid} is set to be 0.33 pu or equivalent to a short-circuit power of 3 pu. As displayed in this figure, the active current becomes more restricted with the increasing impedance $Z_{\mathrm{grid,WT}}$. Even if $Z_{\mathrm{grid,WT}}$ is set to 0 which practically represents the fault scenario 1, a certain active current restriction still exists particularly during faults with a very low residual voltage. In this scenario, the stray reactance of the wind turbine's transformer plays an important role in restricting the active current delivery.

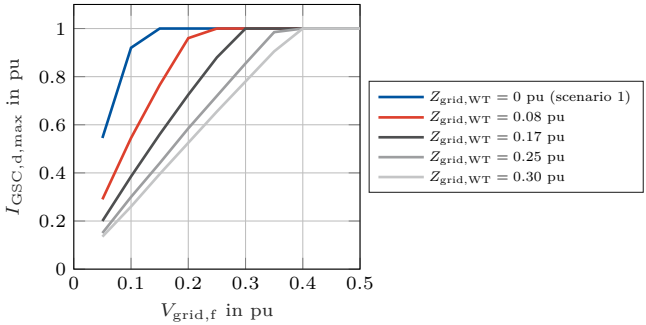

Figure 4.16: Limit of active or d-axis current delivery during grid fault

The simplest method to deal with this restriction is by deteriorating the active current down to 0 pu once the $V_{\mathrm{PCC,f}}$ falls below a certain threshold. For example, if scenario 1 is considered, this threshold can be 0.15 pu. However, this way will lead to LOS when the turbine encounters fault scenario 2 with the same residual voltage. This situation is displayed by the simulation results in Fig. 4.17 using the above mentioned baseline grid-side converter model. In this simulation, the converter operates at full power $I_{\mathrm{GSC,d}} = 1$ pu prior the occurrence of the grid fault.

As mentioned earlier, the baseline converter model observes for about 5 ms if the change in the grid voltage is caused by a fault. At the end of the observation period, the residual voltage is determined. If it is below 0.15 pu, the converter immediately sets its active current $I_{\mathrm{GSC,d}}$ to 0 pu to prevent LOS (refer to Fig. 4.16).

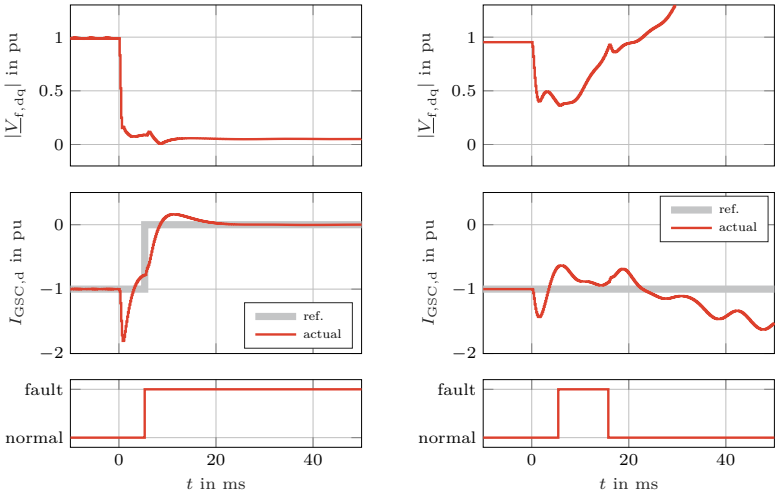

(a) Fault scenario 1
$Z_{grid} = 0.33\,pu$, $Z_{grid,WT} = 0\,pu$

(b) Fault scenario 2
$Z_{grid} = 0.08\,pu$, $Z_{grid,WT} = 0.27\,pu$

Figure 4.17: Simulation of a grid-side converter indicating the loss of synchronization

Otherwise, the active current is set to 1 pu to deliver active power as much as possible to the grid. As Fig. 4.17a shows, this strategy successfully prevents LOS in the fault scenario 1. Because the voltage $\underline{V}_{f,dq}$ is quite stable and not much influenced by the converter current thanks to low grid equivalent impedance. Hence, the converter correctly identifies the residual voltage that leads to an adjustment of the active current.

In Fig. 4.17b, the same strategy is applied but the converter encounters a grid fault with the scenario 2. As depicted in this figure, this fault scenario leads to different converter behavior and a converter instability is even observable. During the voltage observation period from the fault occurance at $t = 0\,ms$ until the converter sets its operation mode to "fault"mode at $t = 5\,ms$, the converter still delivers a nominal active current. Due to the voltage drop in the impedance $Z_{grid,WT}$ in addition to the voltage drop in the transformer impedance Z_σ, the measured voltage $\underline{V}_f$ is significantly higher in the fault scenario 2. As a result, the converter does not reduce its active current which finally results in a system instability due to LOS.

To improve the accuracy of residual voltage detection which plays an important role in deciding the active current delivery in an event of grid faults, a voltage sensor can be placed at the PCC. But, this adds cost and system complexity. To overcome this issue, a model-based approach can be used to estimate the voltage at PCC based on the delivered converter current. Nevertheless, this method is only effective in fault scenario 1. In case of fault scenario 2, the voltage drop across the impedance $Z_{\mathrm{grid,WT}}$ plays a significant role in the PCC voltage and the impedance $Z_{\mathrm{grid,WT}}$ is an unknown parameter. Therefore, an advanced method is required to prevent LOS. More importantly, testing under scenario 2 is crucial as it presents a more challenging operational situation for the grid-side converter of wind turbines.

4.4 Dynamic Behavior of Reference Nacelle during Grid Faults

In order to confirm that the above analysis, validation on the 2.75 MW reference nacelle was conducted within this thesis work. Although the reference nacelle is an open platform, the employed power-electronic converter is a nearly commercial platform with an enclosed system. Because the impedance of the electrical grid, to which the reference nacelle is connected, is not changeable, the validation work is done with the help of a validated simulation model. However, the detailed description of the converter of the reference nacelle can be found in [46].

4.4.1 Simulation Model and Validation

Model

For dynamic simulation purposes, a simulation model of the electrical drive-train of the 2.75 MW reference nacelle is implemented in the simulation software MATLAB/Simulink [67] in cooperation with the project partners. The converter is modeled as a controlled voltage source that considers the average of the converter's output voltage within one switching period. A linear behavior of the passive components are considered in the simulation. In order to correctly replicate the control behavior, the control firmware of the power-electronic converter is embedded as a *.dll data into the simulation model. The simulation is run with a simulation time step of 20 µs, sufficient for analyzing the dynamic behavior of current controller.

Validation

Prior to conducting analysis using the simulation model, its validity is verified with measurements. In particular, the validity of the taken assumptions in the simulation model with regards to the converter and passive components modeling are checked by measurements. For this purpose, a variable voltage source in a megawatt class having a fixed grid short-circuit power of 66 MVA or 21.6 pu, if referred to the nacelle's nominal power, is used. A detailed description of the variable voltage source can be found in [46].

By means of the variable voltage source, a voltage dip is applied at the PCC of the reference nacelle and the fed-in current by the reference nacelle is recorded using the data acquisition system in Fig. 2.8c. Prior to the voltage drop, the wind turbine operates at a power delivery P_{PCC} of $-1.29\,\mathrm{MW}$ or 47 % of its nominal active power. The voltage and the current on the low-voltage side of the wind turbine's transformer, v_{f} and $i_{\mathrm{PCC,LV}}$ respectively, are plotted in Fig. 4.18. To validate the simulation model, both simulation and measurement results are plotted in this figure.

As can be observed in Fig. 4.18, the simulation model is capable of replicating the dynamic behavior of the converter of the reference nacelle in the simulation environment. Although the switching of the converter is not modeled, the dynamic behavior of the converter in the simulation matches very well with measurement results with a small deviation. Beside converter switchings, the deviation is also attributed to the converter losses, namely the semiconductor losses. Therefore, the measured currents are slightly lower than the simulated currents. Nevertheless, the dynamic behavior of the converter controller is reproduced in the simulation with a good agreement. Hence, the simulation model is applicable for further analysis with a sufficient degree of validity.

4.4.2 Control Response under Various Grid Impedances

As briefly described in Section 4.1, depending on the architecture and control parameters, the current controller of a grid-side converter can be sensitive to the grid impedance. The control performance may deteriorate in terms of stability and control bandwidth if a wind turbine operates at an electrical grid with a low short-circuit power. To verify this hypothesis with the reference nacelle, an abrupt change in the q-axis reference current is applied to the control and the reaction is simulated under different grid short-circuit power. The simulation

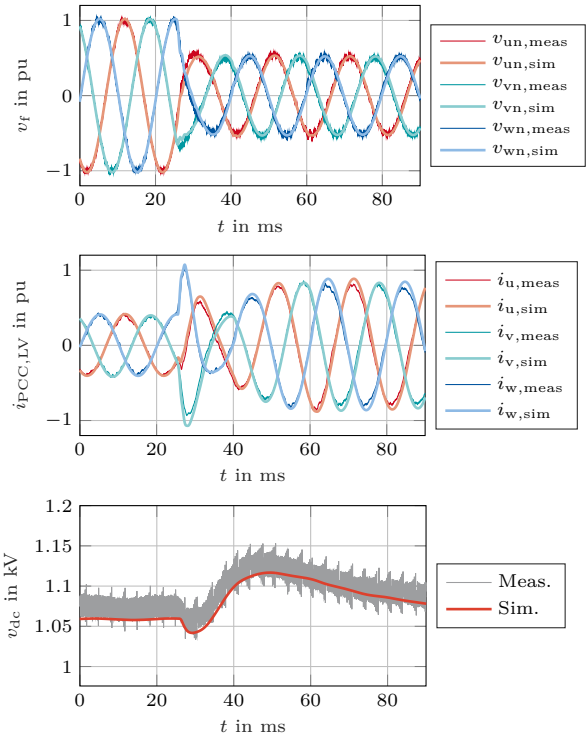

Figure 4.18: Validation of the simulation model of the 2.75 MW reference nacelle with measurements

results are plotted in Fig. 4.19.

Also with the reference nacelle, the effect of the grid impedance on the performance of the grid-side current controller is observable as displayed in Fig. 4.19. Aligned with the analysis in Section 4.1, the step response of at a low grid short-circuit power S_{grid} is significantly slower. This is an indication of a lower control bandwidth if the reference nacelle is operated at an electrical grid with a high short-circuit impedance i.e. a low short-circuit power. Hence, it is worth evaluating the behavior of the reference nacelle under different short-circuit fault scenarios presented in Section 4.2. Because, the dynamic performance of the current controller is highly important namely when considering the short time-frame of grid faults in the range of several hundreds of milliseconds. This is presented

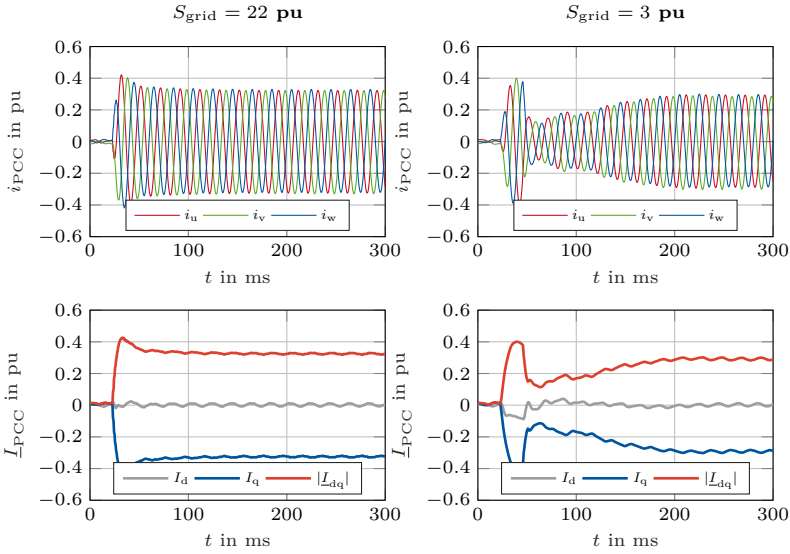

Figure 4.19: Response to an abrupt change in reactive or q-axis current reference at zero turbine power

in the following section.

4.4.3 Dynamic Behavior during Grid Faults

Current Controller Performance

In Fig. 4.20, the simulated behavior of the reference nacelle under two symmetrical short-circuit fault scenarios described in Section 4.2 are shown. For these simulations, the parameters listed in Table 4.2 are applied. The reference nacelle is programmed such that it immediately delivers a reactive current of 1 pu if it detects a grid fault via the grid voltage. Prior to the grid fault, the reference nacelle operates in a standby mode in order to decouple the influence of the active current component on the controller stability.

Aligned with the analysis in Section 4.3, a slower settling time of the reactive current in the short-circuit fault scenario 2 is also evident in the reference nacelle.

Table 4.4: Simulation parameters for the analysis of the dynamic behavior of the reference nacelle

Parameter	Variable	Scenario 1	Scenario 2
Grid impedance (source - faulty bus)	Z_{grid}	0.33 pu	0.08 pu
Grid impedance angle	ψ_{grid}	84°	84°
Grid impedance (faulty bus - PCC)	$Z_{\text{grid,WT}}$	0 pu	0.27 pu
Residual voltage	$\lvert\underline{V}_{\text{PCC,f}}\rvert$	0.2 pu	0.2 pu
Fault resistance	R_{fault}	0 pu	0 pu

The difference in the reactive current settling time is quantified in Table 4.5. The same definition for the settling time as described in Section 4.3 is applied here. Due to the higher grid impedance, the settling time in the scenario 2 is almost 4 times larger than the settling time in scenario 1. Nevertheless, large oscillations as in Fig. 4.11 and Fig. 4.13 are not observable in the reference nacelle. This indicates that the reference nacelle still has a sufficient phase margin to successfully perform the low-voltage ride-through task. It is worth to mention that the reference nacelle has similar values for the passive components in per unit value with the baseline grid-side converter in Table 4.1. Thereby, the limit curve for the active current delivery in an event of grid faults shown Fig. 4.16 is also valid for the reference nacelle.

Table 4.5: Settling time of the positive-sequence reactive current $I_{\text{PCC,r}}$ under a short-circuit fault

	Scenario 1	Scenario 2	Difference
Settling time	32.3 ms	127.6 ms	92.3 ms

Loss of Synchronization

In the previous discussion, the grid-side converter of the reference nacelle is in standby mode. When the reference nacelle encounters a grid fault while it is operating in the power production mode, an instability may occur particularly under the grid fault scenario 2 as displayed by the simulation results in Fig. 4.21. In this simulation, the same simulation parameters as in Table 4.5 are used but the reference nacelle is operating at $P_{\text{PCC}} = -2.75\,\text{MW}$. Meanwhile, the dynamic voltage support via a reactive current supply is in this simulation case is deactivated.

Due to the low grid impedance in the grid fault scenario 1, the reference nacelle detects the residual voltage at the faulty bus correctly and reduces the active

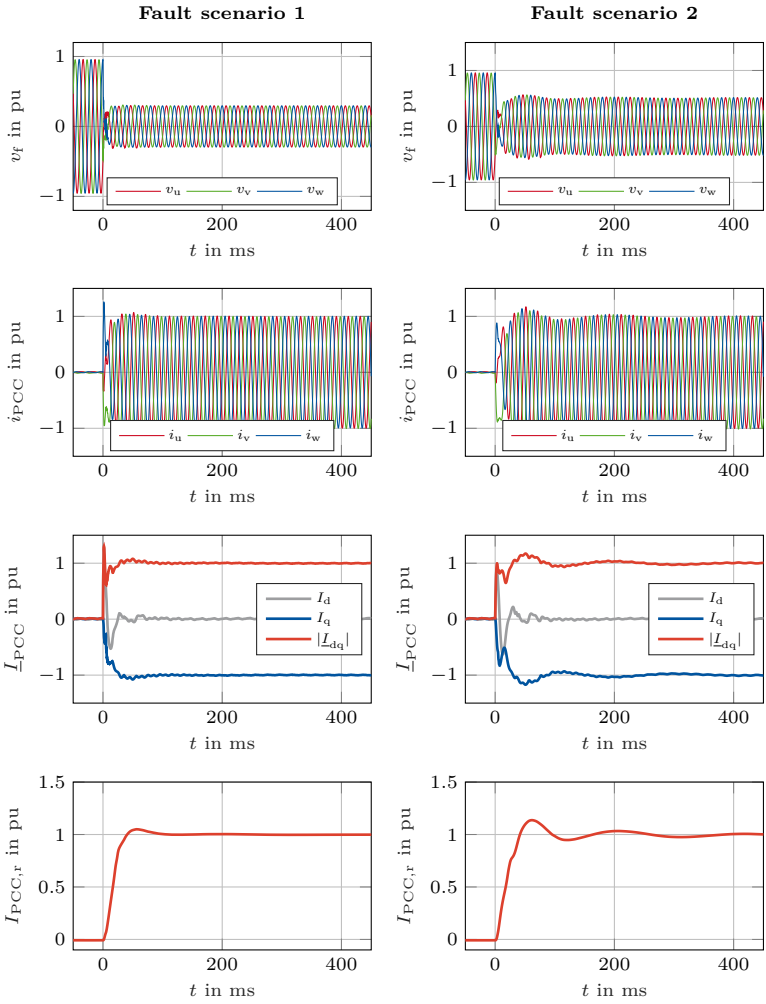

Figure 4.20: Dynamic behavior of a 2.75 MW reference nacelle under two symmetrical short-circuit fault scenarios

current to prevent the loss of synchronization from occurring. This is shown by the left figure in Fig. 4.21. However, the reference nacelle fails to estimate the

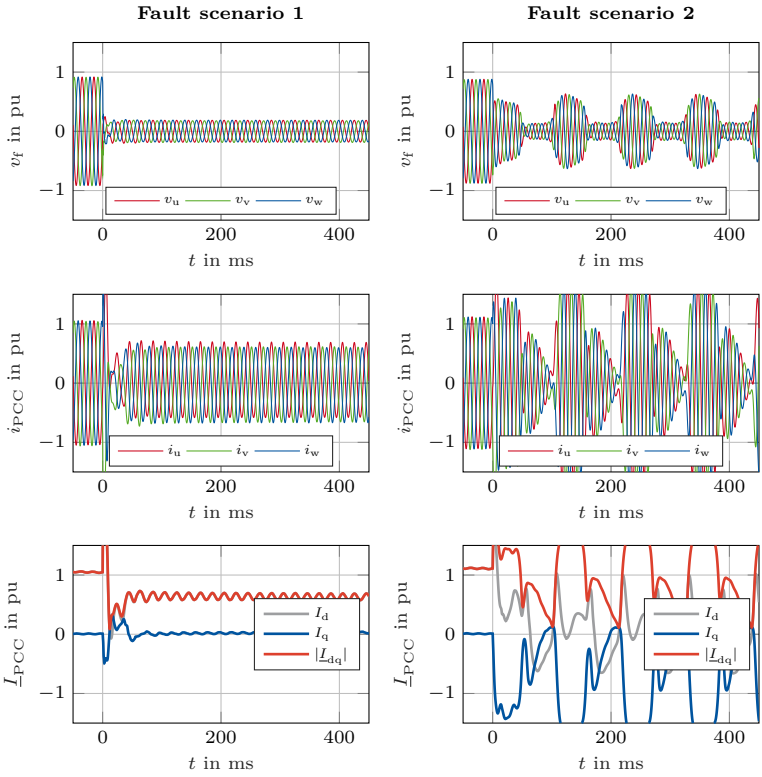

Figure 4.21: Loss of synchronization under two short-circuit fault scenarios

residual voltage correctly at the faulty bus due to the impedance $Z_{\text{grid,WT}}$, when it encounters a grid fault with scenario 2 as depicted by the right figure in Fig. 4.21. Instead of altering its active current, the reference nacelle maintains the active current at 1 pu. Therefore, the instability is inevitable.

Even though the reference nacelle is capable of maintaining its operation at the electrical grid without shutting down, if a dynamic voltage support via a reactive current supply is demanded, the reference nacelle is not able to perform the task correctly. This situation is not observable in fault scenario 1, which is commonly considered when evaluating a single wind turbine. Hence, it is highly recommended that fault scenario 2 is considered in a wind turbine testing.

4.5 Summary

Based on the analysis in this chapter, the small-signal grid impedance at the grid connection point (PCC) of a wind turbine influences the performance of the current controller of the grid-side converter (GSC), an important entity of a wind turbine to perform LVRT. Grid faults may differ in small-signal grid impedance depending on the fault location and grid structures. From the two examples of grid scenarios presented in this chapter, the fault scenario 2 presents a more challenging situation for wind turbines because due to the higher small-signal grid impedance.

5 Analysis on Regulatory Frameworks

In this chapter, the regulatory frameworks for grid code compliance tests will be analyzed in details. It aims at identifying the test conditions which can be used to derive the design criteria for grid emulators. Next to the technical guidelines for grid compliance tests [23], [24], [51], [83], the analysis from the perspective of the demand by the grid operators stipulated in grid codes will be elaborated in this chapter in particular in European countries such as Germany, Denmark, Norway and Great Britain [84]–[88]. This is done in order to obtain the picture from the conditions wind turbines will experience during the operation. The analysis is divided into three four main categories: static grid support, dynamic grid support, flicker and voltage quality.

5.1 Static Grid Support

Static grid support includes the long term voltage and frequency support up to several minutes or even continuously if the actual grid voltage and frequency deviate from their nominal value. Figure 5.1 summarizes the operation requirements for wind turbines in an event of voltage or frequency deviations in several European countries. As visualized in this figure, the demand in terms of operation window and contribution from wind turbines is grid specific. In terms of voltage, German grid allows a wider operation band that wind turbines must tolerate. On the other hand, a less reactive power contribution Q_{PCC} is demanded. Often, the amount of reactive power contribution is described in form of $\cos\phi_{\mathrm{PCC}}$ or known as power factor

$$\cos\phi_{\mathrm{PCC}} = \arctan\left(\frac{Q_{\mathrm{PCC}}}{P_{\mathrm{PCC}}}\right) \tag{5.1}$$

In contrast, grids in Great Britain and Norway tolerate a narrower voltage band but demand more reactive power contribution.

Regarding the frequency deviation, the grid code in Great Britain and Denmark

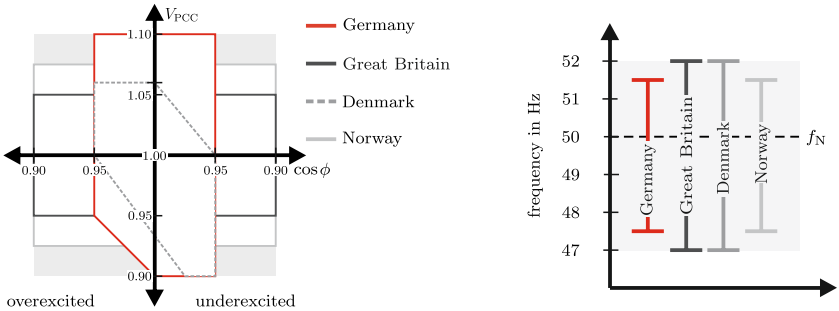

(a) Voltage support

(b) Frequency support

Figure 5.1: Static grid support

shows the widest frequency band, in which wind turbines must remain synchronized with the grid, compared to in other countries. Additionally, a power curtailment is also mandatory in case of overfrequency to prevent frequency runaway due to unbalance electricity production and consumption in the grid. Several advices have also been proposed that wind turbines shall increase their output power in case of underfrequency. Such a grid service can be enabled either by offsetting wind turbines' operation point from their aerodynamic maximum power point during normal operation allowing power increase in case of underfrequency [89]. Other potential method is by installing a battery storage system [90] to boost the output power if needed.

Compliance test

For compliance verification for the static voltage and frequency support, the IEC 61400-21 and the technical guideline by the Fördergesellschaft Windenergie und andere Dezentrale Energien (FGW) [83] in Germany recommend to modify the programmed nominal value of the voltage or frequency in a device under test while the test is performed under load. Thereby, the DUT detects a grid voltage or frequency deviation despited operating at the nominal values. Another method is by performing a test on a signal level only while the wind turbine is in an off state. Therefore, the application of a grid emulator shows a clear advantage to substitute this method because the influence of the voltage or frequency deviation on the power level can be verified. To cover the compliance test of the static grid support, a grid emulator shall continuously allow the operation range indicated

by the grey area in Fig. 5.1 at the nominal power of the device under test.

5.2 Dynamic Grid Support

5.2.1 Low-Voltage Ride-Through (LVRT)

Like conventional power plants, modern wind turbines must remain online in case of voltage dips for a certain duration t_{fault} in order to prevent a significant loss of power in-feed. This requirement is also known as LVRT. Figure 5.2 compares the residual voltage $V_{\text{PCC,f}}$ as a function of the fault duration t_{fault} beyond which wind turbines must remain synchronized with the electrical grids. Only relevant requirements particularly for multi-megawatt wind turbines are taken for the comparison in Fig. 5.2.

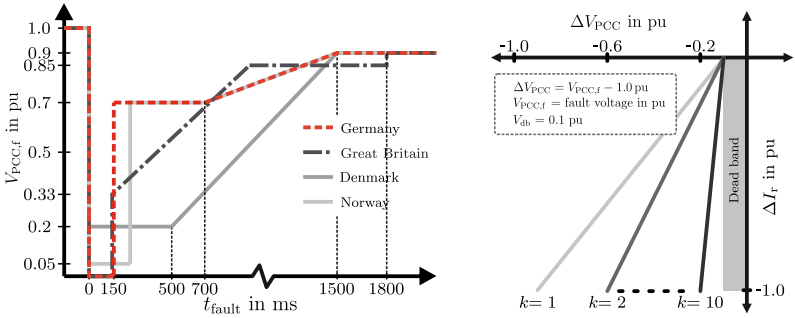

(a) LVRT borderline

(b) Reactive current support

Figure 5.2: Dynamic grid support

Specific for German grids, wind turbines shall additionally deliver a dynamic voltage support at the PCC via a reactive current injection [91]. This regulation is described in (5.2) and also graphically illustrated in Fig. 5.2b.

$$\Delta I_{\text{r}} = k \times (\Delta V_{\text{PCC}} + 0.1\,\text{pu}) \text{ for } \Delta V_{\text{PCC}} \leq 0\,\text{pu} \tag{5.2}$$

ΔI_{r} is the difference between the reactive current that must be injected to the PCC during fault events $I_{\text{r,fault}}$ and the reactive current being injected or absorbed

by a wind turbine prior to the fault $I_{\mathrm{r,pre}}$. ΔV_{PCC} is described as follows

$$\Delta V_{\mathrm{PCC}} = V_{\mathrm{pcc,f}} - 1\,\mathrm{pu} \tag{5.3}$$

where $V_{\mathrm{pcc,f}}$ is the residual voltage. In order to extract the reactive current component, the equations in Appendix A.3 shall be used according to [24].

Besides, ΔI_{r} is also influenced by a factor k in (5.2). According to [91], this factor may vary from 0 to 10. This factor is set upon agreement with the grid operators which offers them a freedom to adjust the contribution level to the grid voltage from a wind turbine depending on the situation of their grid. For instance, if $k = 10$, a wind turbine must provide $I_{\mathrm{r,fault}} = -1.0\,\mathrm{pu}$ when $V_{\mathrm{pcc,f}} = 0.8\,\mathrm{pu}$ and the wind turbine did not provide any reactive current prior to the fault i.e. $I_{\mathrm{r,pre}} = 0\,\mathrm{pu}$. The reactive current contribution during fault $I_{\mathrm{r,fault}}$ is limited to the nominal current at the PCC or $I_{\mathrm{r,fault}} = 1.0\,\mathrm{pu}$.

Compliance Test

As mentioned in Section 1.2, the standard IEC 61400-21 and the FGW technical guideline for grid compliance verification tests of wind turbines [23] recommend to utilize an inductive divider in Fig. 1.2 to conduct LVRT tests for wind turbines. Besides, there are three essential points that require special attention when conducting LVRT tests. These points will be elaborated in the following with the aim to derive the specifications for a grid emulator.

- Voltage dynamic

  The voltage dynamic here represents how quick the voltage emulated by a test equipment reaches its final residual voltage from the initiation instant of a voltage dip. Although there has been no publications that address the influence of the voltage dynamic on the LVRT performance of a wind turbine with a full-scale converter, several publications and standards stipulate a certain criteria for LVRT tests.

  According to the IEC standard [24] and FGW technical guideline [23], an LVRT test is performed by applying a blockwise voltage waveform as shown in Fig. 5.3a. To ensure the validity of an LVRT test, the instantaneous positive-sequence component of the PCC voltage must stay within the tolerance area

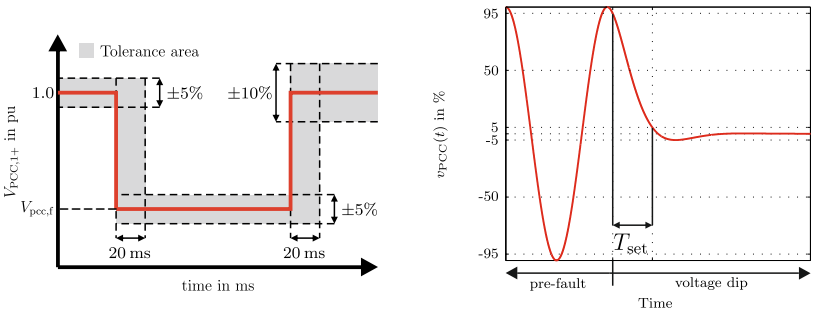

(a) LVRT test voltage waveform

(b) Settling time T_{set}

Figure 5.3: LVRT test voltage according to IEC 61400-21

colored in grey. It must be remarked that the test voltage waveform is to be verified with a disconnected DUT which excludes the DUT contribution to the voltage waveform. This means that the voltage may deviate from the tolerance area depending on the impedance of the test equipment and the DUT current.

Due to the integration in the calculation process for the positive-sequence voltage, the test voltage waveform in Fig. 5.3a cannot be directly used to determine the requirement on the voltage dynamic of a grid emulator. Recommendations are made in several publications [32], [92], [93] for the settling time of the instantaneous voltage (refer to Fig. 5.3b). These recommendations are summarized in Table 5.1. Different background has been taken into account in these publications to derive the specification on the voltage dynamic for grid emulators.

Table 5.1: Settling time of the instantaneous PCC voltage for LVRT tests

Reference	**Settling time** v_{pcc}
[93]	1 ms
[32]	1 ms
[92]	2.5 ms

In a recent publication [93], a settling time of 1 ms is proposed which was derived from the field measurements of several voltage dip events in a power grid. In a power grid, the voltage waveform is likely to be influenced by many factors such as generation unit and loads, fault location, grid structure, etc. Abad et al. in [32] studies the transient torque of a doubly-fed generator when

it encounters a grid fault. According to this study, peak transient torque with 1 ms settling time is comparable with an abrupt voltage dip.

In contrast, the author in [92] recommends a settling time of 2.5 ms. With this value, the instantaneous positive-sequence voltage still stays within the tolerance area in Fig. 5.3. Furthermore, the deviation in the peak transient torque of a doubly-fed generator is still below 5 % as compared to that with $T_{\mathrm{set}} = 1\,\mathrm{ms}$. This value is still considered to be low. In this thesis, 2.5 ms will be taken as the first design target to fulfill the criteria in Fig. 5.3. Besides, the switching frequency of commercially available power-electronic converters in the considered power range is quite low. Thereby, the possible control dynamic range is restricted.

- Grid impedance

  Another crucial aspect to be considered for compliance tests of LVRT is the impedance provided by the test equipment. Previous chapters have revealed the importance of the grid impedance as it determines the performance of wind turbines. Although the IEC 61400-21 does not specify this, the technical guideline FGW TR3 demands the following specification for the grid impedance:

$$\begin{aligned} 3\,\mathrm{pu} \leq S_{\mathrm{grid}} \leq 33\,\mathrm{pu} \\ X_{\mathrm{grid}}/R_{\mathrm{grid}} > 3 \end{aligned} \tag{5.4}$$

  One remark from (5.4) is that a broad range of grid short-circuit power is accepted. This may lead to a wide variation in terms of the control performance of the grid-side converter as briefly elaborated in to Chapter 4.

  When looking at the recommended test setup for LVRT tests in Fig. 1.2b, it only represents the fault scenario 1 (refer to Chapter 4). Principally, adding an inductor between the test equipment and the wind turbine is possible to build the fault scenario 2. However, the series inductance of the test equipment X_{sr} must be reduced in order to maintain the impedance of the pre- and post-fault conditions within the operational limit of the DUT. As a consequence, the local power grid can be severely disturbed during the test and the protection equipments might response as a real short-circuit fault is introduced in the electrical grid.

  It seems that IEC standards and FGW technical guidelines have not precisely defined the requirements on the grid impedance namely during the period of

the voltage dip. Although grid emulators may provide a high flexibility in terms of test scenario, th influence of their control on the performance of the device under tests is still questionable. This topic will be discussed in the next chapter.

- Fault type

  Regarding the type of voltage dips, both symmetrical and asymmetrical voltage dips must be applied for LVRT compliance tests. Due to the installation of a Dyn transformer, the zero sequence component of an asymmetrical voltage dip does not propagate from the medium-voltage onto the low-voltage side of the transformer. Thereby, LVRT tests with asymmetrical voltage dip that contain a zero sequence component is not mandatory. The resulting voltage vector and time-series voltage waveform of an asymmetrical voltage dip is shown in Fig. 5.4. In this example, the voltage phase a is the faulty phase. Because of zero-sequence component, the sum of the three-phase voltages remains zero. Consequently, the magnitude of the non-faulty phases will drop while the phase is shifted.

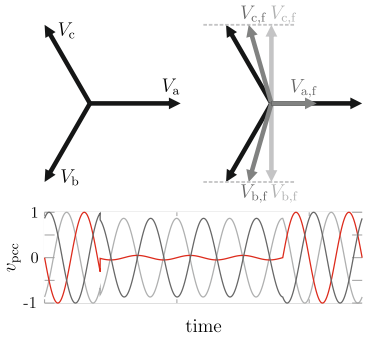

Figure 5.4: Test voltage waveform for asymmetrical LVRT tests

5.2.2 High-Voltage Ride Through (HVRT)

Recently, a high-voltage ride-through (HVRT) capability of wind turbines is requested by grid operators in addition to the LVRT. HVRT is defined as the capability of a wind turbine to maintain its synchronous operation with the power grid in case overvoltages beyond the upper votage limit in Fig. 5.1a. With the increas-

ing grid voltage, the grid-side converter will need to elevate its dc-link voltage to maintain the controllability without entering the overmodulation. However, too high dc-link voltage will harm the installed semiconductor devices.

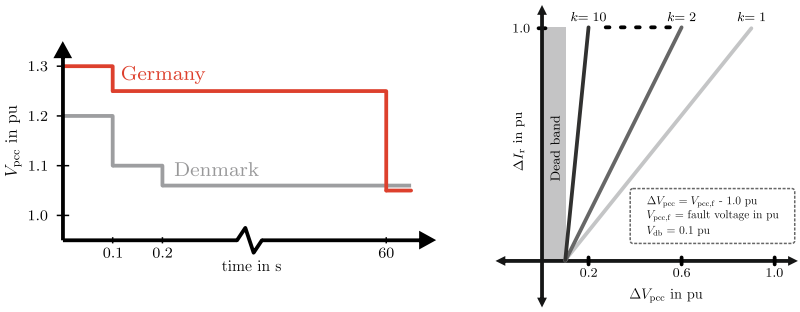

(a) HVRT borderline

(b) Reactive current support [94]

Figure 5.5: Dynamic grid support

Figure 5.5a illustrates the HVRT applied in Germany and Denmark whereas this requirement is still not found in Great Britain, Norway and even on the European level. As observed in Fig. 5.5a, wind turbines in Germany must ride through grid voltages up to 130 % of the nominal value. Additionally, reactive current support as illustrated in Fig. 5.5b is also prescribed. (5.2) can be applied to determine the magnitude of the reactive current $I_{\mathrm{r,fault}}$ that must be fed in into the power grid in an event of overvoltages.

Compliance Test

Due to the flexibility of the power-electronic converter, grid emulator can also establish overvoltages at PCC. Nevertheless, a solution involving only passive components has been introduced recently. The schematic of the HVRT test equipment is shown in Fig. 5.6 [95]. The test setup is developed based on the similar concept as in Fig. 5.3a, only the parallel component is replaced by a capacitor. Thereby, the obtained PCC voltage follows the equation (5.5). A resistance is installed in series with the capacitor to dampen the resonance resulted from the introduction of parallel capacitor after the closing of CB_2.

$$V_{\mathrm{PCC}} = \frac{1}{1 - X_{\mathrm{sr}} X_{\mathrm{sc}}} \text{ in pu, } R_{\mathrm{sc}} = 0 \tag{5.5}$$

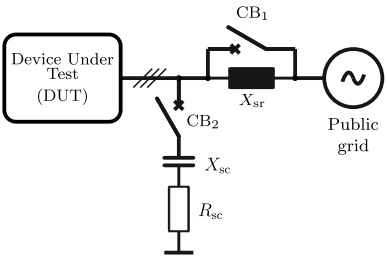

Figure 5.6: HVRT test equipment based on an inductive-capacitive voltage divider [95]

5.3 Flicker

As described in previous chapter, the fluctuation of the wind turbine's output power can induce voltage flicker in power grids. The flicker severity limits set by the grid codes of European countries are summarized in Table 5.2. As can be seen in this table, flicker severity limits are quite diverse among the grid codes. ENTSO-E even does not specify any limits for flicker severity meaning that this parameter is not harmonized among the European countries. In Denmark, no general limit has been specified for flicker severity level but grid operators allow any flicker severity levels as long as the limits for individual substations, to which a wind turbine is connected, are not exceeded. The limits given in Table 5.2 for Denmark is taken from the older version of the grid code and is shown here for information purpose.

Table 5.2: Flicker severity limits in European grid codes

Grid code	$\mathbf{P}_{\mathrm{st}}$	$\mathbf{P}_{\mathrm{lt}}$
ENTSO-E	n.a.	n.a.
Germany	n.a.	0.46
Denmark	0.5	0.5
Norway	0.6	n.a.
Great Britain	1	0.8

Compliance test

As elaborated in detail in Chapter 3, the weaker the grid connection is, the higher is the flicker severity level due to the higher voltage drop across the grid impedance. However, the grid impedance is typically unknown prior to the deployment of wind turbines. Therefore, IEC 61400-21 standardizes a test procedure to estimate the flicker severity level induced by a wind turbine based on measurements on a certain test site which is followed by a simulation. The IEC flicker measurement procedure is illustrated in Fig. 5.7 and described in the following.

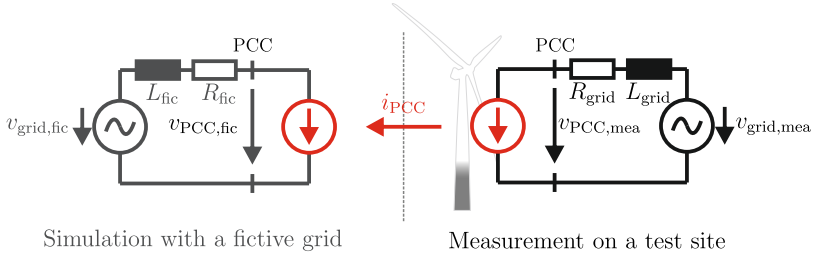

Figure 5.7: Voltage flicker measurement procedure according to IEC 61400-21 [24]

While a wind turbine is operating on a test site, the PCC voltage and current are captured for the entire range of operation wind speeds (from the cut-in to cut-out wind speed). Aferwards, the measured current is fed into a simulation with a fictive grid composed by an ideal voltage source $v_{\text{grid,fic}}$ and a fictive grid impedance (L_{fic} and R_{fic}) where

$$v_{\text{grid,fic}}(t) = \sqrt{2} \cdot V_{\text{WT,N}} \cdot \sin(2 \cdot \pi \cdot f_{\text{grid},1} + \theta_{\text{grid,fic}}) \text{ in V} \tag{5.6}$$

$V_{\text{WT,N}}$ denotes the nominal voltage. The phase of the voltage $v_{\text{grid,fic}}$ must be synchronized with the phase of PCC voltage at the test site, thus $\theta_{\text{grid,fic}} = \theta_{\text{PCC,mea}}$. The flicker severity level is obtained by feeding the simulated voltage v_{fic} into the IEC flickermeter in Fig. 3.2. By varying L_{fic} and R_{fic}, the severity level of the voltage flicker caused by a wind turbine under different grid impedances can be obtained via simulation without having to install the wind turbine in other locations with the desired grid characteristics. In IEC 61400-21, further statistical evaluation steps are given to deal with the occurance probability of wind speeds. However, this is not discussed in this thesis.

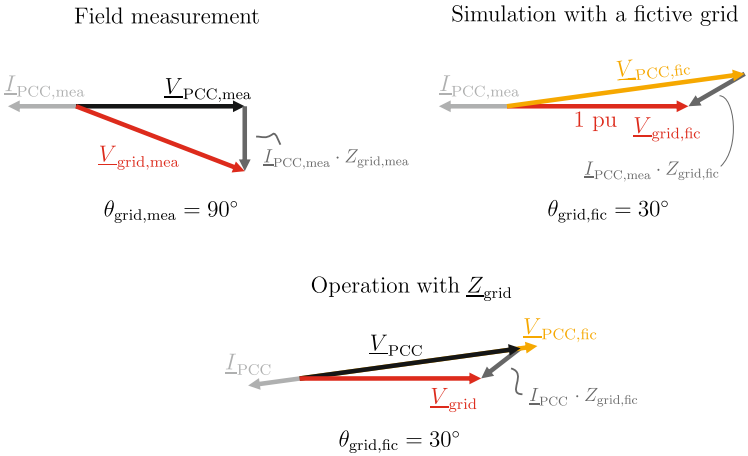

Figure 5.8: Phasor diagrams at fundamental frequency showing a discrepancy in the simulation-based flicker measurement method with a fictive grid

From the described procedure, a potential mismatch between the outcome from the simulation with a fictive grid and the real wind turbine operation at the same grid impedance can be identified. This issue is explained graphically by the phasor diagrams at the fundamental frequency in Fig. 5.8. For this example, a field measurement takes place at an electrical grid having an impedance angle of $\theta_{\mathrm{grid,mea}} = 90°$. Meanwhile, the voltage behavior with a grid impedance angle of $\theta_{\mathrm{grid,mea}} = 30°$ shall be determined with the help of a fictive grid. Both, the grid impedance at the measurement field $\underline{Z}_{\mathrm{grid,mea}}$ and the grid impedance of the fictive grid $\underline{Z}_{\mathrm{grid,fic}}$ are the same in magnitude. For comparison purpose, the phasor diagram if the wind turbine operates with a fictive grid is also given in Fig. 5.8.

Since a wind turbine behaves like a constant power source, the current phasor $\underline{I}_{\mathrm{PCC,mea}}$ is aligned to the phasor of the PCC voltage $\underline{V}_{\mathrm{PCC,mea}}$. In the simulation with a fictive grid, $\underline{I}_{\mathrm{pcc,mea}}$ will be aligned to the grid voltage vector $\underline{V}_{\mathrm{grid,fic}}$ instead of to the PCC voltage vector $\underline{V}_{\mathrm{PCC,fic}}$ as presented by the top right phasor diagram in Fig. 5.8. Here, a certain reactive power flow appears at PCC in the simulation. If a wind turbine would operate with a grid impedance specified in the simulation $S_{\mathrm{grid,fic}}$ and $\theta_{\mathrm{grid,fic}}$, the current phasor $\underline{I}_{\mathrm{PCC}}$ would be aligned with the PCC voltage phasor $\underline{V}_{\mathrm{PCC}}$ illustrated by the lower phasor diagram in Fig. 5.8.

To highlight the disagreement in V_{PCC} between the outcome from simulation and the expected result, the PCC voltage phasor from simulation is also drawn in the phasor diagram. Here, it becomes obvious that the measurement procedure in IEC to determine voltage flicker may lead to discrepancies with the expected result. It depends on several aspects namely the grid voltage and the impedance on the test field as well as the impedance of the fictive grid.

Figure 5.9b quantifies the discrepancy of the outcome from the conventional flicker measurement procedure for various combinations of $\underline{Z}_{\mathrm{grid,mea}}$ and $\underline{Z}_{\mathrm{grid,fic}}$. The color indicates the magnitude of the discrepancy defined as:

$$\Delta V_{\mathrm{PCC}} = |\underline{V}_{\mathrm{PCC}}| - |\underline{V}_{\mathrm{PCC,fic}}| \text{ in pu} \tag{5.7}$$

Figure 5.9b reveals that the disagreement occurs particularly in a very low $S_{\mathrm{grid,fic}}$ or large $\underline{Z}_{\mathrm{PCC,fic}}$. In case of $|\underline{V}_{\mathrm{PCC,mea}}|$ equals 1 pu(Fig. 5.9b), a maximum ΔV_{PCC} of 0.1 pu is even possible which is already equivalent to the voltage operation window for Great Britanian grid. As displayed in Fig. 5.8, even if the device under test is operating with zero reactive power on the test site, the current phasor in the simulation with a fictive grid is no longer in phase with the PCC voltage. This results in a similar effect as the device under test is supplying reactive power to the grid. Thereby, the voltage drop across the fictive grid impedance is no longer solely affected by the active current but also the reactive current which in turn influences the PCC voltage. A higher ΔV_{PCC} is even obtained if the grid voltage on the test site is below the nominal voltage Fig. 5.9a. Consequently, the measured current on the test site would become higher with for the same power leading to a higher voltage drop across the fictive grid impedance.

Another drawback from the conventional method is that the contribution of the flicker mitigation strategy by wind turbines [63], [96], [97] cannot be precisely evaluated. Nevertheless, because changing grid impedance of the real grid is not possible, this method has been used to conduct flicker measurements. Concerning the discussed drawbacks of the conventional flicker measurement method, the power-electronic-based grid emulator is a promising alternative thanks to the flexibility of the emulated voltage. However, a grid emulator must be able to correctly emulate various grid impedances with a sufficient dynamic.

To derive the voltage dynamic criteria for grid emulators for flicker measurements, simulations of the 2.75 MW reference nacelle coupled to a grid emulator model are carried out. The structure of the simulation is depicted in Fig. 5.10a. The grid emulator in this simulation is approached by a controlled voltage source

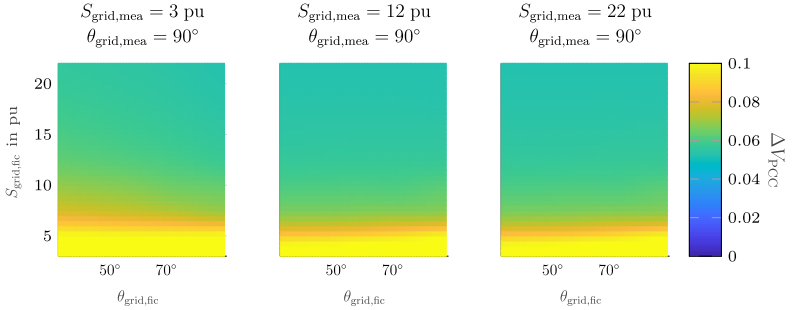

(a) $|\underline{V}_{\text{PCC,mea}}| = 0.95$ pu

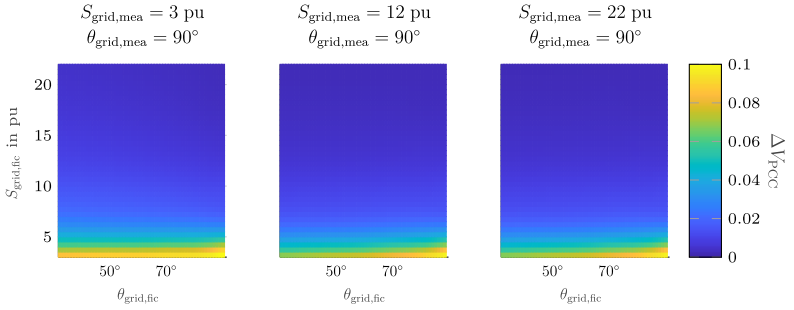

(b) $|\underline{V}_{\text{PCC,mea}}| = 1$ pu

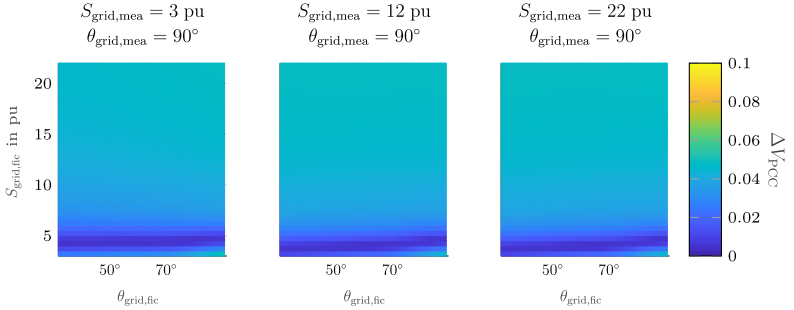

(c) $|\underline{V}_{\text{PCC,mea}}| = 1.05$ pu

Figure 5.9: PCC voltage discrepancy resulted from the conventional flicker measurement method

with a lowpass filter (LPF) which mimics the voltage control dynamic of the grid emulator. Note that the grid emulator modeling and the grid impedance emulation are performed in a synchronous reference frame. In these simulations, the grid emulator model emulates an electrical grid with S_{grid}= 3 pu and θ_{grid} = 30°. The mismatch in flicker severity level e_{Pst} caused by the LPF is shown Fig. 5.10b where e_{Pst} is defined as

$$e_{\text{Pst}} = \frac{\text{P}_{\text{st}} - \text{P}_{\text{st,fil}}}{\text{P}_{\text{st}}} \times 100\,\% \tag{5.8}$$

P_{st} is the flicker severity level without the low-pass filter while $\text{P}_{\text{st,fil}}$ indicates the flicker severity level with a filtered voltage source.

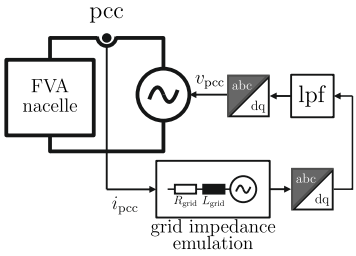

(a) Simulation structure

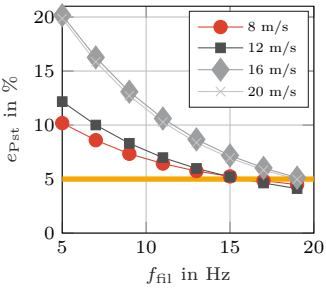

(b) Error in short-term flicker e_{Pst} as a function of the grid emulator voltage dynamic

Figure 5.10: Validation of the dynamic requirement of for grid emulators in simulation

According to the presented simulation results in Fig. 5.10b, when a grid emulator is capable of emulating a grid impedance correctly and dynamically up to a frequency of 20 Hz, flicker measurements can be conducted with a sufficient accuracy. According to IEC standard 61000-4-15 [51], the acceptable limit for flicker severity level P_{st} is 5 %. Such a high dynamic criteria for grid emulator is contributed by the fact that flickermeter is particularly sensitive at this frequency range.

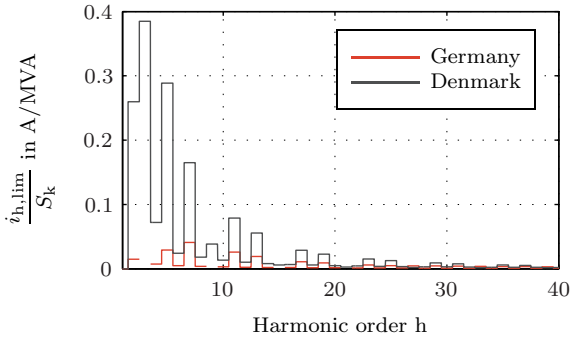

Figure 5.11: Comparison of current harmonic limits in Germany and Denmark

5.4 Harmonic Distortion

Modern wind turbines are equipped with power-electronic converters. On the one hand, it enables a variable-speed operation of the WT allowing it to always operate at its maximum aerodynamic efficiency [98], [99]. On the other hand, the harmonic content in the supplied current caused by the switchings of the converter and space harmonics of doubly-fed generator (DFG) [100] may deteriorate the power quality at the consumer end. Thus, the harmonic distortion of the WT must be limited in order to guarantee a sufficient power quality received by the consumer and to maintain the stability of the grid operation.

Figure 5.11 shows an example of the limits for the harmonic content in the supplied electrical current of a wind turbine at PCC. The grid codes define the limits for the effective currents of harmonics $I_{\mathrm{PCC,h,lim}}$ normalized to the short-circuit power of the grid S_{grid}. This seems that the limits in grid codes have been determined by limiting the voltage across the grid impedance due to the harmonic currents to a constant value [92]. Hence, the $I_{\mathrm{PCC,h,lim}}$ becomes lower as the S_{grid} gets smaller.

Compliance Test

According to IEC 61400-21, the harmonic content in the supplied PCC current of a wind turbine must be measured on a test site for the entire range of operating wind speeds. However, it is crucial to conduct this measurement on an electrical

Table 5.3: Comparison of $\mathrm{THD_{v,PCC}}$ between various standards

Standard or technical guidelines	$\mathrm{THD_{v,PCC}}$	**Amplitude individual harmonics**
IEEE 519-2014	5 %	3 %
EN 61000-2-4	8 %	0.2 %
IEC 61400-21	5 %	not available

grid with a low harmonic content. Otherwise, the harmonic currents due to the harmonics in the grid voltage are measured together with the harmonics induced by WT resulting in an inaccurate measurements. Therefore, the harmonic content in the grid voltage must be limited which is defined by the so-called total harmonic distortion $\mathrm{THD_{v,PCC}}$ in (5.9).

$$\mathrm{THD_{v,PCC}} = \frac{\sqrt{\sum_{h=2}^{50} |V_{\mathrm{PCC,h}}|^2}}{V_{\mathrm{PCC,N}}} \times 100\,\% \tag{5.9}$$

$\mathrm{THD_{v,PCC}}$ is obtained via a geometrical summation of the voltage harmonics $V_{\mathrm{PCC,h}}$ between the harmonic order $h = 2$ and $h = 50$ normalized to the nominal voltage $V_{\mathrm{PCC,N}}$. The harmonic order h is a ratio between the frequency of the harmonic $f_{\mathrm{PCC,h}}$ and the fundamental frequency $f_{\mathrm{PCC,1}}$. According to the standard IEC 61400-21 [24], $\mathrm{THD_{v,PCC}}$ must be lower than 5 %. However, this limit only covers the frequency range in (5.9) even though the harmonic assessment shall be carried up to the harmonic order $h = 180$. If the harmonic assessment shall be conducted on a test bench using a grid emulator with power-electronic converters, depending on the switching frequency and the topology, the power-electronic converters may produce harmonics with $h > 180$. So far this issue has not been addressed in the standard IEC 61400-21.

Since the harmonic assessment is not the focus of this thesis, grid emulator will be designed to obtain $\mathrm{THD_{v,PCC}} < 5\,\%$ but the frequency range for $\mathrm{THD_{v,PCC}}$ calculation will be extended up to $h = 180$. Thereby, the synchronous operation of WTs on the emulated grid is enabled. There has been an attempt to define new requirements on the harmonic content in the PCC voltage to allow harmonic assessment tests with a grid emulator [92]. In this paper, $\mathrm{THD_{v,PCC}}$ is not used but rather the voltage amplitude limits for harmonics $V_{\mathrm{PCC,h}}$ are derived.

6 Multi-Megawatt Grid Emulator

Within this chapter, a multi-megawatt grid emulator based on a power-electronic converter system is discussed. Firstly, the topology and the proper passive filter design to achieve the target voltage quality are elaborated. Afterwards, a possible control structure namely the emulation of grid impedance is described which is followed by the characterization at the PCC. Lastly, the coupling analysis with a device under test will be presented. The following analysis highlights the behavior of the device under test at the PCC regarding the two grid compliance tests discussed in the previous chapters, flicker and low-voltage ride-through (LVRT). Based on the discussion in Chapter 5, the design criteria for the grid emulator considered in this chapter is given in Table 6.1.

Table 6.1: Specification of the considered grid emulator

Parameter	**Symbol**	**Value**
Nominal values		
Power	$S_{\mathrm{PCC,N}}$	5 MVA
Voltage	$V_{\mathrm{PCC,N}}$	20 kV
Frequency	$f_{\mathrm{PCC,N}}$	50 Hz
Current	$I_{\mathrm{PCC,N}}$	144.3 A
Voltage THD	$\mathrm{THD}_{\mathrm{v,PCC}}$	¡ 5 %
Operation range		
Voltage	V_{PCC}	$0.9 \cdot V_{\mathrm{PCC,N}}$ ... $1.1 \cdot V_{\mathrm{PCC,N}}$
Frequency	f_{PCC}	47 Hz ... 52 Hz
Power factor	$\cos\phi_{\mathrm{PCC}}$	-0.9 ... +0.9
Voltage dynamic		
Settling time	T_{set}	$\leq$ 2.5 ms

6.1 Topology

6.1.1 Review on the State-of-the-Art

The selection of the topology for a grid emulator is mainly driven by the power requirement while still meeting the design criteria in terms the voltage quality and

dynamic, the key requirements for a grid emulator. There are several topologies for a grid emulator that can be found in several publications with different target application fields [4]–[7], [9], [10], [12], [101]–[106]. All of them are based on a voltage-source converter system. These topologies are summarized in Fig. 6.1.

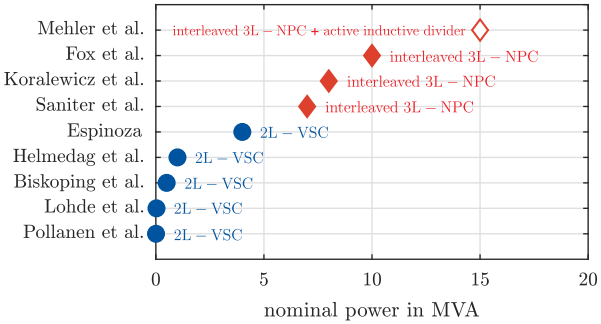

Figure 6.1: Various grid emulator topologies in several publications [4]–[7], [9], [10], [12], [101]–[106]

It is evident from Fig. 6.1 that the topology with one or multiple two-level voltage source converters (2L-VSC) is preferred for power levels from kVA range up to several MVA. This topology is typically equipped with an *LC* filter unit to dampen the voltage harmonics caused by converter switchings. Thereby, the required voltage quality can be reached.

For higher power levels, the preferred topology in the publication is the concept employing the interleaved switching of multiple medium-voltage MV three-level neutral-point clamped (3L-NPC) converters. The converters are linked in parallel via transformers or couple inductors. The reason is because the grid emulators in [4]–[7], [105], [106] are intended for offshore wind turbines with a high nominal power (typically beyond 5 MVA). Hence, a parallel connection of multiple MV converters is inevitable. The interleaved switching is implemented because it adds benefits in terms of increasing the effective switching frequency of the converter system thus lowering the filter size and improving the dynamic performance despite of the restricted converter switching frequency.

Because the nominal power of onshore wind turbines are typically lower than 5 MW, the grid emulator can be built from a commercially-available MV converter. However, the switching frequency of MV converters is typically much lower than that of low voltage (LV) converters. Hence, the resonance frequency of the *LC* filter must be tuned very low which may limit the voltage dynamic

and the usable converter power due to the high reactive power in the *LC* filter. Although [107] shows that the requirement on the voltage settling time as in Table 6.1 is achievable with this concept, it may not be able to cover the transient current caused by doubly-fed generators which is significantly higher compared to the transient current of the full-scale converter [83]. Therefore, this thesis considers also interleaved switching of multiple 3L-NPC converters for the grid emulator. This concept will be elaborated further in the following section.

6.1.2 Interleaved Converters

The topology of the considered grid emulator applying interleaved converters is displayed in Fig. 6.2. Principally, this concept follows the one presented by Saniter et al. in [4], [105]. Three MV 3L-NPC converters are connected in parallel via a multi-winding transformer to step up the voltage from around 3 kV to 20 kV at PCC. The converters are linked to the same dc bus with a dc-link voltage $V_{\mathrm{dc,GEM}}$ of 5 kV. The dc-link voltage is regulated by an active front-end (AFE) which simultaneously provides a link to a public grid. Unlike in [4], [105], a passive filter unit consisting of a capacitor $C_{\mathrm{f,GEM}}$ and resistor $R_{\mathrm{f,GEM}}$ are connected to an additional winding in order to improve the voltage quality at PCC even under no-load condition. This avoids the installation of expensive 20 kV filter unit as well as to save the installation space. The key data of the 3L-NPC and the multi-winding transformer considered in this thesis are given in Table 6.2.

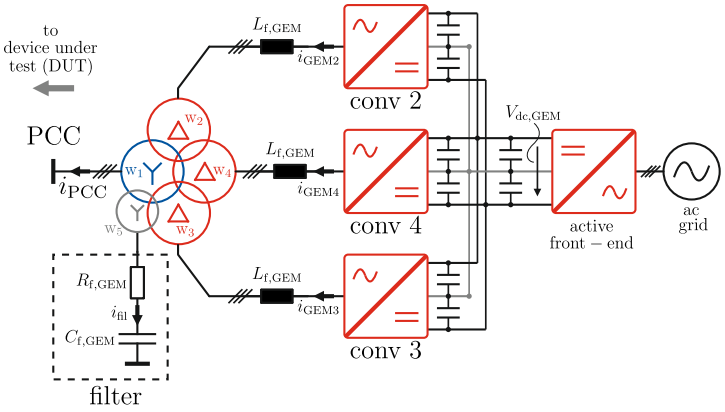

Figure 6.2: Topology of a grid emulator applying interleaved medium-voltage (MV) converters

Table 6.2: Technical data of the grid emulator

Parameter	Symbol	Value
Converter		
Topology	$V_{\mathrm{dc,GEM}}$	5 MVA
DC-link voltage	$V_{\mathrm{PCC,N}}$	20 kV
Semiconductor switches		ST2100GXH24A [108]
Anti-parallel diodes		D1301SH [109]
Clamping diodes		D1301SH [109]
Carrier frequency	f_{car}	1050 Hz
Multi-winding transformer		
Nominal voltage	$V_{\mathrm{w1,N}}$, $V_{\mathrm{w5,N}}$, $V_{\mathrm{w2-w4,N}}$	20 kV, 6 kV, 3 kV
Nominal power	$S_{\mathrm{w1,N}}$, $S_{\mathrm{w5,N}}$, $S_{\mathrm{w2-w4,N}}$	8 MVA, 2 MVA, 2 MVA

Basic Operation of a Three-Level Neutral-Point-Clamped Converter

Figure 6.3 shows the structure as well as the modulation scheme of a 3L-NPC [110]. $v_{\mathrm{car,top}}$ and $v_{\mathrm{car,bot}}$ are the carrier signals for the positive and negative cycle of m_{x} respectively. m_{x} is the voltage reference of the phase x set by a converter controller at every edges of the carrier signals. In the modulation process, the reference signals m_{x} are compared with the carrier signals to determine the switching states of the converter following the switching table presented in Table 6.3. As a result, the terminal voltage of the converter with respect to its dc-link midpoint v_{xN} will have three voltage levels as shown in Fig. 6.4. Consequently, the line-to-line voltage of the converter v_{xx} will contain five levels as depicted in Fig. 6.4.

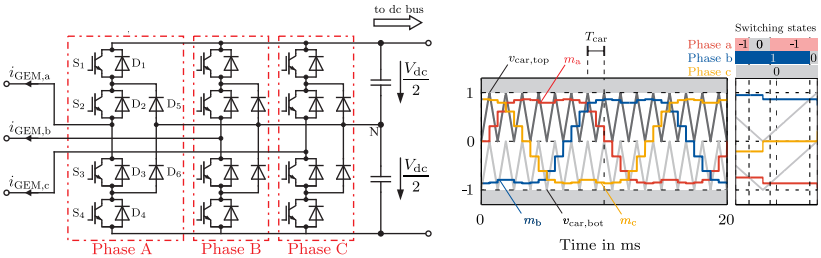

Figure 6.3: Circuit topology and modulation strategy of a three-level neutral-point-clamped converter [110]

It can be observed from Fig. 6.4 that the spectrum of the converter's line-to-line voltage contains not only the fundamental frequency component but also

Table 6.3: Phase leg switching states of a 3L-NPC converter

Condition	State	S_1	S_2	S_3	S_4	v_{xN}
$m_x > v_{car,top}$	1	on	on	off	off	$0.5 \cdot V_{dc,GEM}$
$m_x < v_{car,bot}$	-1	off	off	on	on	$-0.5 \cdot V_{dc,GEM}$
rest	0	off	on	on	off	0

[1] x = a,b,c
[2] $-1 \leq m \leq 1$

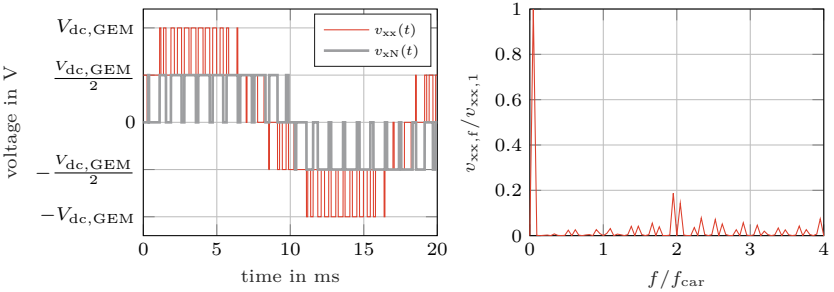

Figure 6.4: Waveform of the terminal voltage of a 3L-NPC converter in the time domain (left) and the frequency domain (right)

the sideband harmonic groups centered around the integer multiple of the carrier signals' frequency f_{car}. When applying the asymmetric regularly-sampled pulse-width modulation (PWM) with a zero-sequence voltage injection like shown in Fig. 6.3 [111], the harmonic groups centered at the twice of the carrier frequency will show the highest peak magnitude. This characteristic enables a reduction in the required filter size in contrast to the two-level voltage source converter (2L-VSC) converter topology with the same carrier frequency when a certain criteria on the voltage or current quality needs to be achieved via a passive filter. In case of 2L-VSC converters, the sideband harmonic groups centered at the carrier frequency will have the highest magnitude [111].

Interleaved Pulse-Width Modulation (PWM)

According to [111], the general form of the sideband harmonic component in the output voltage of a PWM-operated power-electronic converter can be written as follows

$$V_{\mathrm{h}}(t) = \sum_{m=1}^{\infty} \sum_{\substack{n=-\infty \\ n\neq 0}}^{\infty} [A_{\mathrm{mn}} \cos(m[\omega_{\mathrm{car}} t + \theta_{\mathrm{car}}] + n[\omega_1 t + \theta_1]) + B_{\mathrm{mn}} \sin(m[\omega_{\mathrm{car}} t + \theta_{\mathrm{car}}] + n[\omega_1 t + \theta_1])] \quad (6.1)$$

The interleaved switching of parallel-connected 3L-NPC converters are achieved by shifting the carrier signals between the participating converters. Thus, the phase of the carrier signals of converter i in (6.1) can be expressed as follows

$$\theta_{\mathrm{car,i}} = \theta_{\mathrm{car},1} + (i-1) \cdot {}^{2\pi}/_{n_{\mathrm{conv}}} \text{ in rad} \quad (6.2)$$

where n_{conv} is the number of the participating converters and i must be lower or equal than n_{conv}. Consequently, the sideband harmonics of the converters will cancel each other out except for $m = j \cdot n_{\mathrm{conv}}$ where j is an integer number. The interleaved PWM of two and three 3L-NPC converters are shown in Fig. 6.5. The resulting line-to-line voltage waveforms at the output terminals of the interleaved converter systems are displayed in Fig. 6.6.

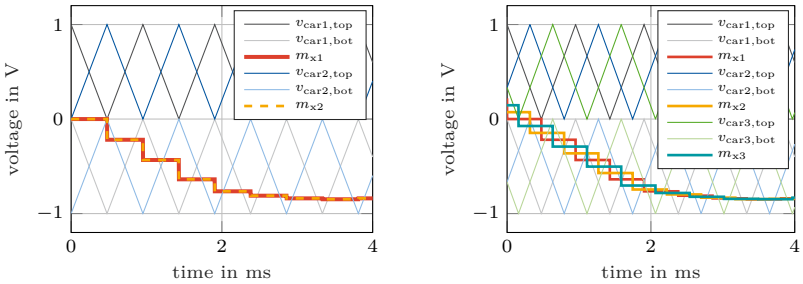

(a) two converters (b) three converters

Figure 6.5: Pulse-width modulation of interleaved-switched 3L-NPC converters

It can be seen in Fig. 6.5a that the carrier signals of the second converter in the two-converter setup are shifted by 180°. When the asymmetric regular sampling is applied, the voltage reference of both converters m_{x1} and m_{x2} are updated at the same time instants because the edges of the carrier signals of both converters occur at the same instants. As displayed in Fig. 6.6a, the sideband harmonics around

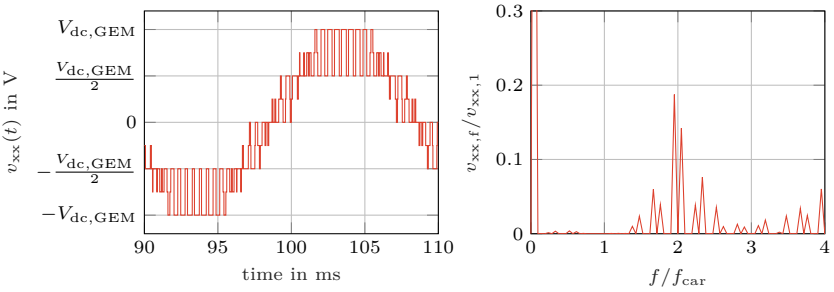

(a) two converters

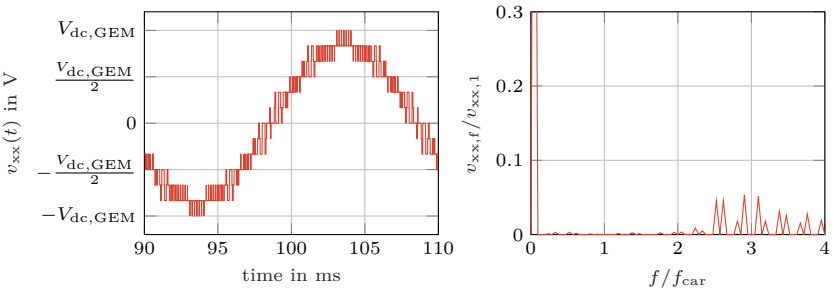

(b) three converters

Figure 6.6: Voltage waveform of interleaved 3L-NPC converters in the time domain (left) and the frequency domain (right)

the carrier frequency are eliminated with the interleaved PWM of two converters. Although the sideband harmonics around $3 \cdot f_{\mathrm{car}}$ should also be eliminated based on the above description, several harmonics around this frequency are still visible. These harmonics are from the sideband groups centered at twice and four times the carrier frequency. In the time domain, the improvement in the voltage quality via interleaved PWM can be identified from the increased number of the voltage levels in the waveform of the output voltage as displayed in Fig. 6.6a.

In terms of the quality of the output voltage, interleaving two 3L-NPC converters does not improve the voltage total harmonic distortion (THD) significantly as shown in Table 6.4. Only a slight improvement in the voltage THD is achieved with this setup compared to the single converter setup. This is because the sideband harmonics with the highest magnitude centered at twice the carrier

Table 6.4: Total harmonic distortion of interleaved 3L-NPC converters

	Number of converters		
	1	2	3
$\mathrm{THD_v}$	36%	32%	16%

frequency are not eliminated if only two converters are in operation. When three converters are operated with the interleaved PWM, these sideband harmonics are canceled out as depicted in Fig. 6.6b. Also, the sideband harmonics groups centered at $1 \cdot f_{\mathrm{car}}$ and $2 \cdot f_{\mathrm{car}}$ are no longer visible in the spectrum plot in the frequency domain. In contrast, the sideband harmonics centered at $3 \cdot f_{\mathrm{car}}$ with lower magnitudes remain. Therefore, the THD level of the output voltage are reduced substantially as shown in Table 6.4.

Regarding the update rate of the reference voltage, interleaving three 3L-NPC converters appears to be advantageous because the effective update rate of the reference voltage can be raised. Since the carrier signals of the participating converters are phase-shifted by 120° between each other as shown in Fig. 6.5b, the update time instants of the converters are interleaved as well. As a result, the converter controller may update the voltage reference signals m_{x} at three times the update rate of the single- or two-converter setup as briefly described in [112]. This is a very important feature namely when strict requirements on voltage dynamic, voltage quality and power come at the same time. Therefore, this thesis considers three 3L-NPC converters operated with interleaved PWM for the grid emulator. Because of these benefits, the wind turbine test bench at the Center for Wind Power Drives (CWD), RWTH Aachen University also applies this setup for its grid emulator.

6.2 Filter Design

Despite employing three 3L-NPC converters with the interleaved PWM, the THD of the output voltage still needs to be reduced to meet the requirement in Table 6.1. Hence, a filter unit is still necessary to further suppress the remaining voltage harmonics. Within this thesis, the filter configuration as shown in Fig. 6.2 is considered. The parameter tuning and the components selection of the filter are very straight forward which is elaborated in the following subsections.

6.2.1 System Modeling

Prior to the selection of the filter components, the equivalent model of the system needs to be derived taking the considered filter structure into account. The single-phase equivalent circuit of the converter system referred to the 3 kV windings is given in Fig. 6.7. Because the remaining sideband harmonics of the participating converters after applying the interleaved PWM are in phase, the three converters can be treated as one large converter having a line-to-line voltage waveform as depicted in Fig. 6.6b.

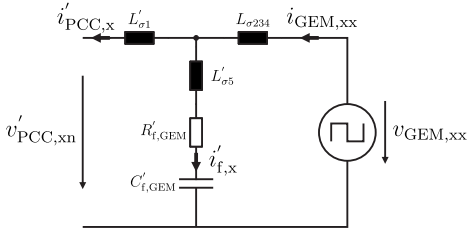

Figure 6.7: Single-phase equivalent circuit referred to the low-voltage (3 kV) windings

The inductance $L_{\sigma 1}$ and $L_{\sigma 5}$ denote the stray inductance of the 20 kV winding (PCC) and 6 kV winding (filter) respectively. The primed symbol indicates that the variables are referred to the 3 kV windings. The inductance $L_{\sigma 234}$ represents the combined stray inductances of the winding 2, 3 and 4, to which the converters are connected.

At no-load condition (DUT is disconnected), the transfer function from the converter's output voltage to the voltage at PCC can be written as follows:

$$G_{\mathrm{f,GEM}}(s) = \frac{\underline{V}'_{\mathrm{PCC,xn}}(s)}{\underline{V}_{\mathrm{GEM,xx}}(s)} = \frac{s^2 \cdot \left(\omega_{\mathrm{resL}}/\omega_{\mathrm{resH}}\right)^2 + s \cdot 2 \cdot \zeta \cdot \omega_{\mathrm{resL}} + \omega_{\mathrm{resL}}^2}{s^2 + s \cdot 2 \cdot \zeta \cdot \omega_{\mathrm{resL}} + \omega_{\mathrm{resL}}^2} \tag{6.3}$$

where ω_{resL} and ω_{resH} are the resonance frequencies and ζ is the damping factor of the system described as follows:

$$\omega_{\mathrm{resL}} = \frac{1}{\sqrt{(L'_{\sigma 5} + L_{\sigma 234}) \cdot C'_{\mathrm{f,GEM}}}}$$

$$\omega_{\mathrm{resH}} = \frac{1}{\sqrt{L'_{\sigma 5} \cdot C'_{\mathrm{f,GEM}}}}$$

$$\zeta = \frac{1}{2} \cdot C'_{\mathrm{f,GEM}} \cdot R'_{\mathrm{f,GEM}} \cdot \omega_{\mathrm{resL}}$$

It must be noted that the modeling in Fig. 6.7 considers the transformer transfer characteristic between the phase windings in order to avoid confusion due to the different winding configurations. Thus, the line-to-line voltage $\underline{V}_{\mathrm{GEM,xx}}$ is taken for the converter output voltage in (6.3). Also, the line to the neutral point $\underline{V}'_{\mathrm{PCC,xn}}$ is taken into account for the voltage on the PCC side. The response of the transfer function $G_{\mathrm{f,GEM}}(s)$ is graphically presented in Fig. 6.8 for various filter parameters.

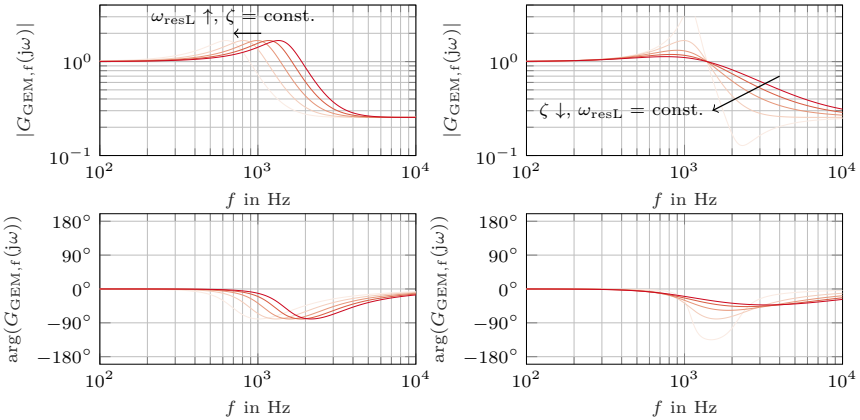

Figure 6.8: Response of the transfer function $G_{\mathrm{f,GEM}}(s)$ with various resonance frequencies and damping factors

It can be seen in Fig. 6.8, that due to the presence of the capacitor $C_{\mathrm{f,GEM}}$, the impedance of the filter branch is high for frequencies below f_{resL}. In contrast to the typical LC filter such as in [93], [103], [104], the filter attenuation is limited

Table 6.5: Stray inductances of the multi-winding transformer referred to the 3 kV windings

	$L'_{\sigma 1}$	$L'_{\sigma 5}$	$L_{\sigma 234}$
Values	690.8 µH	171.8 µH	599.7 µH

by the transformer stray inductance of the filter winding or winding 5. Therefore, the stray inductance to the filter winding shall be designed as low as possible to keep the attenuation at high frequencies low.

From Fig. 6.8, the trade-off in the selection of filter parameters can be identified. The presence of zero in $G_{\mathrm{f,GEM}}(s)$ is indicated by the deep attenuation in the right figure of Fig. 6.8. The zero can principally be utilized to suppress the most significant sideband harmonics that drive the THD value the most. On the other hand, the pole of $G_{\mathrm{f,GEM}}(s)$ is located near the zero which can amplify the sideband harmonics. If the damping factor is increased, the filter branch becomes more resistive such that the amplification caused by the pole is reduced. Consequently, the effect of the filter's zero is weakened which reduces the filter attenuation around the frequency of the zero.

In the next section, the parameter tuning will be discussed followed by the selection of the components taking this trade-off into account. The values of the stray inductances in Table 6.5 are considered for the selection of the filter parameters. These values were derived from the short-circuit test results of the installed multi-winding transformer on the wind turbine test bench at CWD.

6.2.2 Parameters Selection and Verification

The selection of the filter parameters is started by looking at their influence on the THD level of the PCC voltage. At first, the spectrum of the unfiltered PCC voltage in Fig. 6.6b is fed into the filter transfer function in (6.3) to determine the spectrum of the filtered PCC voltage. Afterwards, the THD level of the filtered PCC voltage is calculated by means of the THD equation in (5.9). The THD level of the filtered PCC voltage for various filter setups is accumulated in Fig. 6.9.

It can be seen that the lowest THD level is achieved when the damping factor ζ is low despite the high amplification caused by the filter's resonance. This because a lower ζ also means a better attenuation caused by the filter's zero. However, a lower ζ also means that the step response of the filter will have a

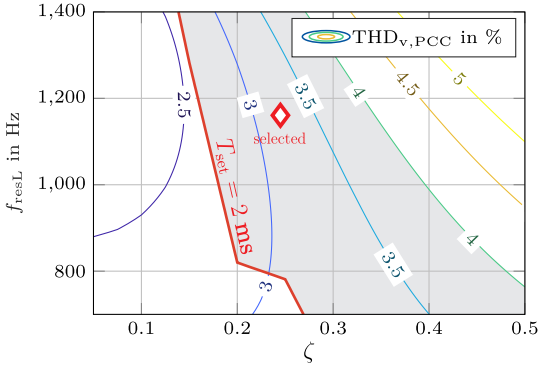

Figure 6.9: Voltage quality of the filtered PCC voltage depending on the filter parameters

heavier oscillation as depicted in Fig. 6.10a. As a consequence, the settling time of the output voltage with respect to an abrupt change in the reference signal T_{set} becomes longer. Therefore, the influence of the filter parameters in particular the filter resonance frequency f_{resL} and the damping factor ζ on the voltage settling time T_{set} is plotted in Fig. 6.10b. The settling time T_{set} is calculated from the starting point of the voltage change ($t = 0\,\mathrm{ms}$) until the last instance the voltage enters the tolerance band indicated by the grey area in Fig. 6.10b.

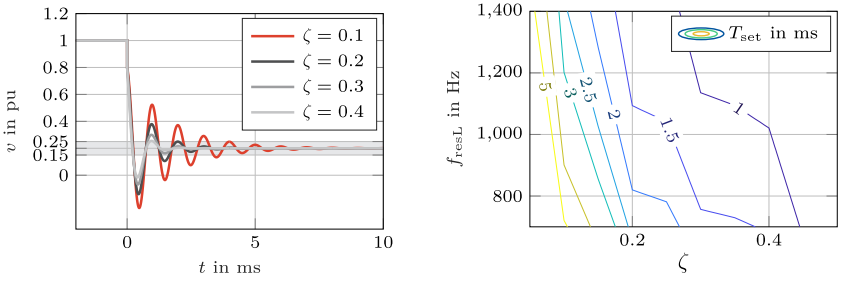

(a) Step response for various ζ to 0.2 pu

(b) Settling time map

Figure 6.10: Settling time T_{set} as a function of the filter parameters

As indicated in Fig. 6.10b, a lower damping factor leads to a large settling time T_{set} which may exceed the tolerated value of 2.5 ms. As a result, filter setups with

Table 6.6: Selected filter parameters

	$C_{\mathrm{f,GEM}}$	$C'_{\mathrm{f,GEM}}$ [1)]	$R_{\mathrm{f,GEM}}$	$R'_{\mathrm{f,GEM}}$ [1)]
Value	21 µF	28 µF	3.2 Ω	2.4 Ω

[1)] referred to the 3 kV windings

a too low damping factor cannot be taken despite of the low THD level of the PCC voltage. In Fig. 6.9, the filter setups that lead to a settling time T_{set} of 2 ms is plotted. With this, the filter setups that meet the design criteria in terms of the settling time and the voltage quality can be identified. Principally, all filter setups located in the grey area in Fig. 6.9 will fulfill these criteria. In contrast to the values in Table 6.1, $T_{\mathrm{set}} = 2\,\mathrm{ms}$ and $\mathrm{THD}_{\mathrm{v,PCC}} = 4\,\%$ are taken as limits in Fig. 6.9 in order to preserve a certain design margin.

For further discussions within this chapter, the setup indicated by the red diamond in Fig. 6.9 will be considered. This setup is also applied for the grid emulator of the wind turbine test bench at CWD. The component values of this setup are listed in Table 6.6. To verify the performance of the filter setup, the waveform of the PCC voltage obtained via a circuit simulation in PLECS [68] is plotted in Fig. 6.11a. As evident from this figure, the filter setup is able to suppress the sideband harmonics to achieve a PCC voltage with a low THD level ($< 5\,\%$). This is also confirmed via measurements on the CWD test bench as depicted in Fig. 6.11b.

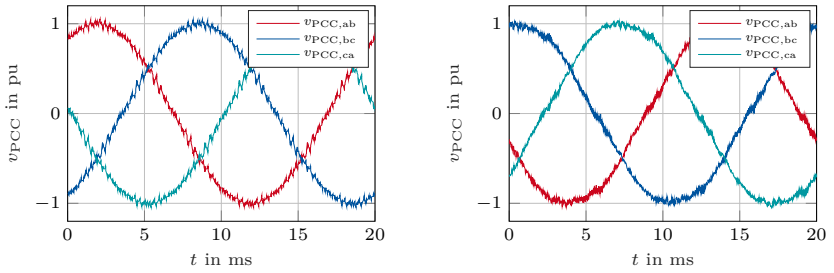

(a) Simulation, $\mathrm{THD}_{\mathrm{v,PCC}} = 3.2\%$ (b) Measurement, $\mathrm{THD}_{\mathrm{v,PCC}} = 3.2\%$

Figure 6.11: Waveforms of the PCC voltage from a simulation and a measurement

To confirm the performance of the selected filter setup with respect to the voltage

settling time when emulating a voltage dip, a simulation and a measurement of a voltage dip were performed. The results are displayed in Fig. 6.11 for the simulation and in Fig. 6.12 for the measurements. Next to the three-phase waveforms, the magnitude of the PCC voltage in an arbitrary synchronous reference frame is also given in these figures to obtain the voltage settling time T_{set}. From the simulation result, it is proven that the selected filter design enables a satisfactory settling time of lower than 2.5 ms. However, the voltage waveforms obtained from the measurement shows a significantly longer T_{set}. It seems that the voltage dynamic is limited by the converter controller although the selected filter setup allows a much higher dynamic. Because of this limitation, only the theoretical dynamic of the passive elements of the test bench will be taken into consideration for further analysis within this chapter. Nevertheless, the same steps can also be followed to conduct an analysis with a converter controller.

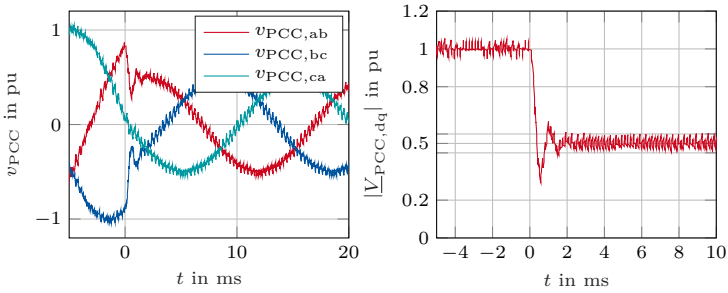

Figure 6.12: Simulated voltage dip with the selected filter setup under a no-load condition (DUT disconnected)

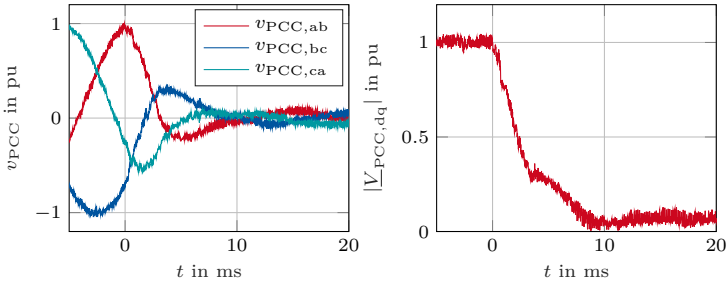

Figure 6.13: Measured voltage dip at the CWD wind turbine test bench under no-load condition (DUT disconnected)

6.3 Grid Impedance Emulation

6.3.1 Implementation

Beside operating in a power hardware-in-the-loop structure to mimic an electrical grid [9], the impedance of an electrical grid in Fig. 1.4a can be emulated using the converter controller. To accomplish this task, the concept with a proportional-resonance (PR) regulator as proposed in [93] can be employed. The complete structure of the grid impedance emulation is shown in Fig. 6.14.

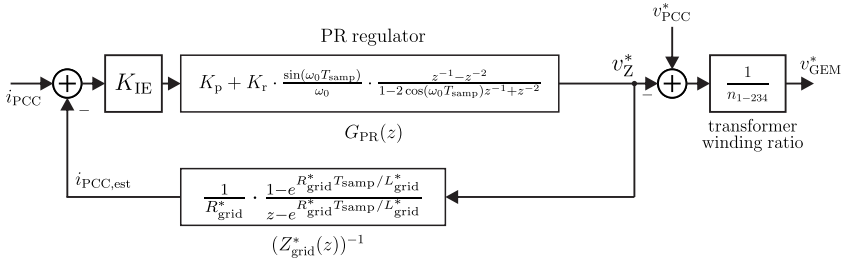

Figure 6.14: Grid impedance emulation algorithm on 20 kV side [93]

The concept works by estimating the PCC current $i_{\mathrm{PCC,est}}$ using a model of the desired grid impedance Z^*_{grid}. The estimated PCC current is then compared with the measured one and the error is regulated to zero by the PR regulator. The output of the PR regulator v^*_{Z} will represent the voltage drop across the emulated grid impedance:

$$\underline{V}^*_{\mathrm{Z}} = Z_{\mathrm{IE}}(z) \cdot \underline{I}_{\mathrm{PCC}} = \frac{K_{\mathrm{IE}} \cdot G_{\mathrm{PR}}(z)}{1 + K_{\mathrm{IEC}} \cdot G_{\mathrm{PR}}(z) \cdot {}^{1}/_{Z^*_{\mathrm{grid}}(z)}} \cdot \underline{I}_{\mathrm{PCC}} \tag{6.4}$$

The parameter of the PR regulator K_{p} and K_{r} can be determined by means of the following equations [93]:

$$K_{\mathrm{p}} = \sqrt{\left({}^{L^*_{\mathrm{grid}}}/_{T_{\mathrm{samp}}}\right)^2 + (R^*_{\mathrm{grid}})^2} \tag{6.5}$$

$$K_{\mathrm{r}} = 0.1 \cdot {}^{K_{\mathrm{P}}}/_{T_{\mathrm{samp}}} \tag{6.6}$$

where T_{samp} denotes the sampling period of the controller. In case of three interleaved converters applying the asymmetric regular sampling PWM, T_{samp} equals one sixth of the period of the carrier signals.

In [93], a certain value was selected for the gain K_{IE}. However, this value must be carefully determined in relation with the DUT. If the gain K_{IE} is too high, the coupled system will become unstable. On the other hand, with a lower gain the frequency coverage of the emulated grid impedance becomes more restricted as shown in Fig. 6.15. This issue will be elaborated further in the next section.

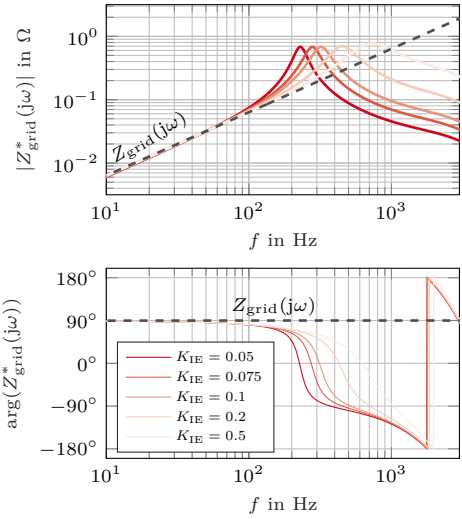

Figure 6.15: Frequency coverage of the grid impedance emulation for various gain K_{IE}

6.3.2 Stability Assessment at PCC

Stability Analysis

To analytically evaluate the system stability at PCC, the DUT and the grid emulator are redrawn as in Fig. 6.16. Z_{DUT} and Z_{GEM} are the impedance of the DUT and the grid emulator when measured at the PCC.

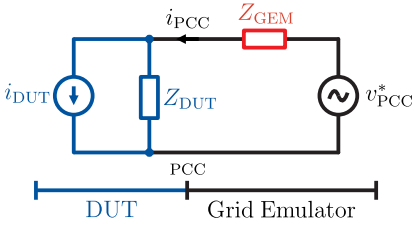

Figure 6.16: System equivalent circuit at PCC to conduct an impedance-based stability analysis

Considering the stray impedance of the 20 kV winding $Z_{\sigma 1}(z)$, the response $G_{\mathrm{f,GEM}}(z)$ of the passive filter and the control delay z^{-1}, the grid emulator impedance can be expressed as follows:

$$Z_{\mathrm{GEM}}(z) = Z_{\sigma 1}(z) + Z_{\mathrm{IE}}(z) \cdot G_{\mathrm{f,GEM}}(z) \cdot z^{-1} \tag{6.7}$$

$Z_{\sigma 1}(z)$ and $G_{\mathrm{f,GEM}}(z)$ can be obtained by discretizing their continuous transfer function in laplace domain. The c2d function in MATLAB [67] can be used to perform this task.

On the DUT side, the influence of the current controller of the DUT is neglected for the sake of simplification. Considering the DUT in Fig. 4.1, the impedance of the DUT at PCC only consists of the stray impedance of its step-up transformer $Z_{\sigma}(z)$ and the shunt elements of its filter $Z_{\mathrm{p}}(z)$. Later on, it is shown via a circuit simulation that this assumption is accurate enough to predict the system stability. Thus, the DUT impedance at the PCC can be written as follows:

$$Z_{\mathrm{DUT}}(z) = Z_{\sigma}(z) + Z_{\mathrm{p}}(z) \tag{6.8}$$

Similarly, the impedance $Z_{\sigma}(z)$ and $Z_{\mathrm{p}}(z)$ in discrete domain can be obtained by discretizing their corresponding continuous transfer function in Fig. 4.1 by means of the c2d tool in MATLAB [67].

According to [113], the above described system is stable if ${}^{Z_{\mathrm{GEM}}(z)}/_{Z_{\mathrm{DUT}}(z)}$ satisfies the Nyquist stability criterion. To evaluate the system stability, the Nyquist diagram of ${}^{Z_{\mathrm{GEM}}(z)}/_{Z_{\mathrm{DUT}}(z)}$ is plotted in Fig. 6.17 for different values of gain K_{IE}.

For this plot, the DUT in Table 4.1 is taken into account.

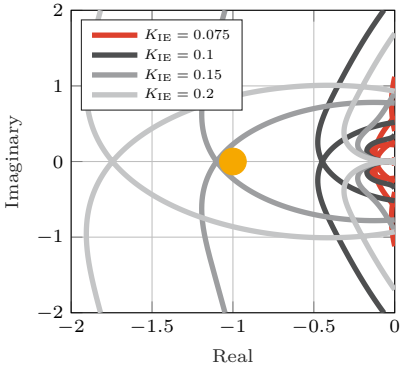

Figure 6.17: Nyquist plot of $Z_{GEM}(z)/Z_{DUT}(z)$ indicating the system stability

According to the Nyquist stability criterion, the system is unstable if the Nyquist plot of the function $Z_{GEM}(z)/Z_{DUT}(z)$ encircles the point (-1,0) marked by the orange circle in Fig. 6.17. This situation indicates an undamped resonance and must be avoided. As observed in the Nyquist plot in Fig. 6.17, the crossing point of the Nyquist curve is shifted to the left when the gain K_{IE} is enhanced. Starting from $K_{IE} > 0.15$ and beyond, the orange point starts to be encircled by the Nyquist curve indicating that the system starts destabilizing. This stability issue is also confirmed by the time domain simulation results presented in Fig. 6.18.

In the simulation for Fig. 6.18, the DUT finishes the pre-charging process of its DC link and the DUT connects to the grid at $t = 0$ ms by closing a circuit breaker at PCC. However, the grid-side converter is not active yet in this moment. Thus, only its step-up transformer and the shunt filter elements are connected to the grid. As evident from Fig. 6.18, the occurring PCC voltage oscillation when $K_{IE} = 0.2$ is further amplified. This indicates that the system is unstable. Based on the Nyquist plot Fig. 6.17 and time-domain simulation results in Fig. 6.18, the system presents a sufficient stability margin when K_{IE} is set to 0.1. Therefore, this value is taken for further discussions.

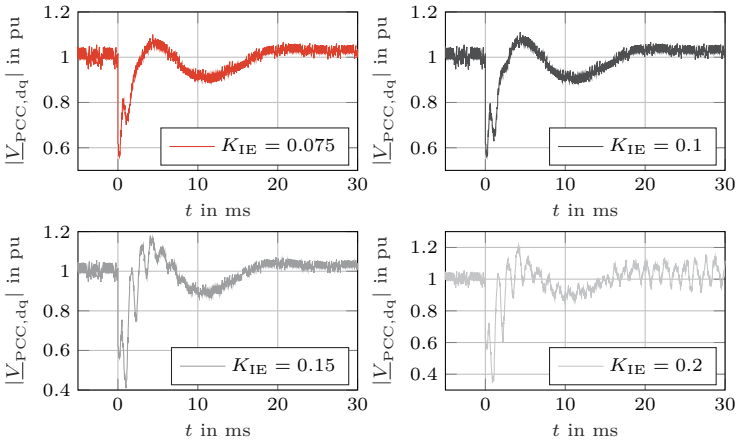

Figure 6.18: Time domain simulation for various gain K_{IE}

Stability with the Grid-Side Current Controller

So far, the grid-side current controller of the DUT was excluded. In order to confirm the validity of the stability analysis with the grid-side current controller of the DUT, a circuit simulation is performed with the grid-side current controller is activated 30 ms after the DUT connects to the grid. The simulation results are presented in Fig. 6.19.

As shown in Fig. 6.19, the active current controller does not impact the stability of the system. This is because the resonance between by the grid impedance emulation and the passive elements of the DUT occurs well beyond the bandwidth of the current controller. Therefore, the system stability can already be predicted with a sufficient accuracy by taking only the passive elements of the DUT into consideration. This is helpful namely because the information about the controller of the DUT is typically very limited. In contrast, the information about the passive elements is often available, which can be utilized to tune the grid impedance emulation feature of the grid emulator to prevent a system instability.

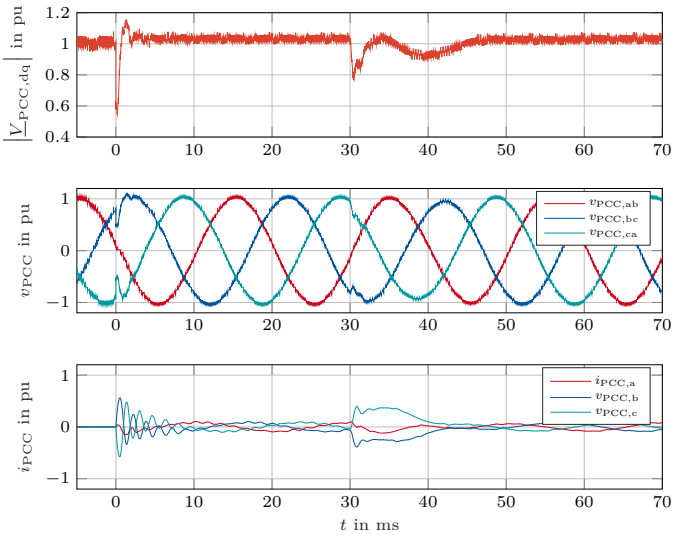

Figure 6.19: Time domain simulation of the grid impedance emulation with an active grid-side current controller of the DUT

6.3.3 Performance Evaluation

Within this section, the performance of the grid impedance emulation is evaluated in terms of the bandwidth of the impedance emulation as well as the dynamic response in the time domain. In order to identify the bandwidth of the grid emulation, the transfer characteristic of the current estimation $\underline{I}_{\mathrm{PCC,est}}/\underline{I}_{\mathrm{PCC}}$ is plotted in Fig. 6.20. The bandwidth of the current estimation is defined when its transfer characteristic curve falls below -3 dB.

According to this figure, the current estimation loop of the grid impedance emulation shows a bandwidth of almost 200 Hz. This means that the emulated grid impedance takes effect effectively only up to this frequency. This is also observable in Fig. 6.15 which compares the terminal impedance of the grid emulator at PCC with the desired grid impedance. For the selected gain K_{IE} of 0.1, the terminal impedance of the grid emulator shows a significant deviation to the desired impedance beyond this frequency. It must be noted that the bandwidth frequency of the current estimation must be subtracted with the fundamental frequency to be compared with the requirement discussed in Section 5.3. This is

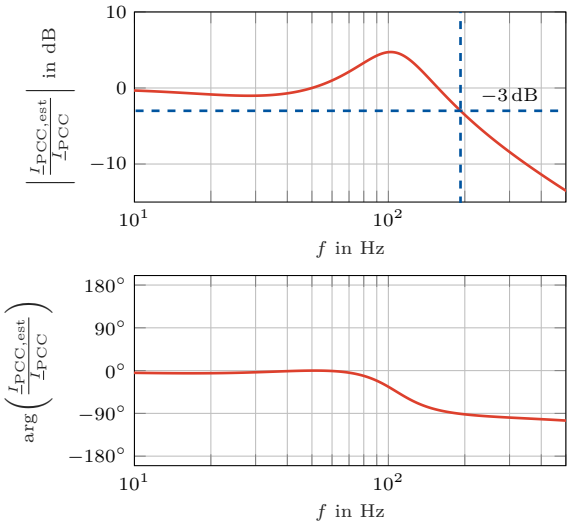

Figure 6.20: Bandwidth of the current estimation loop for the grid impedance emulation

because the low-pass filter used to estimate the bandwidth of the grid emulator is applied in a synchronous reference frame. Nevertheless, after subtracting with 50 Hz, the bandwidth of grid impedance emulation becomes about 150 Hz which is well beyond the required value of 20 Hz. Thus, the grid impedance emulation can be used to conduct flicker measurements.

In the time domain, the grid impedance emulation also shows a satisfactory performance as displayed by the simulation results in Fig. 6.21. In this simulation, at $t = 0$ ms the DUT abruptly changes its q-axis current responsible for the reactive power supply. As can be observed from Fig. 6.21, the response of the grid impedance emulation is satisfactory. When emulating a grid with a short-circuit power $S_{\mathrm{grid}} = 33$ pu (left figure), the grid impedance successfully sets the magnitude of the PCC voltage according to the desired grid impedance. When compared with a real grid impedance that consists of an inductive and a resistive part (red curve), a slight delay can be observed which shows the phase lag of the grid impedance emulation. Furthermore, a similar transient behavior of the grid-side converter current of the DUT can be observed even at a high grid impedance value or low grid's short-circuit power. Thereby, the grid emulator can also be used to observe the controller behavior under various grid impedances.

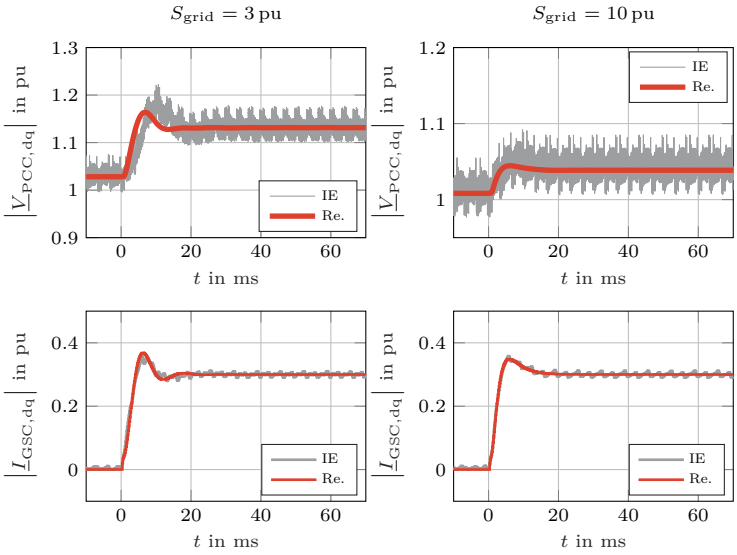

Figure 6.21: Simulations with a real grid impedance (Re.) and an emulated grid impedance (IE)

6.4 Coupled Operation with a Device Under Test

In this section, the coupled operation between the grid emulator and the device under test is evaluated. The evaluation emphasizes particularly if the expected behavior of the DUT with regards to the operation under a fluctuating output power and an occurrence of a voltage dip can be reproduced with the grid emulator.

6.4.1 Operation with a Power Fluctuation

For the operation with a power fluctuation, the output power waveform of the wind turbine in Fig. 2.4 is used to determine the d-axis current reference for the grid-side current controller of the DUT. The behavior of the resulting PCC voltage with a real grid and with a grid emulator is obtained via an electromagnetic transient simulation. In the simulation, the average model of the grid emulator is

used. In this model, the converter is modeled by a voltage source that represents the converter output voltage over a switching period. The simulation results with two different cases of a grid impedance are given in Fig. 6.22.

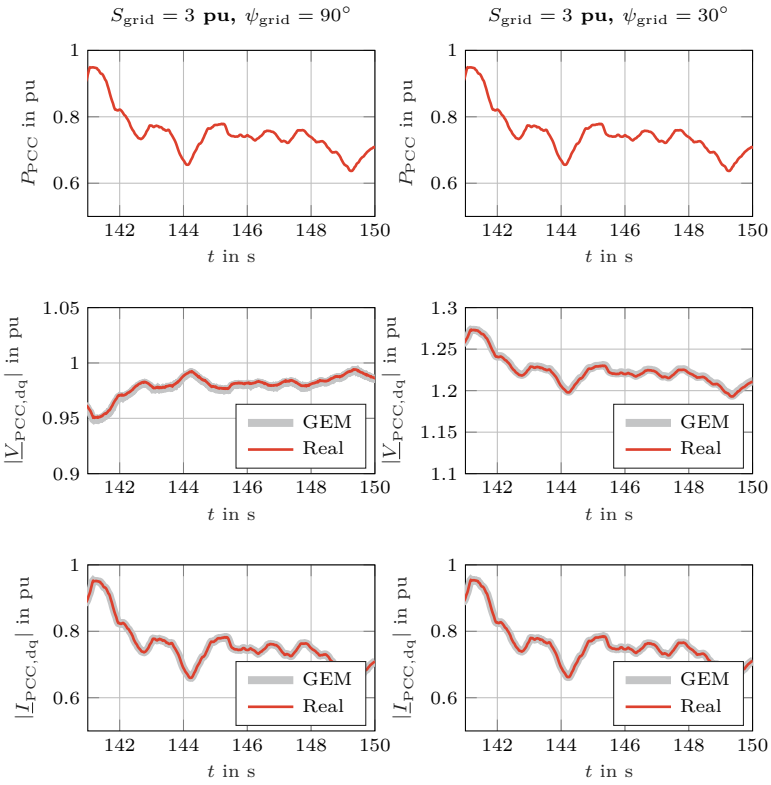

Figure 6.22: Grid emulator operation with a wind turbine operating at $\bar{V}_{\text{wind}} = 12\,\text{m/s}$ and $I_{\text{wind}} = 16\,\%$

As displayed in Fig. 6.22, the grid emulator is capable of emulating the behavior of a real grid even with a fluctuating output power of the DUT. The PCC voltage emulated by the grid emulator can follow the voltage of the real grid accurately. This shows that the grid emulator has a sufficient bandwidth to replicate a dynamic PCC voltage caused by a fluctuation of the wind turbine's output power. This simulation also confirms that the grid emulator concept can be applied to conduct flicker measurements. It must be noted that the converter voltage may

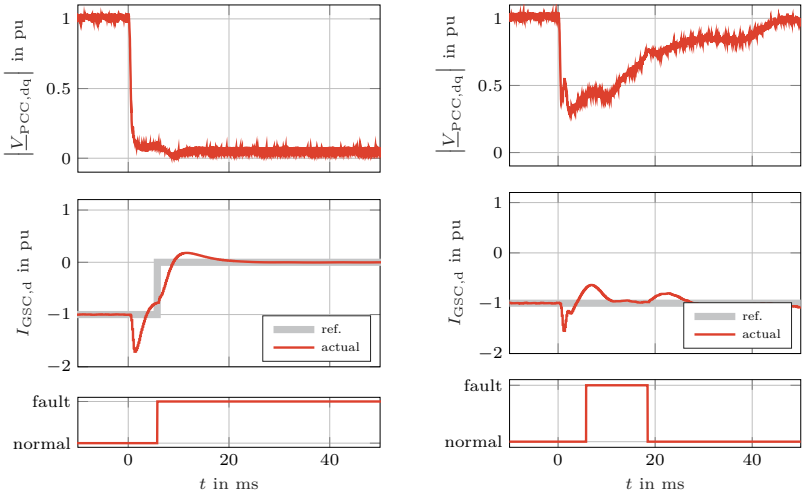

(a) Without grid impedance emulation

(b) With grid impedance emulation

Figure 6.23: Simulated LVRT test of a wind turbine with the considered grid emulator

enter an overmodulation ($m_{\mathrm{x}} > 1$) [111] when emulating a combination of a low short-circuit power and a low impedance angle ψ_{grid}. To solve this issue, the winding ratio of the multi-winding transformer shall be modified by using the available winding taps. Thereby, the nominal voltage of the low-voltage windings is reduced.

6.4.2 Low-Voltage Ride-Through Test

Lastly, the performance of the grid emulator in performing an LVRT test is evaluated via simulations in this section. Two different scenarios are simulated which represent 1 and scenario 2 in Chapter 4. For the scenario 1, the grid impedance emulation is deactivated. The resulting grid impedance during fault is 0.08 pu. In this case, the DUT must reduce its active current, if the residual voltage is 0.25 pu or lower before a loss of synchronization (LOS) occurs. For the scenario 2, the same grid impedance constellation as in Fig. 4.17b is considered. Prior to the fault, the DUT operates at its nominal power.

As observed in Fig. 6.23a, the DUT shows a similar behavior as in Fig. 4.17a. when a voltage dip with a residual voltage of 0.05 pu is emulated, the DUT is capable of correctly identifying the residual voltage thanks to the low grid impedance. Thus, the DUT correctly reduces its active power to prevent the LOS. In contrary, the DUT is not able to identify the residual voltage when a high grid impedance is emulated by the grid emulator. As a result, the DUT does not reduce its active power which leads to an instability and the DUT fails to perform the LVRT task. This shows the behavior of the DUT when a grid fault with the scenario 2 occurs as presented in Fig. 4.17b. Because the grid emulator is capable of correctly reproducing the behavior of the DUT during a grid fault, it can be concluded that the grid emulator can be applied to conduct the LVRT test.

6.5 Summary

Within this chapter, a grid emulator concept applying three interleaved MV 3L-NPC converters is analyzed systematically. Next to the selection of the number of converters, the determination of filter parameters is also presented. Furthermore, a systematic analysis and evaluation on a grid impedance emulation algorithm is presented, which is an essential element for wind turbine testing. From the conducted analysis and concept evaluation, it can be concluded that the grid emulator with the grid impedance emulation can be used to conduct flicker measurements as well as LVRT tests. The grid emulator concept fulfills the requirements in terms of voltage quality as well as the bandwidth for the grid impedance emulation. It is also found out that the stability of the coupled system can be well predicted only from the information on the passive elements of the DUT.

7 Conclusions and Future Work

7.1 Summary and Conclusion

This thesis presents a comprehensive analysis on the application of a grid emulator to conduct grid compliance tests of wind turbines. Firstly, the behavior of wind turbines in particular the output power fluctuation and the dynamic behavior is analyzed to draw a reference behavior for the evaluation of a grid emulator. Through this analysis, the design requirements for a grid emulator are derived from the DUT stand point. Additionally, this thesis presents an analysis on several standards and grid codes also to identify the design requirements for a grid emulator from the perspective of the regulatory framework. In the last part of the thesis, a multi-megawatt grid emulator concept for onshore wind turbines is evaluated with regard to its capability in performing flicker measurements and LVRT tests. The analysis is verified on simulation with the help of a simulation model of the reference nacelle developed at the Center for Wind Power Drives (CWD), RWTH Aachen University in Aachen, Germany.

Regarding the output power fluctuations that are responsible for the flicker phenomenon, it is found out that the wind turbulence and the tower shadowing effect are the main contributing factor to flicker. The contribution of the tower shadowing to flicker becomes relevant especially if the turbulence intensity is low. Therefore, in order to conduct flicker measurements on a test bench, the grid emulator must correctly emulate the grid voltage fluctuation caused by these two phenomenon. Although drivetrain resonances can cause power fluctuation when they are excited, this situation is typically prevented such that their contribution to flicker phenomenon is negligible.

In case of LVRT tests, the performance of the grid-side current controller is mainly dictated by the grid impedance. In this thesis, two grid fault scenarios are identified which can lead to a completely different behavior. Both scenarios differ mainly in the small-signal grid impedance during faults. It is identified that the risk of a controller instability is high when the grid impedance is large. Therefore, it is recommended that the test equipment must present a high grid impedance during grid faults in order to cover the worst case scenario.

From the regulatory frameworks, several design requirements can be derived, particularly the voltage quality, voltage dynamic and grid impedance. Nevertheless, a broad range of grid impedance is allowed in the standards and technical guidelines. Therefore, it is recommended to to consider the highest grid impedance at it presents the worst case scenario. Regarding the flicker measurements, it is found out that the simulation-based flicker measurement procedure may lead to a certain discrepancy in the results. Moreover, the flicker mitigation strategy embedded in the wind turbines cannot be fully validated using this way which makes the application of grid emulator very attractive.

From the analysis in the last part of this thesis, it can be concluded that the grid emulator concept employing three MV 3L-NPC converters can be used to conduct flicker measurements and LVRT tests. This concept is capable of meeting the strict requirements in terms of voltage quality, voltage dynamic and power demand. If the PR-regulator-based grid impedance emulation is employed, the grid emulator is capable of emulating grid impedance with a satisfactory bandwidth. It must be noted, that such a grid impedance emulation algorithm may interact with the device under test which can cause a stability issue. To prevent an instability, the gain of the PR regulator must be tuned in conjunction with the DUT. Nonetheless, considering only the passive components of the DUT when tuning the PR regulator still gives a good prediction on the stability limit of the system.

7.2 Future Work

Within the next steps, the grid emulator concept can be further evaluated with different types of DUT such as converters with an active damping for its LCL filters. In particular, the active damping for the LCL filter may present a major challenge in terms of the system stability. Not only during the operation, but also during the startup or shut down procedure where the control of the DUT is inactive but the filter components are connected to the grid. As a result, the system may be insufficiently damped. Besides, the evaluation with a doubly-fed generator wind turbine can be performed to verify the dynamic requirement derived in this thesis. Using a doubly-fed generator wind turbine is a good verification way since this wind turbine type is particularly sensitive to voltage dips.

Furthermore, the comparative analysis with field measurements need to be conducted in order to verify the behavior of the DUT obtained with a grid emulator. This is an important step for the introduction of grid emulators into the standards

for grid compliance and verification tests. However, this cannot be done with the reference wind turbine due to the missing rotor and the tower assembly.

Lastly, the operation in a power hardware-in-the-loop configuration with a real-time grid simulator can be investigated. The operation with a real-time grid simulator offers a much higher and a more realistic test scenario compared. Next to the stability in this setup, the limitations of the test setup need to be deeply evaluated to determine the plausible test cases.

A Appendix

A.1 Park and Clarke Transformation

Clarke Transformation

The transformation of a three-phase quantities onto a stationary reference frame is accomplished by means of a clarke transformation in (A.1) [114]. The graphical illustration of the vectors on a stationary reference frame is shown in Fig. A.1.

$$\begin{bmatrix} X_\alpha \\ X_\beta \end{bmatrix} = \begin{bmatrix} \frac{2}{3} & -\frac{1}{3} & -\frac{1}{3} \\ 0 & \frac{1}{\sqrt{3}} & -\frac{1}{\sqrt{3}} \end{bmatrix} \begin{bmatrix} X_\mathrm{a} \\ X_\mathrm{b} \\ X_\mathrm{c} \end{bmatrix} \tag{A.1}$$

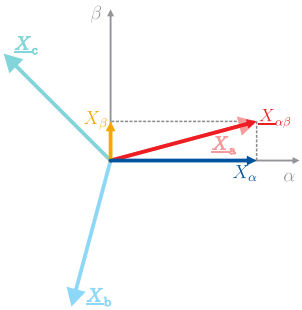

Figure A.1: Vectors on a stationary reference frame

Park Transformation

The transformation from the stationary reference frame on to a synchronous reference frame is accomplished by means of a park transformation in (A.2) [39]. The graphical illustration of the vectors on a synchronous reference frame is shown in Fig. A.2.

$$\begin{bmatrix} X_\mathrm{d} \\ X_\mathrm{q} \end{bmatrix} = \begin{bmatrix} \cos\theta_\mathrm{dq} & \sin\theta_\mathrm{dq} \\ -\sin\theta_\mathrm{dq} & \cos\theta_\mathrm{dq} \end{bmatrix} \begin{bmatrix} X_\alpha \\ X_\beta \end{bmatrix} \tag{A.2}$$

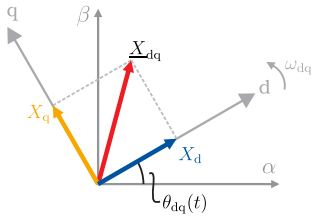

Figure A.2: Vectors on a synchronous reference frame

A.2 Electromagnetic Transient Simulation Model of the Wind Turbines

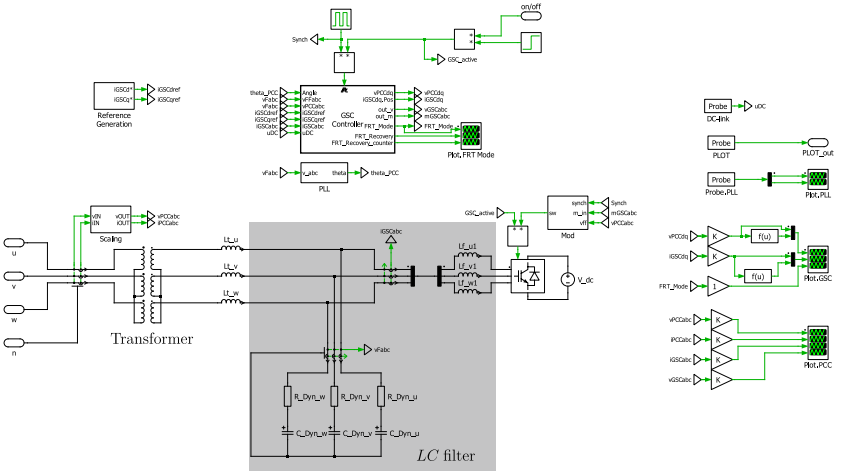

Figure A.3: Simulation model of the grid-side current controller

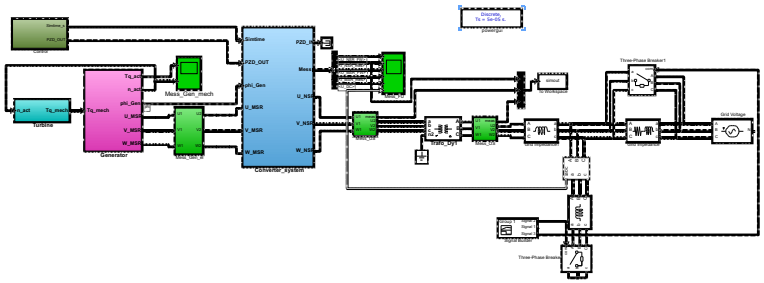

Figure A.4: Simulation model of the 2.75 MW reference nacelle

A.3 Symmetrical-Component Quantities according to IEC 61400-21

To calculate the symmetrical component quantities at the fundamental frequency, the Fourier coefficients of the voltage over a fundamental period T_1 needs to be obtained firstly

$$\begin{aligned} v_{\mathrm{x,cos}} &= \frac{2}{T_1}\int_{t-T_1}^{t} v_{\mathrm{x}}(t)\cos(\omega_{\mathrm{grid},1}\cdot t)dt \\ v_{\mathrm{x,sin}} &= \frac{2}{T_1}\int_{t-T_1}^{t} v_{\mathrm{x}}(t)\sin(\omega_{\mathrm{grid},1}\cdot t)dt \end{aligned} \tag{A.3}$$

where x indicates the phase a, b or c. Similar equation can be used to obtain the fourier coefficients of the fundamental component of the currents. The vector components of the fundamental positive-sequence voltage $V_{1+,\mathrm{cos}}$ and $V_{1+,\mathrm{sin}}$ are calculated using

$$\begin{aligned} V_{1+,\mathrm{cos}} &= \frac{1}{6}\left[2v_{\mathrm{a,cos}} - v_{\mathrm{b,cos}} - v_{\mathrm{c,cos}} - \sqrt{3}\,(v_{\mathrm{c,sin}} - v_{\mathrm{b,sin}})\right] \\ V_{1+,\mathrm{sin}} &= \frac{1}{6}\left[2v_{\mathrm{a,sin}} - v_{\mathrm{b,sin}} - v_{\mathrm{c,sin}} - \sqrt{3}\,(v_{\mathrm{c,cos}} - v_{\mathrm{b,cos}})\right] \end{aligned} \tag{A.4}$$

Whereby the vector components of the fundamental positive-sequence current $I_{1+,\mathrm{cos}}$ and $I_{1+,\mathrm{sin}}$ are obtained as follows

$$\begin{aligned} I_{1+,\mathrm{cos}} &= \frac{1}{6}\left[2i_{\mathrm{a,cos}} - i_{\mathrm{b,cos}} - i_{\mathrm{c,cos}} - \sqrt{3}\,(i_{\mathrm{c,sin}} - i_{\mathrm{b,sin}})\right] \\ I_{1+,\mathrm{sin}} &= \frac{1}{6}\left[2i_{\mathrm{a,sin}} - i_{\mathrm{b,sin}} - i_{\mathrm{c,sin}} - \sqrt{3}\,(i_{\mathrm{c,cos}} - i_{\mathrm{b,cos}})\right] \end{aligned} \tag{A.5}$$

Finally, the active part of the fundamental positive-sequence current can be calculated as follows

$$I_{\mathrm{a},1+} = \frac{P_{1+}}{\sqrt{3}\cdot U_{1+}} \tag{A.6}$$

where

$$\begin{aligned} P_{1+} &= \frac{3}{2}\left(V_{1+,\sin} I_{1+,\sin} + V_{1+,\cos} I_{1+,\cos}\right) \\ U_{1+} &= \sqrt{1.5\left(V_{1+,\sin}^2 + V_{1+,\cos}^2\right)} \end{aligned} \tag{A.7}$$

Meanwhile, the following equation applies for the reactive part of the fundamental positive-sequence current

$$I_{\mathrm{r},1+} = \frac{Q_{1+}}{\sqrt{3} \cdot U_{1+}} \tag{A.8}$$

where

$$Q_{1+} = \frac{3}{2}\left(V_{1+,\cos} I_{1+,\sin} - V_{1+,\sin} I_{1+,\cos}\right) \tag{A.9}$$

B Acronyms

2L-VSC	two-level voltage source converter
3L-NPC	three-level neutral-point clamped
AC	alternating current
AFE	active front-end
DC	direct current
DFG	doubly-fed generator
DUT	device under test
GSC	grid-side converter
HV	high voltage
HVRT	high-voltage ride-through
LOS	loss of synchronization
LPF	lowpass filter
LV	low voltage
LVRT	low-voltage ride-through
MSC	machine-side converter
MV	medium voltage
PCC	point of common coupling
PHiL	Power Hardware-in-the-Loop
PLL	phase-locked loop
PTP	Precision Time Protocol
PWM	pulse-width modulation
SFB	state feedback
THD	total harmonic distortion
VDD	voltage disturbance decoupling

VSC	voltage-source converter
WT	wind turbine

List of Figures

1.1 Schematic of a 4 MW nacelle test bench at CWD RWTH Aachen University . . . 1
1.2 Methods to apply voltage dips for wind turbines testing . . . 3
(a) Transformer-based method [15] . . . 3
(b) Shunt-impedance-based method [19]–[22] . . . 3
1.3 Topics coverage of the thesis . . . 6
1.4 Sign convention at PCC . . . 8
(a) Single-phase equivalent circuit diagram at PCC . . . 8
(b) Phasor diagram for diffferent cases of reactive power flow . . . 8

2.1 Power coefficient C_p for different tip-speed ratios λ and rotor blades pitch angle β in [29], [30] . . . 10
2.2 Drivetrain architectures variable-speed wind turbines in a multi-megawatt class [31], [33], [34] . . . 11
(a) Partial-scale converter concept . . . 11
(b) Full-scale converter concept . . . 11
2.3 Power-electronic converter and control architecture of a wind turbine with a full-scale converter [33], [36], [37] . . . 11
2.4 Typical control architecture of a variable-speed wind turbine [40] . . . 13
2.5 Derivation of a generator lookup table considering the aerodynamic characteristic in Fig. 2.1 . . . 14
(a) Power curve at $\beta = 0^\circ$ . . . 14
(b) Generator operation baseline . . . 14
(c) Baseline power curve . . . 14
2.6 Operation simulation of a wind turbine at a varying wind speed . . . 16
2.7 Operation baseline of the FVA nacelle . . . 19
(a) Measured generator operation points . . . 19
(b) Baseline power curve from datasheet . . . 19
2.8 FVA nacelle setup . . . 20
(a) Schematic . . . 20
(b) Final assembly on CWD test bench . . . 20
(c) Distributed data acquisition (DAQ) system architecture . . . 20

2.9 Measured operation behavior of the FVA nacelle under a low and high wind speed 21
(a) Average wind speed V_{wind}= 8 m/s 21
(b) Average wind speed V_{wind}= 20 m/s 21

3.1 PCC voltage deviation to its nominal value (ΔV_{PCC}) as a function of the fed-in power and the grid impedance. $Q_{\mathrm{PCC}} = 0$ pu 25
3.2 IEC flickermeter 26
(a) Flickermeter process chain 26
(b) Test voltage 26
(c) Response plot 26
3.3 Probability of instantaneous wind speed v_{wind} due to turbulence at V_{wind}= 16 m/s 28
3.4 Influence of tower shadowing on the instantaneous equivalent wind speed $v_{\mathrm{wind,eq}}$ 29
(a) Geometry of a wind turbine to calculate $v_{\mathrm{wind,ts}}$ 29
(b) Turbulence component in the equivalent wind speed $v_{\mathrm{wind,ts}}$. 29
3.5 Waveform approximation of torques and speed due to the tower shadowing effect 31
3.6 Power pulsation magnitude on the generator side of a wind turbine due to tower shadowing effect 32
3.7 Wind turbine simulation considering tower shadowing effect at an average wind speed of $V_{\mathrm{wind}} = 14$ m/s and 0 % turbulence intensity . 33
3.8 Wind turbine drivetrain representation as a three-rotating-mass model 34
(a) Three-mass model 34
(b) Drivetrain eigenfrequencies of various turbines [43], [44], [64]–[66] 34
3.9 Flicker severity level of the simulated wind turbine in Fig. 2.4 under turbulent wind conditions. $S_{\mathrm{grid}} = 3$ pu. 36
3.10 Simulated output power fluctuation of a wind turbine 36
3.11 Measured output power fluctuation of the 2.75 MW reference wind turbine nacelle 37
3.12 Flicker severity level of a 2.75 MW reference wind turbine nacelle . 37
3.13 Flicker severity level P_{st} without (red) and with (grey) tower shadowing effect at various wind speeds and turbulence intensity. . . . 38
3.14 Output power of the reference nacelle in frequency domain 39
3.15 Average output power of a wind turbine $\bar{P}_{\mathrm{pcc}}$ under various turbulence intensities 41
3.16 Power curve of the reference nacelle (grey) and the measured 10-minutes average power $\bar{P}_{\mathrm{pcc}}$ (red) for various V_{wind} and $I_{\mathrm{wind}} = 16$ % 41

4.1 Typical control architecture for the grid-side converter current i_{GSC} 45
4.2 Current control model in the s-domain 45
4.3 Plant and open-loop transfer function of the grid-side converter current controller $G_{\mathrm{ol}}(s_{\mathrm{dq}})$. $S_{\mathrm{grid}} = 3\,\mathrm{pu}$ and $\theta_{\mathrm{grid}} = 90^{\circ}$ 48
4.4 Plant and open-loop transfer function of the grid-side converter current controller $G_{\mathrm{ol}}(s_{\mathrm{dq}})$ with voltage disturbance decoupling. $S_{\mathrm{grid}} = 3\,\mathrm{pu}$ and $\theta_{\mathrm{grid}} = 90^{\circ}$ 49
4.5 Analytical model validation via circuit simulations in frequency domain 50
(a) Without disturbance decoupling 50
(b) With disturbance decoupling 50
4.6 Comparison of control performance parameters under various grid short-circuit power S_{grid} 51
(a) Without disturbance decoupling 51
(b) With disturbance decoupling 51
4.7 Step response simulation of the current controller at $S_{\mathrm{grid}} = 3\,\mathrm{pu}$. 52
(a) Without disturbance decoupling 52
(b) With disturbance decoupling 52
4.8 Sensitivity analysis of PI regulator parameters on the control performance for different S_{grid} 53
(a) Gain K_{p} 53
(b) Corner frequency ω_{PI} 53
4.9 Short-circuit fault scenarios 53
4.10 Grid fault scenarios and the simplified grid impedance model depending on the fault location 54
(a) Scenario 1 54
(b) Scenario 2 54
4.11 Behavior of current controller under different scenarios of a bolted grid fault ($R_{\mathrm{fault}} = 0$). $f_{\mathrm{samp}} = 2 \cdot f_{\mathrm{sw}}$ 57
4.12 Phase margin (PM) and bandwidth f_{bw} resulted from bolted grid faults for $f_{\mathrm{samp}} = 2 \cdot f_{\mathrm{sw}}$ 57
4.13 Behavior of current controller under different scenarios of a bolted grid fault ($R_{\mathrm{fault}} = 0$). $f_{\mathrm{samp}} = f_{\mathrm{sw}}$ 59
4.14 Phase margin (PW) and bandwidth f_{bw} resulted from bolted grid faults for $f_{\mathrm{samp}} = \cdot f_{\mathrm{sw}}$ 60
4.15 Phasor diagram during a grid fault under various I_{GSC} from low (left) to high (right) 62
4.16 Limit of active or d-axis current delivery during grid fault 63
4.17 Simulation of a grid-side converter indicating the loss of synchronization 64
(a) Fault scenario 1
$Z_{\mathrm{grid}} = 0.33\,\mathrm{pu}$, $Z_{\mathrm{grid,WT}} = 0\,\mathrm{pu}$ 64

(b) Fault scenario 2
$Z_{\text{grid}} = 0.08\,\text{pu}$, $Z_{\text{grid,WT}} = 0.27\,\text{pu}$ 64
4.18 Validation of the simulation model of the 2.75 MW reference nacelle with measurements 67
4.19 Response to an abrupt change in reactive or q-axis current reference at zero turbine power 68
4.20 Dynamic behavior of a 2.75 MW reference nacelle under two symmetrical short-circuit fault scenarios 70
4.21 Loss of synchronization under two short-circuit fault scenarios . . . 71

5.1 Static grid support 74
(a) Voltage support 74
(b) Frequency support 74
5.2 Dynamic grid support 75
(a) LVRT borderline 75
(b) Reactive current support 75
5.3 LVRT test voltage according to IEC 61400-21 77
(a) LVRT test voltage waveform 77
(b) Settling time T_{set} 77
5.4 Test voltage waveform for asymmetrical LVRT tests 79
5.5 Dynamic grid support 80
(a) HVRT borderline 80
(b) Reactive current support [94] 80
5.6 HVRT test equipment based on an inductive-capacitive voltage divider [95] 81
5.7 Voltage flicker measurement procedure according to IEC 61400-21 [24] 82
5.8 Phasor diagrams at fundamental frequency showing a discrepancy in the simulation-based flicker measurement method with a fictive grid 83
5.9 PCC voltage discrepancy resulted from the conventional flicker measurement method 85
(a) $|\underline{V}_{\text{PCC,mea}}| = 0.95\,\text{pu}$ 85
(b) $|\underline{V}_{\text{PCC,mea}}| = 1\,\text{pu}$ 85
(c) $|\underline{V}_{\text{PCC,mea}}| = 1.05\,\text{pu}$ 85
5.10 Validation of the dynamic requirement of for grid emulators in simulation 86
(a) Simulation structure 86
(b) Error in short-term flicker e_{Pst} as a function of the grid emulator voltage dynamic 86
5.11 Comparison of current harmonic limits in Germany and Denmark . 87

6.1 Various grid emulator topologies in several publications [4]–[7], [9], [10], [12], [101]–[106] 90
6.2 Topology of a grid emulator applying interleaved medium-voltage (MV) converters 91
6.3 Circuit topology and modulation strategy of a three-level neutral-point-clamped converter [110] 92
6.4 Waveform of the terminal voltage of a 3L-NPC converter in the time domain (left) and the frequency domain (right) 93
6.5 Pulse-width modulation of interleaved-switched 3L-NPC converters 94
(a) two converters 94
(b) three converters 94
6.6 Voltage waveform of interleaved 3L-NPC converters in the time domain (left) and the frequency domain (right) 95
(a) two converters 95
(b) three converters 95
6.7 Single-phase equivalent circuit referred to the low-voltage (3 kV) windings 97
6.8 Response of the transfer function $G_{\mathrm{f,GEM}}(s)$ with various resonance frequencies and damping factors 98
6.9 Voltage quality of the filtered PCC voltage depending on the filter parameters 100
6.10 Settling time T_{set} as a function of the filter parameters 100
(a) Step response for various ζ to 0.2 pu 100
(b) Settling time map 100
6.11 Waveforms of the PCC voltage from a simulation and a measurement 101
(a) Simulation, $\mathrm{THD}_{\mathrm{v,PCC}} = 3.2\%$ 101
(b) Measurement, $\mathrm{THD}_{\mathrm{v,PCC}} = 3.2\%$ 101
6.12 Simulated voltage dip with the selected filter setup under a no-load condition (DUT disconnected) 102
6.13 Measured voltage dip at the CWD wind turbine test bench under no-load condition (DUT disconnected) 102
6.14 Grid impedance emulation algorithm on 20 kV side [93] 103
6.15 Frequency coverage of the grid impedance emulation for various gain K_{IE} 104
6.16 System equivalent circuit at PCC to conduct an impedance-based stability analysis 105
6.17 Nyquist plot of $Z_{\mathrm{GEM}}(z)/Z_{\mathrm{DUT}}(z)$ indicating the system stability . . 106
6.18 Time domain simulation for various gain K_{IE} 107
6.19 Time domain simulation of the grid impedance emulation with an active grid-side current controller of the DUT 108
6.20 Bandwidth of the current estimation loop for the grid impedance emulation 109

6.21 Simulations with a real grid impedance (Re.) and an emulated grid impedance (IE) 110
6.22 Grid emulator operation with a wind turbine operating at $\bar{V}_{\mathrm{wind}} = 12\,{}^{\mathrm{m}}/_{\mathrm{s}}$ and $I_{\mathrm{wind}} = 16\,\%$ 111
6.23 Simulated LVRT test of a wind turbine with the considered grid emulator 112
(a) Without grid impedance emulation 112
(b) With grid impedance emulation 112

A.1 Vectors on a stationary reference frame 120
A.2 Vectors on a synchronous reference frame 121

List of Tables

2.1 Nominal values of the FVA nacelle 18

4.1 Parameter of the baseline grid-side converter 44
4.2 Simulation parameters for the fault scenario 1 56
4.3 Settling time of the positive sequence reactive current under the fault scenario 1 60
4.4 Simulation parameters for the analysis of the dynamic behavior of the reference nacelle 69
4.5 Settling time of the positive-sequence reactive current $I_{\mathrm{PCC,r}}$ under a short-circuit fault 69

5.1 Settling time of the instantaneous PCC voltage for LVRT tests . . 77
5.2 Flicker severity limits in European grid codes 81
5.3 Comparison of $\mathrm{THD}_{\mathrm{v,PCC}}$ between various standards 88

6.1 Specification of the considered grid emulator 89
6.2 Technical data of the grid emulator 92
6.3 Phase leg switching states of a 3L-NPC converter 93
6.4 Total harmonic distortion of interleaved 3L-NPC converters 96
6.5 Stray inductances of the multi-winding transformer referred to the 3 kV windings 99
6.6 Selected filter parameters 101

Bibliography

[1] WindEurope, *Wind in power: 2016 European statistics*, WindEurope, Ed.

[2] J. B. Jensen, "Wind Turbine Testing System," US20090107256 A1, 2009.

[3] ——, "Test Bench And A Method For Testing Wind Turbine Equipment," US20090107255 A1, 2009.

[4] C. Saniter and J. Janning, "Test Bench for Grid Code Simulations for Multi-MW Wind Turbines, Design and Control," *IEEE Transactions on Power Electronics*, vol. 23, no. 4, pp. 1707–1715, 2008.

[5] C. Mehler, T. Jersch, P. Koralewicz, and B. Tegtmeier, "Advanced grid simulator topology for testing of renewable energy supply units especially wind energy converters (WECs) under laboratory conditions," in *2016 18th European Conference on Power Electronics and Applications (EPE'16 ECCE Europe)*, pp. 1–9.

[6] P. Koralewicz, V. Gevorgian, R. Wallen, W. van der Merwe, and P. Jorg, "Advanced grid simulator for multi-megawatt power converter testing and certification," in *2016 IEEE Energy Conversion Congress and Exposition (ECCE)*, pp. 1–8.

[7] J. C. Fox and B. Gislason, "Introduction to the Clemson University 15 MW Hardware-In-the-Loop Grid Simulator," in *2014 Clemson University Power Systems Conference*, 2014, pp. 1–5.

[8] D. Bosse, D. Radner, R. Schelenz, and G. Jacobs, "Analysis and Application of Hardware in the Loop Wind Loads for Full Scale Nacelle Ground Testing," in *DEWI Magazin*, DEWI, Ed., vol. 43, 2013, pp. 65–70.

[9] A. Helmedag, T. Isermann, A. Monti, N. R. Averous, M. Stieneker, and R. W. de Doncker, "Multi-physics power hardware in the loop test bench for on-shore wind turbine nacelles," in *2013 IEEE ECCE Asia Downunder*, IEEE, 2013, pp. 221–226.

[10] A. Helmedag, T. Isermann, U. Jassmann, D. Radner, D. Abel, G. Jacobs, and A. Monti, "Testing nacelles of wind turbines with a hardware in the loop test bench," *IEEE Instrumentation & Measurement Magazine*, vol. 17, no. 5, pp. 26–33, 2014.

[11] A. Helmedag, "System level multi-physics power hardware in the loop testing for wind energy converters," Dissertation, RWTH Aachen University, Aachen, 2015.

[12] N. R. Averous, M. Stieneker, S. Kock, A. Cristian, A. Helmedag, R. W. de Doncker, G. Jacobs, K. Hameyer, and A. Monti, "Development of a 4 MW Full-Size Wind-Turbine Test Bench," *IEEE Journal of Emerging and Selected Topics in Power Electronics*, p. 1, 2017.

[13] Uwe Jassmann, Matthias Reiter, and Dirk Abel, "Driving Torque Control for a Nacelle Test Bench," *Journal of Physics: Conference Series*, vol. 524, no. 1, p. 012 068, 2014.

[14] U. Jassmann, M. Hakenberg, and D. Abel, "An extended inertia and eigenfrequency emulation for full-scale wind turbine nacelle test benches," in *2015 IEEE International Conference on Advanced Intelligent Mechatronics (AIM)*, 2015, pp. 996–1001.

[15] A. Kramer and J. Ruff, "Transformers for phase angle regulation considering the selection of on-load tap-changers," *IEEE Transactions on Power Delivery*, vol. 13, no. 2, pp. 518–525, 1998.

[16] Y. Ma and G. G. Karady, "A single-phase voltage sag generator for testing electrical equipments," in *2008 IEEE/PES Transmission and Distribution Conference and Exposition*, pp. 1–5.

[17] C. Wessels, R. Lohde, and F. W. Fuchs, "Transformer based voltage sag generator to perform LVRT and HVRT tests in the laboratory," in *2010 14th International Power Electronics and Motion Control Conference (EPE/PEMC 2010)*.

[18] S. P. Engel, "Thyristor-based high-power on-load tap changers," Dissertation, RWTH Aachen and Shaker Verlag GmbH, 2016.

[19] J. C. Ausin, D. N. Gevers, and B. Andresen, "Fault ride-through capability test unit for wind turbines," *Wind Energy*, vol. 11, no. 1, pp. 3–12, 2008.

[20] M. García-Gracia, M. Paz Comech, J. Sallán, D. López-Andía, and O. Alonso, "Voltage dip generator for wind energy systems up to 5MW," *Applied Energy*, vol. 86, no. 4, pp. 565–574, 2009.

[21] Y. Yang, F. Blaabjerg, and Z. Zou, "Benchmarking of Voltage Sag Generators," in *IECON 2012 - 38th Annual Conference of IEEE Industrial Electronics*, pp. 943–948.

[22] J. Dirksen, "LVRT: Low Voltage Ride-Through," in *DEWI Magazin*, DEWI, Ed., vol. 43, 2013, pp. 56–60.

[23] FGW e.V., *Teil 3: Bestimmung der elektrischen Eigenschaften von Erzeugungseinheiten und -anlagen am Mittel-, Hoch- und Höchstspannungsnetz*, FGW e.V., Ed., 2016-03.

[24] IEC, *IEC 61400-21 - Wind turbines – Part 21: Measurement and assessment of power quality characteristics of grid connected wind turbines*, 2008.

[25] M. H. J. Bollen, "Voltage Sags in Three-Phase Systems," *IEEE Power Engineering Review*, vol. 21, no. 9, pp. 8–15, 2001.

[26] IEEE, *IEEE 1547-2018 - IEEE Standard for Interconnection and Interoperability of Distributed Energy Resources with Associated Electric Power Systems Interfaces*, 2018.

[27] IEC, *IEC 61850-7-420:2009 - Communication networks and systems for power utility automation - Part 7-420: Basic communication structure - Distributed energy resources logical nodes*, 2009.

[28] S. Heier, *Windkraftanlagen: Systemauslegung, Netzintegration und Regelung*, 4., überarbeitete und aktualisierte Auflage. Wiesbaden and s.l.: Vieweg+Teubner Verlag, 2005.

[29] O. Wasynczuk, D. Man, and J. Sullivan, "Dynamic Behavior of a Class of Wind Turbine Generators During Randon Wind Fluctuations," *IEEE Transactions on Power Apparatus and Systems*, vol. PAS-100, no. 6, pp. 2837–2845, 1981.

[30] P. Anderson and A. Bose, "Stability Simulation Of Wind Turbine Systems," *IEEE Transactions on Power Apparatus and Systems*, vol. PAS-102, no. 12, pp. 3791–3795, 1983.

[31] S. Muller, M. Deicke, and R. W. D. Doncker, "Doubly fed induction generator systems for wind turbines," *IEEE Industry Applications Magazine*, vol. 8, no. 3, pp. 26–33, 2002.

[32] G. Abad, J. Lopez, M. Rodriguez, L. Marroyo, and G. Iwanski, *Doubly fed induction machine: Modeling and control for wind energy generation applications*, ser. IEEE Press series on power engineering. Oxford: Wiley-Blackwell, 2011, vol. 84.

[33] F. Blaabjerg, M. Liserre, and K. Ma, "Power Electronics Converters for Wind Turbine Systems," *IEEE Transactions on Industry Applications*, vol. 48, no. 2, pp. 708–719, 2012.

[34] Z. Chen, J. M. Guerrero, and F. Blaabjerg, "A Review of the State of the Art of Power Electronics for Wind Turbines," *IEEE Transactions on Power Electronics*, vol. 24, no. 8, pp. 1859–1875, 2009.

[35] C. Vázquez Hernández, T. Telsnig, and A. Villalba Pradas, *JRC Wind Energy Status Report - 2016 Edition*, Publications Office of the European Union, Ed., Luxembourg, 2017.

[36] F. Blaabjerg, R. Teodorescu, M. Liserre, and A. V. Timbus, "Overview of Control and Grid Synchronization for Distributed Power Generation Systems," *IEEE Transactions on Industrial Electronics*, vol. 53, no. 5, pp. 1398–1409, 2006.

[37] F. Blaabjerg and K. Ma, "Future on Power Electronics for Wind Turbine Systems," *IEEE Journal of Emerging and Selected Topics in Power Electronics*, vol. 1, no. 3, pp. 139–152, 2013.

[38] R. de Doncker, D. W. Pulle, and A. Veltman, *Advanced Electrical Drives*. Dordrecht: Springer Netherlands, 2011.

[39] R. H. Park, "Two-reaction theory of synchronous machines generalized method of analysis-part I," *Transactions of the American Institute of Electrical Engineers*, vol. 48, no. 3, pp. 716–727, 1929.

[40] J. Jonkman, S. Butterfield, W. Musial, and G. Scott, *Definition of a 5-MW Reference Wind Turbine for Offshore System Development*. 2009.

[41] M. Marnett, S. Wellenberg, and W. Schröder, "Real-time simulation of aeroelastic rotor loads for horizontal axis wind turbines," *Journal of Physics: Conference Series*, vol. 524, p. 012 071, 2014.

[42] S. Reisch, G. Jacobs, D. Bosse, C. Leisten, U. Jassmann, and D. Abel, "FVA-Gondel: Aufbau und Betrieb der generischen Forschungs-WEA FVA 730 I," in *FVA-Informationstagung : 29. und 30. November 2017 in Würzburg / Forschungsvereinigung Antriebstechnik e.V*, Frankfurt: FVA, Forschungsvereinigung Antriebstechnik e.V, 2017.

[43] C. Leisten, U. Jassmann, J. Balshüsemann, and D. Abel, "Model Predictive Speed Control of a Wind Turbine System Test Bench," *IFAC-PapersOnLine*, vol. 51, no. 32, pp. 349–354, 2018.

[44] C. Leisten, L. Kavenl, U. Jassmann, and D. Abel, "Model Predictive Torque Control of a Wind Turbine System Test Bench in Hardware-in-the-Loop Operation," in *2019 18th European Control Conference (ECC)*, pp. 633–638.

[45] NEG Micon A/S, Ed., *Technical description NM80/2750: TSD 4000031'01*. 2003.

[46] N. R. Averous, A. Berthold, A. Schneider, F. Schwimmbeck, A. Monti, and R. W. de Doncker, "Performance tests of a power-electronics converter for multi-megawatt wind turbines using a grid emulator," *Journal of Physics: Conference Series*, vol. 753, p. 072 015, 2016.

[47] International Electrotechnical Commission, *Industrial communication networks - Fieldbus specifications*, 2019-04-10.

[48] *IEEE Standard for a Precision Clock Synchronization Protocol for Networked Measurement and Control Systems*, Piscataway, NJ, USA, 2008.

[49] *Electromagnetic compatibility (EMC): Part 3-3: Limits – Limitation of voltage changes, voltage fluctuations and flicker in public low-voltage supply systems, for equipment with rated current $\leq$ 16 A per phase and not subject to conditional connection*, Edition 3.0, ser. International standard Norme internationale. Geneva: International Electrotechnical Commission, 2013, vol. IEC 61000-3-3.

[50] D. DiLaura, *The lighting handbook: Reference and application*, 10. ed. New York, NY: Illuminating Engineering Society of North America, 2011.

[51] IEC, *IEC 61000 - Electromagnetic compatibility (EMC) - Part 4-15: Testing and measurement techniques - Flickermeter - Functional and design specifications*, 2010-08-24.

[52] J. Ruiz, J. J. Gutierrez, A. Lazkano, and S. Ruiz de Gauna, "A Review of Flicker Severity Assessment by the IEC Flickermeter," *IEEE Transactions on Instrumentation and Measurement*, vol. 59, no. 8, pp. 2037–2047, 2010.

[53] H. de Lange Dzn, "Eye's Response at Flicker Fusion to Square-Wave Modulation of a Test Field Surrounded by a Large Steady Field of Equal Mean Luminance," *Journal of the Optical Society of America*, vol. 51, no. 4, p. 415, 1961.

[54] J. Majchrzak and G. Wiczyński, "Basic Characteristics of IEC Flickermeter Processing," *Modelling and Simulation in Engineering*, vol. 2012, no. 4, pp. 1–9, 2012.

[55] Z. P. Goh, M. A. M. Radzi, H. Hizam, and N. I. Abdul Wahab, "Investigation of severity of voltage flicker caused by second harmonic," *IET Science, Measurement & Technology*, vol. 11, no. 3, pp. 363–370, 2017.

[56] P. Sørensen, A. D. Hansen, and P. A. C. Rosas, "Wind models for simulation of power fluctuations from wind farms," *Journal of Wind Engineering and Industrial Aerodynamics*, vol. 90, no. 12-15, pp. 1381–1402, 2002.

[57] P. Sørensen, N. A. Cutululis, A. Vigueras-Rodríguez, H. Madsen, P. Pinson, L. E. Jensen, J. Hjerrild, and M. Donovan, "Modelling of power fluctuations from large offshore wind farms," *Wind Energy*, vol. 11, no. 1, pp. 29–43, 2008.

[58] L. de Tommasi, M. Gibescu, and A. J. Brand, "A dynamic aggregate model for the simulation of short term power fluctuations," *Procedia Computer Science*, vol. 1, no. 1, pp. 269–278, 2010.

[59] S. Engström, H. Ganander, and R. Lindström, *Short Term Power Variations in the Output of Wind Turbines*, DEWI, Ed., 2001.

[60] D. Dolan and P. W. Lehn, "Simulation Model of Wind Turbine 3p Torque Oscillations due to Wind Shear and Tower Shadow," in *2006 IEEE PES Power Systems Conference and Exposition*, pp. 2050–2057.

[61] S. Das, N. Karnik, and S. Santoso, "Time-Domain Modeling of Tower Shadow and Wind Shear in Wind Turbines," *ISRN Renewable Energy*, vol. 2011, no. 1, pp. 1–11, 2011.

[62] D. Dolan and P. W. Lehn, "Simulation Model of Wind Turbine 3p Torque Oscillations due to Wind Shear and Tower Shadow," *IEEE Transactions on Energy Conversion*, vol. 21, no. 3, pp. 717–724, 2006.

[63] Weihao Hu, Zhe Chen, Yue Wang, and Zhaoan Wang, "Flicker Mitigation by Active Power Control of Variable-Speed Wind Turbines With Full-Scale Back-to-Back Power Converters," *IEEE Transactions on Energy Conversion*, vol. 24, no. 3, pp. 640–649, 2009.

[64] I. P. Girsang, J. S. Dhupia, E. Muljadi, M. Singh, and L. Y. Pao, "Gearbox and drivetrain models to study dynamic effects of modern wind turbines," in *2013 IEEE Energy Conversion Congress and Exposition (ECCE)*, pp. 874–881.

[65] C. Li, Y. Zhou, T. C. Lim, and G. Sun, "Dynamic responses of a wind turbine drivetrain under turbulent wind and voltage disturbance conditions," *Advances in Mechanical Engineering*, vol. 8, no. 5, p. 168 781 401 664 993, 2016.

[66] J. Kavil Kambrath, M. S. U. Khan, Y. Wang, A. I. Maswood, and Y.-J. Yoon, "A Novel Control Technique to Reduce the Effects of Torsional Interaction in Wind Turbine System," *IEEE Journal of Emerging and Selected Topics in Power Electronics*, vol. 7, no. 3, pp. 2090–2105, 2019.

[67] I. The MathWorks, *MATLAB*, url: www.mathworks.com.

[68] Plexim GmbH, *PLECS*, url: http://www.plexim.com.

[69] D. v. den Hoff, D. Cappel, A. Baseer, R. W. de Doncker, and R. Schelenz, "Simple Empiric Root-Mean-Square Electric-Drivetrain Model for Wind Turbines with Full-Size Converter," in *2019 IEEE Energy Conversion Congress and Exposition (ECCE)*, pp. 21–26.

[70] G. Romero, *Electrical Generation and Distribution Systems and Power Quality Disturbances*. InTech, 2011.

[71] J. Lopez, P. Sanchis, X. Roboam, and L. Marroyo, "Dynamic Behavior of the Doubly Fed Induction Generator During Three-Phase Voltage Dips," *IEEE Transactions on Energy Conversion*, vol. 22, no. 3, pp. 709–717, 2007.

[72] J. LÓpez, E. GubÍa, P. Sanchis, X. Roboam, and L. Marroyo, "Wind Turbines Based on Doubly Fed Induction Generator Under Asymmetrical Voltage Dips," *IEEE Transactions on Energy Conversion*, vol. 23, no. 1, pp. 321–330, 2008.

[73] N. R. Averous, H. Stagge, and R. W. de Doncker, "Performance characteristics of a doubly-fed generator on a test-rig with full-scale converter-based grid emulator," in *2014 IEEE Symposium on Power Electronics and Machines for Wind and Water Applications (PEMWA)*, pp. 1–8.

[74] J. Bielemeier, A. Frehn, A. Monti, R. Fruhmann, and F. Santjer, "Comparison of multi-megawatt LVRT testing setups for the certification of wind turbines," in *2019 IEEE Milan PowerTech*, pp. 1–6.

[75] Z. Ali, N. Christofides, L. Hadjidemetriou, E. Kyriakides, Y. Yang, and F. Blaabjerg, "Three-phase phase-locked loop synchronization algorithms for grid-connected renewable energy systems: A review," *Renewable and Sustainable Energy Reviews*, vol. 90, pp. 434–452, 2018.

[76] P. Rodriguez, R. Teodorescu, I. Candela, A. V. Timbus, M. Liserre, and F. Blaabjerg, "New Positive-sequence Voltage Detector for Grid Synchronization of Power Converters under Faulty Grid Conditions," in *37th IEEE Power Electronics Specialists Conference*, 18-22 June 2006, pp. 1–7.

[77] J. Shen, S. Schroder, H. Stagge, and R. W. de Doncker, "Precise modeling and analysis of DQ-frame current controller for high power converters with low pulse ratio," in *2012 IEEE Energy Conversion Congress and Exposition (ECCE)*, pp. 61–68.

[78] J. Shen, *Modeling methodologies for analysis and synthesis of controls and modulation schemes for high-power converters with low pulse ratios: Zugl.: Aachen, Techn. Hochsch., Diss., 2013*, 1. Aufl., ser. E.ON Energy Research Center PGS, Power Generation and Storage Systems. Aachen: E.ON Energy Research Center, 2013, vol. 17.

[79] H. A. B. Siddique, M. J. R. Ahmad, and R. W. de Doncker, "Optimal control and filter sizing of a multi-megawatt medium-voltage voltage-source converter for future grids," in *2016 IEEE 7th International Symposium on Power Electronics for Distributed Generation Systems (PEDG)*, pp. 1–8.

[80] E. Muljadi, C. P. Butterfield, A. Ellis, J. Mechenbier, J. Hochheimer, R. Young, N. Miller, R. Delmerico, R. Zavadil, and J. C. Smith, "Equivalencing the collector system of a large wind power plant," in *2006 IEEE Power Engineering Society General Meeting*, 9 pp.

[81] I. Erlich, F. Shewarega, S. Engelhardt, J. Kretschmann, J. Fortmann, and F. Koch, "Effect of wind turbine output current during faults on grid voltage and the transient stability of wind parks," in *Energy Society General Meeting (PES)*, pp. 1–8.

[82] O. Goksu, R. Teodorescu, C. L. Bak, F. Iov, and P. C. Kjaer, "Instability of Wind Turbine Converters During Current Injection to Low Voltage Grid Faults and PLL Frequency Based Stability Solution," *IEEE Transactions on Power Systems*, vol. 29, no. 4, pp. 1683–1691, 2014.

[83] FGW e.V., Ed., *Technische Richtlinien fuer Erzeugungseinheiten und -anlagen.*

[84] BDEW, *Richtlinie für Anschluss und Parallelbetrieb von Erzeugungsanlagen am Mittelspannungsnetz*, 2008.

[85] Energinet.dk, *Technical Regulations TF 3.2.6 Wind turbines connected to grids with voltages below 100 kV*, May 2004.

[86] ——, *Technical regulation 3.2.5 for wind power plants with a power output greater than 11 kW*, September 2010.

[87] National Grid Electricity Transmissions plc, *The Grid Code*, September 2016.

[88] Europäische Union, *Commission Regulation (EU) 2016/631 of 14 April 2016 establishing a network code on requirements for grid connection of generators (Text with EEA relevance)*, April 2016.

[89] Y. Fu, Y. Wang, and X. Zhang, "Integrated wind turbine controller with virtual inertia and primary frequency responses for grid dynamic frequency support," *IET Renewable Power Generation*, vol. 11, no. 8, pp. 1129–1137, 2017.

[90] J.-Y. Son and K. Ma, "Wind Energy Systems," *Proceedings of the IEEE*, vol. 105, no. 11, pp. 2116–2131, 2017.

[91] Bundesministerium der Justiz und fuer Verbraucherschutz, *Verordnung zu Systemdienstleistungen durch Windenergieanlagen: Systemdienstleistungsverordnung - SDL-WindV*, July 2009.

[92] N. R. Averous, M. Stieneker, and R. W. de Doncker, "Grid emulator requirements for a multi-megawatt wind turbine test-bench," in *2015 IEEE 11th International Conference on Power Electronics and Drive Systems*, IEEE, 2015, pp. 419–426.

[93] M. Biskoping, *Discrete modeling and control of a versatile power electronic test bench with special focus on central photovoltaic inverter testing.* RWTH Aachen University, 2019.

[94] VDE, *Technical requirements for the connection and operation of customer installations to the high-voltage network (TCC High-Voltage)*, 1.10.2015.

[95] Julian Langstädtler, *Testing Renewable Power Plants on High-Voltage-Ride-Through Capability: Grid Requirements and Testing Procedure*, 2017.

[96] T. Sun, *Power quality of grid-connected wind turbines with DFIG and their interaction with the grid.* Aalborg: Institute of Energy Tecnology, Aalborg University, 2004.

[97] Y. Hu, Z. Chen, W. Hu, and C. Su, "Mitigation of power system oscillation caused by wind power fluctuation," *IET Renewable Power Generation*, vol. 7, no. 6, pp. 639–651, 2013.

[98] G. S. Doman, J. M. Kos, K. I. Harner, E. D. DiValentin, and H. S. Healy, *Variable speed wind turbine*, 1987.

[99] R. D. Richardson and W. L. Erdman, *Variable speed wind turbine*, 1992.

[100] M. Lindholm and T. W. Rasmussen, "Harmonic analysis of doubly fed induction generators," in *The Fifth International Conference on Power Electronics and Drive Systems, 2003. PEDS 2003*, 17-20 Nov. 2003, pp. 837–841.

[101] R. Pöllänen, L. Kankainen, M. Pääkkönen, J. Ollila, and S. Strandberg, "Full-power converter based test bench for low voltage ride-through testing of wind turbine converters," in *Proceedings of the 2011 14th European Conference on Power Electronics and Applications*, 2011, pp. 1–10.

[102] R. Lohde and F. W. Fuchs, "Laboratory type PWM grid emulator for generating disturbed voltages for testing grid connected devices," in *2009 13th European Conference on Power Electronics and Applications*, 2009, pp. 1–9.

[103] M. Biskoping, S. Richter, and R. W. D. Doncker, "Inverter based testbench for photovoltaic inverters in compliance with medium-voltage grid codes," in *Renewable Energy Research and Applications (ICRERA), 2012 International Conference on*, 2012, pp. 1–6.

[104] N. Espinoza, "Wind turbine characterization by voltage source converter based test equipment," Dissertation, 2016.

[105] C. Saniter, J. Janning, and A. Bocquel, "Test bench for grid code simulations for multi-MW wind turbines," in *Power Electronics and Applications, 2007 European Conference on*, 2007, pp. 1–10.

[106] R. F. Schkoda and C. Fox, "Integration of mechanical and electrical hardware for testing full scale wind turbine nacelles," in *2014 Clemson University Power Systems Conference*, IEEE, 2014, pp. 1–8.

[107] N. R. Averous, A. Deshpande, and R. W. De Doncker, "Design and Performance Evaluation of a Grid Emulator Based on a 3L-NPC Converter," in *Conference for Wind Power Drives, CWD 2017, Aachen 7th-8th March*, A. T. Werkmeister, D. Abel, C. Brecher, R. W. de Doncker, K. Hameyer, G. Jacobs, A. Monti, and W. Schröder, Eds., Norderstedt: BoD - Books on Demand, 2017, pp. 133–144.

[108] TOSHIBA Corporation, *Press Pak IEGT Silicon N-Channel IEGT ST2100GXH24A*, 2016.

[109] Infineon Technologies Bipolar GmbH & Co. KG, *Technical Information Fast Hard Drive Diode D1301SH*, 2016.

[110] A. Nabae, I. Takahashi, and H. Akagi, "A New Neutral-Point-Clamped PWM Inverter," *IEEE Transactions on Industry Applications*, vol. IA-17, no. 5, pp. 518–523, 1981.

[111] D. G. Holmes and T. A. Lipo, *Pulse width modulation for power converters: Principles and practice*, ser. IEEE Press series on power engineering. Hoboken, New Jersey and Piscataway, New Jersey: Wiley-Interscience IEEE Press, 2003.

[112] S. Schroder, P. Tenca, T. Geyer, P. Soldi, L. J. Garces, R. Zhang, T. Toma, and P. Bordignon, "Modular High-Power Shunt-Interleaved Drive System: A Realization up to 35 MW for Oil and Gas Applications," *IEEE Transactions on Industry Applications*, vol. 46, no. 2, pp. 821–830, 2010.

[113] J. Sun, "Impedance-Based Stability Criterion for Grid-Connected Inverters," *IEEE Transactions on Power Electronics*, vol. 26, no. 11, pp. 3075–3078, 2011.

[114] Edith Clarke, "Problems Solve by Modified Symmetrical Components," in *General Electric Review*, vol. 41, pp. 11–12.

E.ON ERC Band 1
Streblow, R.
Thermal Sensation and Comfort Model for Inhomogeneous Indoor Environments
1. Auflage 2011
ISBN 978-3-942789-00-4

E.ON ERC Band 2
Naderi, A.
Multi-phase, multi-species reactive transport modeling as a tool for system analysis in geological carbon dioxide storage
1. Auflage 2011
ISBN 978-3-942789-01-1

E.ON ERC Band 3
Westner, G.
Four Essays related to Energy Economic Aspects of Combined Heat and Power Generation
1. Auflage 2012
ISBN 978-3-942789-02-8

E.ON ERC Band 4
Lohwasser, R.
Impact of Carbon Capture and Storage (CCS) on the European Electricity Market
1. Auflage 2012
ISBN 978-3-942789-03-5

E.ON ERC Band 5
Dick, C.
Multi-Resonant Converters as Photovoltaic Module-Integrated Maximum Power Point Tracker
1. Auflage 2012
ISBN 978-3-942789-04-2

E.ON ERC Band 6
Lenke, R.
A Contribution to the Design of Isolated DC-DC Converters for Utility Applications
1. Auflage 2012
ISBN 978-3-942789-05-9

E.ON ERC Band 7
Brännström, F.
Einsatz hybrider RANS-LES-Turbulenzmodelle in der Fahrzeugklimatisierung
1. Auflage 2012
ISBN 978-3-942789-06-6

E.ON ERC Band 8
Bragard, M.
The Integrated Emitter Turn-Off Thyristor - An Innovative MOS-Gated High-Power Device
1. Auflage 2012
ISBN 978-3-942789-07-3

E.ON ERC Band 9
Hoh, A.
Exergiebasierte Bewertung gebäudetechnischer Anlagen
1. Auflage 2013
ISBN 978-3-942789-08-0

E.ON ERC Band 10
Köllensperger, P.
The Internally Commutated Thyristor - Concept, Design and Application
1. Auflage 2013
ISBN 978-3-942789-09-7

E.ON ERC Band 11
Achtnicht, M.
Essays on Consumer Choices Relevant to Climate Change: Stated Preference Evidence from Germany
1. Auflage 2013
ISBN 978-3-942789-10-3

E.ON ERC Band 12
Panašková, J.
Olfaktorische Bewertung von Emissionen aus Bauprodukten
1. Auflage 2013
ISBN 978-3-942789-11-0

E.ON ERC Band 13
Vogt, C.
Optimization of Geothermal Energy Reservoir Modeling using Advanced Numerical Tools for Stochastic Parameter Estimation and Quantifying Uncertainties
1. Auflage 2013
ISBN 978-3-942789-12-7

E.ON ERC Band 14
Benigni, A.
Latency exploitation for parallelization of power systems simulation
1. Auflage 2013
ISBN 978-3-942789-13-4

E.ON ERC Band 15
Butschen, T.
Dual-ICT – A Clever Way to Unite Conduction and Switching Optimized Properties in a Single Wafer
1. Auflage 2013
ISBN 978-3-942789-14-1

E.ON ERC Band 16
Li, W.
Fault Detection and Protection inMedium Voltage DC Shipboard Power Systems
1. Auflage 2013
ISBN 978-3-942789-15-8

E.ON ERC Band 17
Shen, J.
Modeling Methodologies for Analysis and Synthesis of Controls and Modulation Schemes for High-Power Converters with Low Pulse Ratios
1. Auflage 2014
ISBN 978-3-942789-16-5

E.ON ERC Band 18
Flieger, B.
Innenraummodellierung einer Fahrzeugkabine in der Programmiersprache Modelica
1. Auflage 2014
ISBN 978-3-942789-17-2

E.ON ERC Band 19
Liu, J.
Measurement System and Technique for Future Active Distribution Grids
1. Auflage 2014
ISBN 978-3-942789-18-9

E.ON ERC Band 20
Kandzia, C.
Experimentelle Untersuchung der Strömungsstrukturen in einer Mischlüftung
1. Auflage 2014
ISBN 978-3-942789-19-6

E.ON ERC Band 21
Thomas, S.
A Medium-Voltage Multi-Level DC/DC Converter with High Voltage Transformation Ratio
1. Auflage 2014
ISBN 978-3-942789-20-2

E.ON ERC Band 22
Tang, J.
Probabilistic Analysis and Stability Assessment for Power Systems with Integration of Wind Generation and Synchrophasor Measurement
1. Auflage 2014
ISBN 978-3-942789-21-9

E.ON ERC Band 23
Sorda, G.
The Diffusion of Selected Renewable Energy Technologies: Modeling, Economic Impacts, and Policy Implications
1. Auflage 2014
ISBN 978-3-942789-22-6

E.ON ERC Band 24
Rosen, C.
Design considerations and functional analysis of local reserve energy markets for distributed generation
1. Auflage 2014
ISBN 978-3-942789-23-3

E.ON ERC Band 25
Ni, F.
Applications of Arbitrary Polynomial Chaos in Electrical Systems
1. Auflage 2015
ISBN 978-3-942789-24-0

E.ON ERC Band 26
Michelsen, C. C.
The *Energiewende* in the German Residential Sector: Empirical Essays on Homeowners' Choices of Space Heating Technologies
1. Auflage 2015
ISBN 978-3-942789-25-7

E.ON ERC Band 27
Rohlfs, W.
Decision-Making under Multi-Dimensional Price Uncertainty for Long-Lived Energy Investments
1. Auflage 2015
ISBN 978-3-942789-26-4

E.ON ERC Band 28
Wang, J.
Design of Novel Control algorithms of Power Converters for Distributed Generation
1. Auflage 2015
ISBN 978-3-942789-27-1

E.ON ERC Band 29
Helmedag, A.
System-Level Multi-Physics Power Hardware in the Loop Testing for Wind Energy Converters
1. Auflage 2015
ISBN 978-3-942789-28-8

E.ON ERC Band 30
Togawa, K.
Stochastics-based Methods Enabling Testing of Grid-related Algorithms through Simulation
1. Auflage 2015
ISBN 978-3-942789-29-5

E.ON ERC Band 31
Huchtemann, K.
Supply Temperature Control Concepts in Heat Pump Heating Systems
1. Auflage 2015
ISBN 978-3-942789-30-1

E.ON ERC Band 32
Molitor, C.
Residential City Districts as Flexibility Resource: Analysis, Simulation, and Decentralized Coordination Algorithms
1. Auflage 2015
ISBN 978-3-942789-31-8

E.ON ERC Band 33
Sunak, Y.
Spatial Perspectives on the Economics of Renewable Energy Technologies
1. Auflage 2015
ISBN 978-3-942789-32-5

E.ON ERC Band 34
Cupelli, M.
Advanced Control Methods for Robust Stability of MVDC Systems
1. Auflage 2015
ISBN 978-3-942789-33-2

E.ON ERC Band 35
Chen, K.
Active Thermal Management for Residential Air Source Heat Pump Systems
1. Auflage 2015
ISBN 978-3-942789-34-9

E.ON ERC Band 36
Pâques, G.
Development of SiC GTO Thyristors with Etched Junction Termination
1. Auflage 2016
ISBN 978-3-942789-35-6

E.ON ERC Band 37
Garnier, E.
Distributed Energy Resources and Virtual Power Plants: Economics of Investment and Operation
1. Auflage 2016
ISBN 978-3-942789-37-0

E.ON ERC Band 38
Calì, D.
Occupants' Behavior and its Impact upon the Energy Performance of Buildings
1. Auflage 2016
ISBN 978-3-942789-36-3

E.ON ERC Band 39
Isermann, T.
A Multi-Agent-based Component Control and Energy Management System for Electric Vehicles
1. Auflage 2016
ISBN 978-3-942789-38-7

E.ON ERC Band 40
Wu, X.
New Approaches to Dynamic Equivalent of Active Distribution Network for Transient Analysis
1. Auflage 2016
ISBN 978-3-942789-39-4

E.ON ERC Band 41
Garbuzova-Schiftler, M.
The Growing ESCO Market for Energy Efficiency in Russia: A Business and Risk Analysis
1. Auflage 2016
ISBN 978-3-942789-40-0

E.ON ERC Band 42
Huber, M.
Agentenbasierte Gebäudeautomation für raumlufttechnische Anlagen
1. Auflage 2016
ISBN 978-3-942789-41-7

E.ON ERC Band 43
Soltau, N.
High-Power Medium-Voltage DC-DC Converters: Design, Control and Demonstration
1. Auflage 2017
ISBN 978-3-942789-42-4

E.ON ERC Band 44
Stieneker, M.
Analysis of Medium-Voltage Direct-Current Collector Grids in Offshore Wind Parks
1. Auflage 2017
ISBN 978-3-942789-43-1

E.ON ERC Band 45
Bader, A.
Entwicklung eines Verfahrens zur Strompreisvorhersage im kurzfristigen Intraday-Handelszeitraum
1. Auflage 2017
ISBN 978-3-942789-44-8

E.ON ERC Band 46
Chen, T.
Upscaling Permeability for Fractured Porous Rocks and Modeling Anisotropic Flow and Heat Transport
1. Auflage 2017
ISBN 978-3-942789-45-5

E.ON ERC Band 47
Ferdowsi, M.
Data-Driven Approaches for Monitoring of Distribution Grids
1. Auflage 2017
ISBN 978-3-942789-46-2

E.ON ERC Band 48
Kopmann, N.
Betriebsverhalten freier Heizflächen unter zeitlich variablen Randbedingungen
1. Auflage 2017
ISBN 978-3-942789-47-9

E.ON ERC Band 49
Fütterer, J.
Tuning of PID Controllers within Building Energy Systems
1. Auflage 2017
ISBN 978-3-942789-48-6

E.ON ERC Band 50
Adler, F.
A Digital Hardware Platform for Distributed Real-Time Simulation of Power Electronic Systems
1. Auflage 2017
ISBN 978-3-942789-49-3

E.ON ERC Band 51
Harb, H.
Predictive Demand Side Management Strategies for Residential Building Energy Systems
1. Auflage 2017
ISBN 978-3-942789-50-9

E.ON ERC Band 52
Jahangiri, P.
Applications of Paraffin-Water Dispersions in Energy Distribution Systems
1. Auflage 2017
ISBN 978-3-942789-51-6

E.ON ERC Band 53
Adolph, M.
Identification of Characteristic User Behavior with a Simple User Interface in the Context of Space Heating
1. Auflage 2018
ISBN 978-3-942789-52-3

E.ON ERC Band 54
Galassi, V.
Experimental evidence of private energy consumer and prosumer preferences in the sustainable energy transition
1. Auflage 2017
ISBN 978-3-942789-53-0

E.ON ERC Band 55
Sangi, R.
Development of Exergy-based Control Strategies for Building Energy Systems
1. Auflage 2018
ISBN 978-3-942789-54-7

E.ON ERC Band 56
Stinner, S.
Quantifying and Aggregating the Flexibility of Building Energy Systems
1. Auflage 2018
ISBN 978-3-942789-55-4

E.ON ERC Band 57
Fuchs, M.
Graph Framework for Automated Urban Energy System Modeling
1. Auflage 2018
ISBN 978-3-942789-56-1

E.ON ERC Band 58
Osterhage, T.
Messdatengestützte Analyse und Interpretation sanierungsbedingter Effizienzsteigerungen im Wohnungsbau
1. Auflage 2018
ISBN 978-3-942789-57-8

E.ON ERC Band 59
Frieling, J.
Quantifying the Role of Energy in Aggregate Production Functions for Industrialized Countries
1. Auflage 2018
ISBN 978-3-942789-58-5

E.ON ERC Band 60
Lauster, M.
Parametrierbare Gebäudemodelle für dynamische Energiebedarfsrechnungen von Stadtquartieren
1. Auflage 2018
ISBN 978-3-942789-59-2

E.ON ERC Band 61
Zhu, L.
Modeling, Control and Hardware in the Loop in Medium Voltage DC Shipboard Power Systems
1. Auflage 2018
ISBN 978-3-942789-60-8

E.ON ERC Band 62
Feron, B.
An optimality assessment methodology for Home Energy Management System approaches based on uncertainty analysis
1. Auflage 2018
ISBN 978-3-942789-61-5

E.ON ERC Band 63
Diekerhof, M.
Distributed Optimization for the Exploitation of Multi-Energy Flexibility under Uncertainty in City Districts
1. Auflage 2018
ISBN 978-3-942789-62-2

E.ON ERC Band 64
Wolisz, H.
Transient Thermal Comfort Constraints for Model Predictive Heating Control
1. Auflage 2018
ISBN 978-3-942789-63-9

E.ON ERC Band 65
Pickartz, S.
Virtualization as an Enabler for Dynamic Resource Allocation in HPC
1. Auflage 2019
ISBN 978-3-942789-64-6

E.ON ERC Band 66
Khayyamim, S.
Centralized-decentralized Energy Management in Railway System
1. Auflage 2019
ISBN 978-3-942789-65-3

E.ON ERC Band 67
Schlösser, T.
Methodology for Holistic Evaluation of Building Energy Systems under Dynamic Boundary Conditions
1. Auflage 2019
ISBN 978-3-942789-66-0

E.ON ERC Band 68
Cui, S.
Modular Multilevel DC-DC Converters Interconnecting High-Voltage and Medium-Voltage DC Grids
1. Auflage 2019
ISBN 978-3-942789-67-7

E.ON ERC Band 69
Hu, J.
Modulation and Dynamic Control of Intelligent Dual-Active-Bridge Converter Based Substations for Flexible DC Grids
1. Auflage 2019
ISBN 978-3-942789-68-4

E.ON ERC Band 70
Schiefelbein, J.
Optimized Placement of Thermo-Electric Energy Systems in City Districts under Uncertainty
1. Auflage 2019
ISBN 978-3-942789-69-1

E.ON ERC Band 71
Ferdinand, R.
Grid Operation of HVDC-Connected Offshore Wind Farms: Power Quality and Switching Strategies
1. Auflage 2019
ISBN 978-3-942789-70-7

E.ON ERC Band 72
Musa, A.
Advanced Control Strategies for Stability Enhancement of Future Hybrid AC/DC Networks
1. Auflage 2019
ISBN 978-3-942789-71-4

E.ON ERC Band 73
Angioni, A.
Uncertainty modeling for analysis and design of monitoring systems for dynamic electrical distribution grids
1. Auflage 2019
ISBN 978-3-942789-72-1

E.ON ERC Band 74
Möhlenkamp, M.
Thermischer Komfort bei Quellluftströmungen
1. Auflage 2019
ISBN 978-3-942789-73-8

E.ON ERC Band 75
Voss, J.
Multi-Megawatt Three-Phase Dual-Active Bridge DC-DC Converter
1. Auflage 2019
ISBN 978-3-942789-74-5

E.ON ERC Band 76
Siddique, H.
The Three-Phase Dual-Active Bridge Converter Family: Modeling, Analysis, Optimization and Comparison of Two-Level and Three-Level Converter Variants
1. Auflage 2019
ISBN 978-3-942789-75-2

E.ON ERC Band 77
Heesen, F.
An Interdisciplinary Analysis of Heat Energy Consumption in Energy-Efficient Homes: Essays on Economic, Technical and Behavioral Aspects
1. Auflage 2019
ISBN 978-3-942789-76-9

E.ON ERC Band 78
Möller, R.
Untersuchung der Durchschlagspannung von Mineral-, Silikonölen und synthetischen Estern bei mittelfrequenten Spannungen
1. Auflage 2020
ISBN 978-3-942789-77-6

E.ON ERC Band 79
Höfer, T.
Transition Towards a Renewable Energy Infrastructure: Spatial Interdependencies and Stakeholder Preferences
1. Auflage 2020
ISBN 978-3-942789-78-3

E.ON ERC Band 80
Freitag, H.
Investigation of the Internal Flow Behavior in Active Chilled Beams
1. Auflage 2020
ISBN 978-3-942789-79-0

E.ON ERC Band 81
Razik, L.
High-Performance Computing Methods in Large-Scale Power System Simulation
1. Auflage 2020
ISBN 978-3-942789-80-6

E.ON ERC Band 82
Mirz, M.
A Dynamic Phasor Real-Time Simulation Based Digital Twin for Power Systems
1. Auflage 2020
ISBN 978-3-942789-81-3

E.ON ERC Band 83
Schmitz, H.
Energy Consumption Behavior of Private Households: Heterogeneity, Prosuming, and Rebound
1. Auflage 2020
ISBN 978-3-942789-82-0

E.ON ERC Band 84
Cupelli, L.
Data-driven Methods for Voltage Control in Distribution Networks: A Bottom-Up Approach
1. Auflage 2020
ISBN 978-3-942789-83-7

E.ON ERC Band 85
Happ, S.
A Scalable Simulation Method for Cyber-Physical Power Systems
1. Auflage 2020
ISBN 978-3-942789-84-4

E.ON ERC Band 86
Rewitz, K.
Modellierung des thermischen Komforts in Kabinen-innenräumen
1. Auflage 2021
ISBN 978-3-948234-00-3

E.ON ERC Band 87
Wesseling, M.
Probabilistische Bewertung von Entrauchungsanlagen
1. Auflage 2021
ISBN 978-3-948234-01-0

E.ON ERC Band 88
Stoyanova, I.
Cooperative Energy Management and Cross-Domain Optimization for Electro-Thermal Devices at City-District and City-Level
1. Auflage 2021
ISBN 978-3-948234-02-7

E.ON ERC Band 89
Tran, T.
Advanced hierarchical control structure for Virtual Oscillator-based distributed generation in multi-bus microgrids under different grid dynamics and disturbances
1. Auflage 2021
ISBN 978-3-948234-03-4

E.ON ERC Band 90
Yang, Z.
On the Stability of Three-Phase Grid-Tied Photovoltaic Inverter Systems
1. Auflage 2021
ISBN 978-3-948234-04-1

E.ON ERC Band 91
Wang, T.
Fault Detection and Isolation in DC Distribution Grids
1. Auflage 2021
ISBN 978-3-948234-05-8

E.ON ERC Band 92
Beushausen, S.
A GaN-Based Switched-Mode Gate-Drive Unit for Medium-Voltage IGBTs
1. Auflage 2021
ISBN 978-3-948234-06-5

E.ON ERC Band 93
Schumacher, M.
Design and Assessment of Grid-driven Distributed Cogeneration
1. Auflage 2021
ISBN 978-3-948234-07-2

E.ON ERC Band 94
Joebges, P.
Distributed Real-Time Simulation of Modular Bidirectional DC-DC Converters for Control-Hardware-in-the-Loop
1. Auflage 2021
ISBN 978-3-948234-08-9